DANMARKS OG GRØNLANDS GEOLOGISKE UNDERSØGELSE RAPPORT 2000/15

Characterisation and multistep upscaling of fractured chalk reservoirs

Final Report for JCR Phase V Project No. 3

Peter Frykman, Flemming If and John Jansson

GEOLOGICAL SURVEY OF DENMARK AND GREENLAND
MINISTRY OF ENVIRONMENT AND ENERGY

G E U S

DANMARKS OG GRØNLANDS GEOLOGISKE UNDERSØGELSE RAPPORT 2000/15

Characterisation and multistep upscaling of fractured chalk reservoirs

Final Report for JCR Phase V Project No. 3

Joint Chalk Research Phase V Project carried out in co-operation with COWI

Peter Frykman, Flemming If and John Jansson

Released 01.04.2005

GEOLOGICAL SURVEY OF DENMARK AND GREENLAND
MINISTRY OF ENVIRONMENT AND ENERGY

G E U S

CHARACTERISATION AND MULTISTEP UPSCALING OF FRACTURED CHALK RESERVOIRS.

JCR Phase V, Project no. 3

JCR Phase V Proposal (no: 96-chalk-07-01) Topic - Upscaling of reservoir heterogeneities.

Peter Frykman (GEUS)
Flemming If (COWI)
John Jansson (COWI)

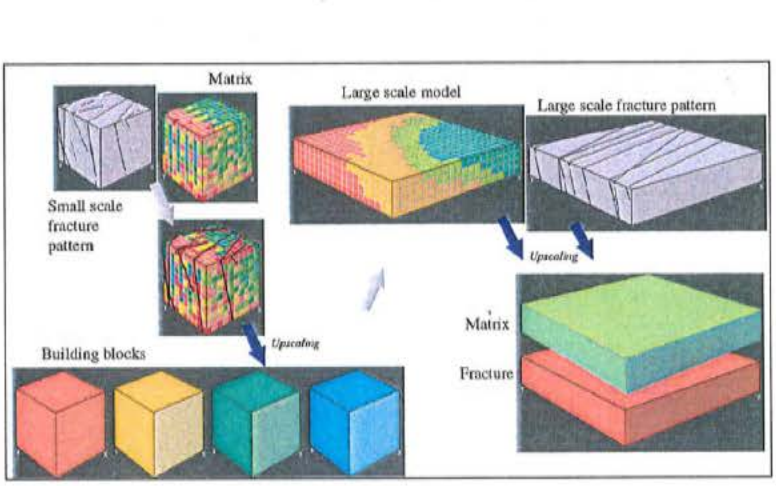

Final Report

GEUS

and

COWI

CONTENTS:

EXECUTIVE SUMMARY

The present project was carried out as part of the Joint Chalk Research Phase V during 1998-1999 as a joint effort by Geological Survey of Denmark and Greenland (GEUS) and COWI Consulting Engineers and Planners AS. Selected subjects were treated by a subcontractor at Danish Technical University. Co-operation with Project no. 2 in JCR-V has been active in the initial phase concerned with fracture network description.

The main objective for the project has been to develop a method for implementation of detailed description of matrix heterogeneities and fractures in a chalk reservoir into a reservoir simulation model. The characterisation and upscaling studies are concerned with single-phase flow properties only.

The project consists of the two main parts, characterisation of chalk matrix heterogeneities and development of a multi-step up-scaling method that incorporates fractures at different scales and calculates the effective absolute directional permeabilities at reservoir grid block scale.

The strategy has been to investigate selected chalk matrix heterogeneities and identify those observed to be important for the flow characteristics. Several heterogeneities important for the flow properties of the chalk are recognised at the scale of core plugs. The laboratory measurements of heterogeneities are aiming at supplying the best possible input for a 3D geostatistical modelling of fine-scale geological models. The heterogeneities at slightly larger scales are also investigated in this study. The vertical variations and cyclic development of porosity variations in the chalk is studied from several types of data, mostly at decimeter to meter scale. The combination of standard core plug data, fine-scale core-density scanning and well-log information is utilised to supply input parameters for generation of several geostatistical m^3 models.

The 3D geo-modelling performed on matrix properties is a necessary tool to generate exhaustive datasets used for the upscaling. The limited amount or even lack of certain input data is overcome by applying geostatistic methods to simulate the missing parts of the models. The investigations of heterogeneities, the modelling and the upscaling have been engaged also with quantifying the permeability anisotropy, usually specified as the k_V/k_H ratio (vertical permeability to horizontal permeability). The concept of nested anisotropy is introduced, and the concerted effect of different types of anisotropy existing at different scales is quantified.

Based on the findings in the matrix characterisation study and the reservoir simulation requirements a multi-step up-scaling method was developed. Fine scale 3D models of the matrix heterogeneities can be combined with fine scale fractures to form input to the first steps in the up-scaling procedure. These steps are designed to transfer the effects of matrix heterogeneities and fine scale fracture patterns from core plug scale to matrix models at m^3 scale. These m^3 models are then used as building blocks in the next up-scaling step to reservoir grid block size. This last up-scaling step may also take into account an overall fracture pattern and deliver grid block input data for a subsequent single- or dual porosity reservoir simulation.

The single-phase up-scaling procedure is described, and the algorithms are implemented in a developed software tool – ***FracSynt*** - which is described in the report. The tool allows combination of matrix and fracture network models in 3D, and performs upscaling of the flow characteristics. The effective permeabilities are described as 3D permeability tensors, and the software includes a wide range of routines to inspect the models.

The practical use of the developed up-scaling procedure is demonstrated by an example with real data from the Kraka Field. Matrix and fracture data from a vertical and a horizontal well form input to the example. The example illustrates that by using the developed up-scaling method it is possible to include chert beds and fractures in the calculation of the directional permeabilities for reservoir simulation models. The example shows the up-scaling to both single porosity and dual porosity reservoir simulation.

From the study of matrix heterogeneities it is concluded that many features have the effect of reducing the vertical permeability and therefore have consequences for the permeability anisotropy. The characterisation of the heterogeneities is heavily linked to the scale they occur at, and any permeability anisotropy at plug scale must be quantified and carried through to the larger scale models by explicit modelling and upscaling. Nested anisotropy is the combination of effects that is in effect at different scales, and is a common phenomenon that may increase anisotropy as the scale goes up.

A multistep upscaling method and procedure for fractured chalk has been developed. With the method it is possible to incorporate fine-scale geological observations and both fine-scale and field scale fracture networks in the upscaling.

Based on the findings and conclusions from the project we recommend to study further the flow effects of permeability variations. It is also recommended to extend the upscaling method to incorporate two-phase flow.

The final report has been forwarded to the participating companies in the Joint Chalk Research Program: Amerada Hess Norge AS, BP Amoco, DONG, Elf Petroleum, Enterprise Oil Norge Ltd., Phillips Petroleum Company Norway, Mærsk Olie og Gas, Norske Conoco AS, RWE-DEA, Veba Oil Nederland, TOTALFINA, and the two associated members Norwegian Petroleum Directorate and the Danish Energy Agency.

INTRODUCTION

The present project was carried out as part of the Joint Chalk Research Phase V during 1998-1999 as a joint effort by Geological Survey of Denmark and Greenland (GEUS) and COWI Consulting Engineers and Planners AS. Selected subjects on fine-scale heterogeneity characterisation were treated by Institute of Geology and Geotechnics at Danish Technical University. Co-operation with Project no. 2 in JCR-V has been active in the initial phase concerned with fracture network description. The reporting presented here is provided in sections concerned with the specific subjects treated. The developed software and case examples are included on a CD-ROM, that can be ordered from GEUS or COWI.

Objectives

The main objective for the project has been to develop a method for implementation of detailed description of matrix heterogeneities and fractures in a chalk reservoir into a reservoir simulation model. The characterisation and upscaling studies are concerned with single-phase flow properties only.

This objective was met by the following sequence of activities:

- Characterisation of flow properties of different types of heterogeneities in chalk.
- Investigation of the concept of type models for chalk, consisting of heterogeneity pattern and flow properties.
- Incorporation of fracture pattern and its properties in the matrix models.
- Upscaling of flow properties for the combined models at different block sizes.
- Comparison of new and old model methodology to investigate to what extent the more detailed reservoir description leads to better reservoir simulation models.

During the project work, the concept of type models at meter-scale had to be abandoned, because the variations in matrix heterogeneities were too large to allow the identification of an operational number of type models at this scale.

The project expanded the activities concerned with the development of a practical method for generation of 3D fracture patterns. The developed upscaling method was extended to include the option for upscaling both to single and to dual porosity simulation models.

Validation in a traditional sense of the developed single-phase flow upscaling method by comparing real well test data with the response from an upscaled model is not possible. This is due to the fact that detailed geological information is only known in the well, whereas the well production test depends on the geology in the much larger drained area. In addition the production tests are performed under multi-phase flow conditions and the upscaling method is for single-phase flow. The individual parts of the method have been validated by comparison with available analytical solutions. Therefore the validation has been substituted by a demonstration of the upscaling method on an example that illustrates the full work scheme involved and the feasibility of the methods.

Background and methodology

Although production of oil and gas is successful from chalk matrix reservoirs, it is generally accepted that the fracture network and its associated geometry and intensity of fractures, is a major factor in good productivity from chalk. However, the main part of the hydrocarbons are situated in the matrix rock and the properties of the matrix greatly influences the exchange of fluids between fractures and the matrix. Since this is important for the flow of hydrocarbons, the project has focused on a characterisation of the heterogeneities and the consequences for fluid flow of the heterogeneities existing in the matrix rock. The additional effects from the fracture network were taken into account in the upscaling, by considering specific fracture networks. These specific fracture networks are generated by fracture modelling.

Small-scale heterogeneities (mm- to cm-scale) in the matrix are investigated during core analysis of samples extracted from chalk core. Their combined effects are subsequently incorporated in the plug-measured properties. Heterogeneities larger than the sample size and combinations of different types of heterogeneities at scales larger than the cm-scale are not represented by any measured properties, except for the information derived from the wireline logs at dm-scale. As a consequence, these laboratory- and log-measured properties are not sufficient for the reservoir engineer who needs to input permeability functions for simulator blocks at a scale of 10-100 m. This is a classic problem in upscaling procedures. In this project, the problem is approached by starting at fine scale, using the plug-measured properties as input at their correct volume scale in a flow simulator. The simulation is designed to express the combined effects of the heterogeneities at a larger scale.

A requisite to properly modelling reservoir performance is a realistic numerical representation of the reservoir in a format usable by a reservoir flow simulator. "Realistic" means that a reservoir model must be consistent with all relevant data collected from the reservoir. This is difficult to achieve because reservoir models are built at one specific scale, whereas reservoir data, which come from many sources, are associated with different scales. Measurements made on one scale and on a specific support volume are, in general not directly applicable to another scale.
In order to transcend through the different scales according to the problems worked, upscaling is a main activity dealing with the consequences of small scale heterogeneities for the larger scale models and their behaviour. Since the change in scale from the volume of a core plug to a full field reservoir simulation cell is in the order of 10^9 (Fig. 1), this transition can normally not be carried out in a single step, due to the size of the models and the computational constraints from this.

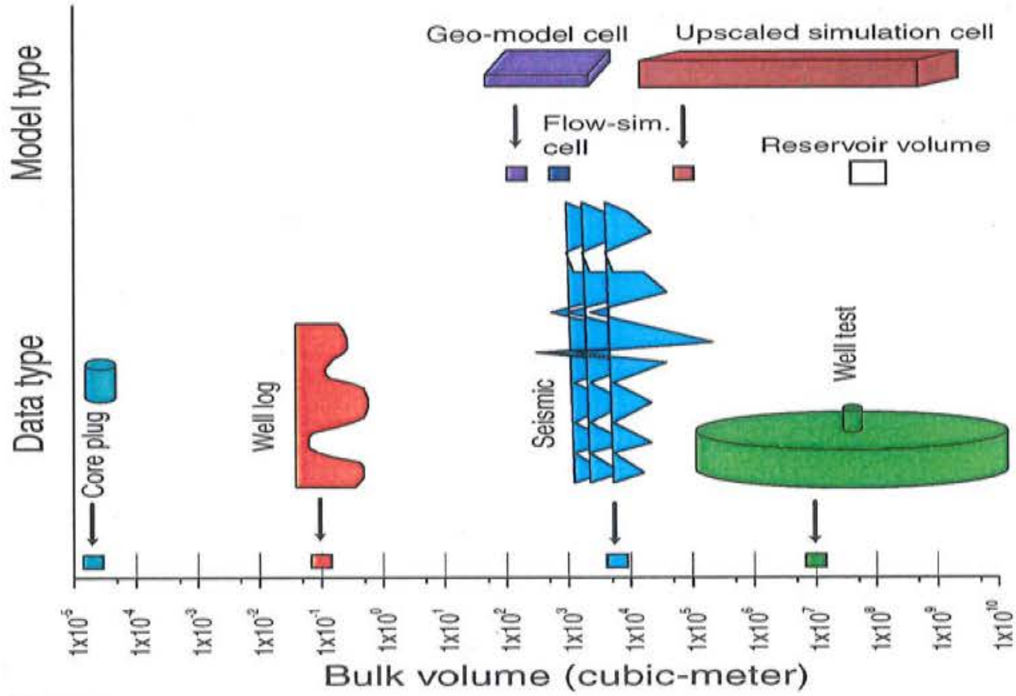

Figure 1
The figure shows that regarding volume, the scale distance from core plug to log scale is nearly as large as the scale difference from log to standard modelling cell scale. This therefore requires scaling relations also to be investigated between the core and log data, as well as the scaling from core+log to modelling cells or grid blocks.

The multi-step upscaling approach addresses this problem by dividing the upscaling into 2 or more steps as illustrated in Fig. 2.

- The first steps consist of upscaling the core plug data to a few m^3-sized models. These models are chosen so that they reflect the heterogeneity of the reservoir volume to be covered by the final reservoir simulation grid cell. In these first steps different fine scale fracture patterns can also be incorporated in the upscaling, resulting in permeability enhancement and permeability anisotropy.

- In the final upscaling step the effective properties of these fine scale models are combined to form a full field reservoir simulation cell in which the effect of the fine scale heterogeneities and fine scale fractures are represented. In the final step an overall fracture pattern can be incorporated in the upscaling for generation of input data to dual porosity reservoir simulation.

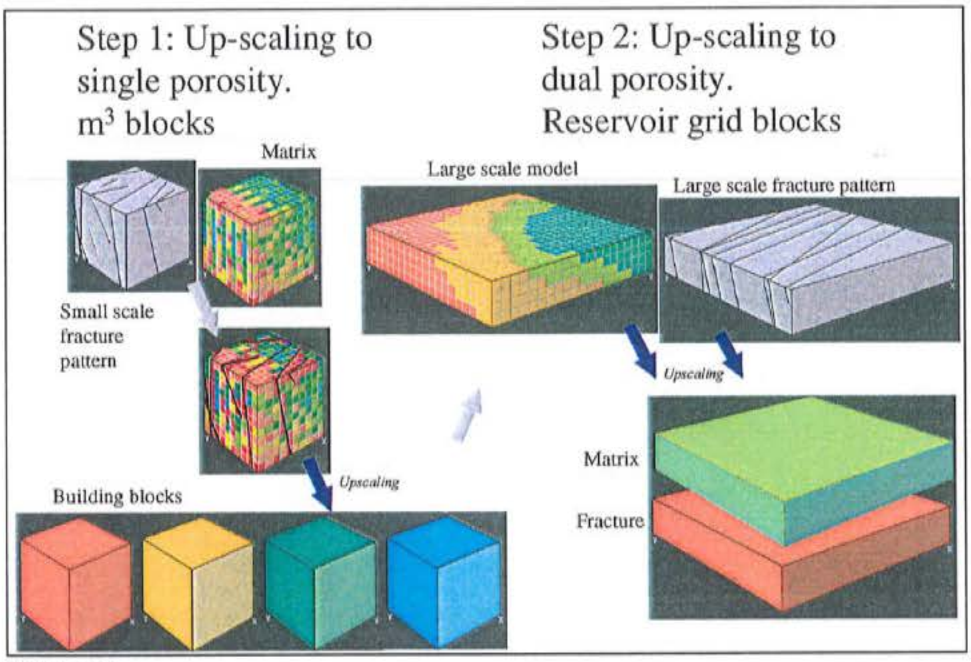

Figure 2
The multistep scheme adapted in the project.

Organisation of report

The report is organised in chapters for each topic. The sequence of chapters approximates the work flow process in an upscaling study.

First, an outline of the concepts for multi-step upscaling is given, supplemented by the principles behind nested anisotropy as an effect from heterogeneities at several scales. Then follows a presentation of numerical tools for quantification of heterogeneity and variability with an emphasis on the variogram analysis.

The heterogeneity catalogue presents a description of origin and representation for different types of matrix heterogeneities from small to larger scale, including measurements and analyses performed on their properties. The cm-scale of a core plug is chosen as the starting point for the upscaling exercise. Therefore it is important to quantify the effects from the heterogeneities existing on this scale on e.g. the permeability anisotropy expressed as the k_V/k_H ratio.

The next four chapters describe methods to quantify heterogeneity in matrix properties from mm- to m-scale. This step of multi-scale reservoir characterisation then leads to input to a modelling procedure for high-resolution models where in principle all the heterogeneities are incorporated at their correct scale. A geostatistical approach has been used to generate models for the fine-scale representation of matrix heterogeneities.

The high-resolution models are the input for an upscaling step, and it is described how the effective flow properties as well as the upscaled permeability anisotropy are derived. For the upscaling is used a developed software program - FracSynt – for which the documentation and methodology description is given.

In the demonstration chapter, the different steps in modelling of matrix properties and fracture networks is carried out on a real reservoir example, where well data forms the starting point for a derivation of effective properties for a full field simulation grid cell. It is shown how wireline log data can form the basis for a core-scale matrix model and a model for the natural fracture network. These models are merged and upscaling is performed with the software tool to derive the effective properties in a 2-step upscaling sequence.

Finally, the concluding remarks leads to recommendations for future work and extensions of the work with upscaling of chalk reservoir sequences.

CONCEPT OF UP-SCALING FROM CORE PLUG TO RESERVOIR SIMULATION GRID BLOCK SCALE

When building full-field reservoir simulation models with grid cells of 100 x 100 x 5 m^3 the problem arises of how to include and upscale the detailed geological information derived from core plug scale. As a result much geological information is often discarded and the potential effects of observed heterogeneities (e.g. stylolites, stylolite-associated fractures, healed hairline fractures, chert beds) are ignored.

A straight forward up-scaling is not possible because the size of a typical grid block used in full-field reservoir simulation corresponds to the volume of several billion core plugs.

In this project we have developed a multi-step up-scaling method which preserves the detailed matrix heterogeneities and fine fracture networks when computing the effective directional permeabilities. The developed method can also incorporate a large scale fracture pattern and is suitable for up-scaling to both single and dual porosity reservoir simulation models.

The multi-step up-scaling concept is summarised in Figure 3.

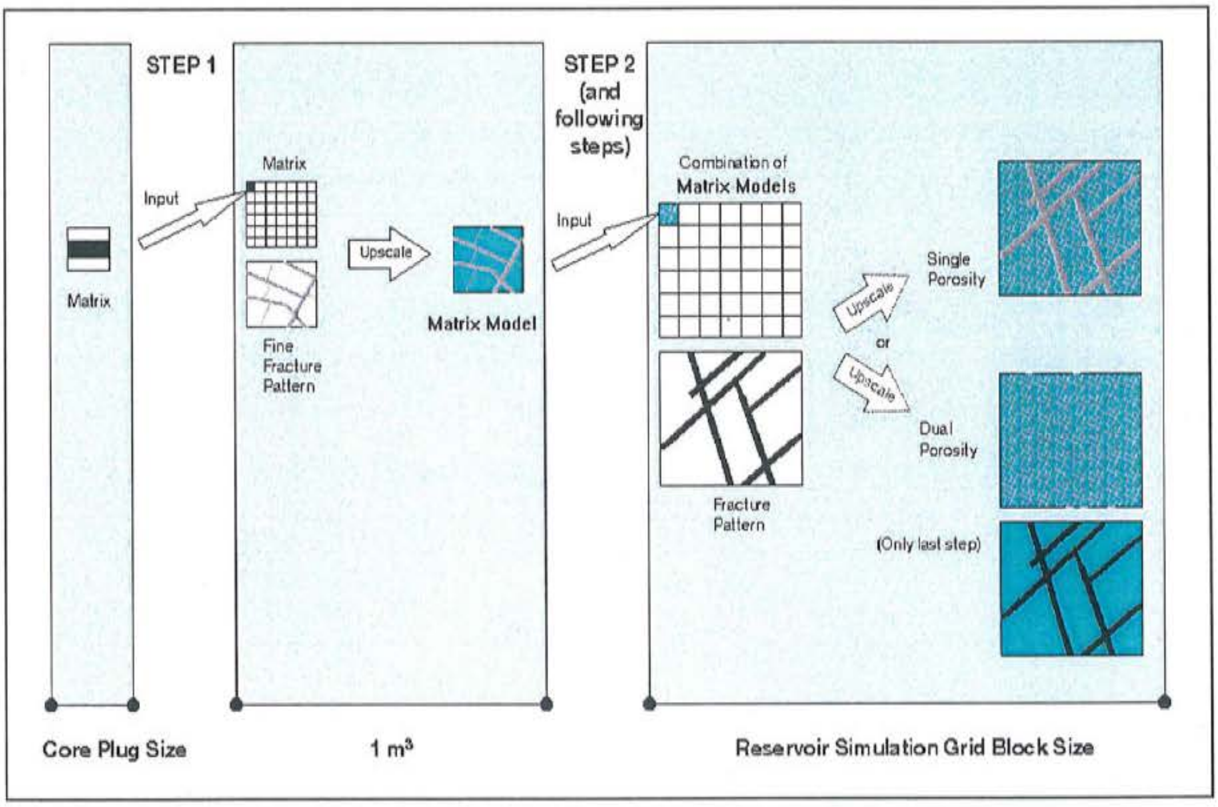

Figure 3
Upscaling from core plug to reservoir simulation grid block.

The multi-step up-scaling method is designed to take into account reservoir heterogeneities at the scale at which they are significant, and calculate the resulting porosity and directional permeabilities.
The small scale heterogeneity effects are transferred to the next step by using the calculated porosity and directional permeabilities in the next step in which reservoir characteristics at a

larger scale are incorporated. Finally, in the last up-scaling step to reservoir grid block size sections of an overall field wide fracture network can be incorporated and input for single porosity or dual porosity reservoir simulation models can be produced.

1 step: Generation of matrix models

The first step in the procedure consists of an up-scaling from a detailed description of porosity and permeability at core plug size to a m^3 sized matrix block. The step may involve a geostatistical treatment of the detailed geological information as a mean to produce a realistic 3D distribution of the data. In this step a small-scale fracture pattern can be merged with the matrix description into one media and up-scaled to a m^3 sized matrix model, including the effects of the fractures.

The first up-scaling step involves generation of several such matrix models reflecting variations in the sequence, in order to produce input data (porosity and directional permeabilities) to the next up-scaling step.

2 step: Generation of rock parameters at reservoir simulation grid block level

In the second step the m^3 sized matrix models are combined in a grid covering a volume corresponding to a reservoir simulation grid block cell. A section of a field wide fracture pattern or a local fracture pattern on 100m scale can be combined with the matrix grid and up-scaled to a reservoir simulation grid block. The last step consists of separate up-scaling of the matrix and of the fracture network for generation of input data to dual porosity or dual permeability reservoir simulation. Alternatively, the fracture network and the matrix data can be merged into a single matrix model and up-scaled as one media to form input to single porosity reservoir simulation. The inclusion of the fractures will have the effect of increasing the permeability in the dominant fracture direction. The latter information can also be used to test grid orientation effects.

Up-scaling software tool

A software tool has been developed, *FracSynt*, which merges a fine grid matrix description with an overall 3D-fracture network, and computes the up-scaled directional matrix and fracture permeabilities. The input to *FracSynt* is fine grid models of matrix porosity and directional permeability data and a specific 3D-fracture network geometry and associated fracture aperture data. The matrix and the fracture data can be up-scaled separately as two media or the matrix and the fracture data can be merged into a matrix model and up-scaled as one media.

SCALE DEPENDENT PERMEABILITY ANISOTROPY

Permeability anisotropy is widely used as one of the "matching parameters" in full-field reservoir simulations for chalk reservoirs. Company experience in some cases advocates an anisotropy factor as low as 0.1-0.2 for the $\mathbf{k_V/k_H}$ ratio (vertical permeability : horizontal permeability) in order to obtain a match to the existing production data.
The geological background for such significant anisotropies has been largely unknown, and existing measurements on core material have not been able to support this level of anisotropy. An alternative explanation is the effect of relative permeabilities in multi-phase flow situations and the combination with relatively large simulation grid block sizes.

The present study is therefore reviewing some of the candidates for single-phase flow permeability anisotropy in the geological material across a wide range of scales in chalk

reservoirs. The results indicate that it is not a single feature that is responsible for the full anisotropy, but that it is rather the cumulative effect of several features at a range of scales: i.e. from mm-scale (primary or diagenetic phenomena) to m-scale (bedding and cyclic porosity variations), that in concert are creating anisotropy at reservoir simulation block scale. This combination is termed "nested anisotropy", signifying that the different effects from the very different features are embedded in the model at different scales.
The conclusions have been reached by use of fine-scale geological modelling with elaborate core analysis data as input, and subsequent upscaling by use of single-phase flow simulation to derive the effective properties of larger volumes.
Examples of nested anisotropy analysis in the case study show values for k_V/k_H down to 0.25 (still being inadequate to satisfy the extreme "needs" for anisotropy), but further anisotropy could be due to extra effects during multiphase flow.

Synthesis

The anisotropy analyses performed in this study at different scales, and including very different features, are summarised in Figure 4. The illustration in most cases shows both a minimum and a maximum value (in few cases the mean also) for the individual features investigated by direct core analysis measurements, but also for the examples where nested anisotropy has been quantified by the flow simulation studies.

The mean anisotropy and spread for the different features are seen to vary, and are depending on the specific examples investigated (Fig. 4). It is seen that the spread and mean is changing with the change in scale. The increasing anisotropy (decreasing k_V/k_H) seen until the 1 m scale is due to the cumulative effect of nested anisotropy where small- and large-scale features are combined into the 1 m^3 blocks investigated. From 1 m and up to the 20 m scale, nested anisotropy is not seen to be in effect, since the same sequence is used for the upscaling. Therefore the anisotropy decreases and the spread is decreased.

Conclusions

The combined effect of small- and large-scale heterogeneities in a nested pattern is responsible for the ultimate permeability anisotropy seen in chalk sequences. It is therefore important to evaluate at which scale the important features exist, and accommodate them in the modelling at that scale in order for them to be represented during the upscaling.
As mentioned, effects during multi-phase flow might cause additional significant anisotropy and should be evaluated accordingly, as suggested in recommendation for future work.

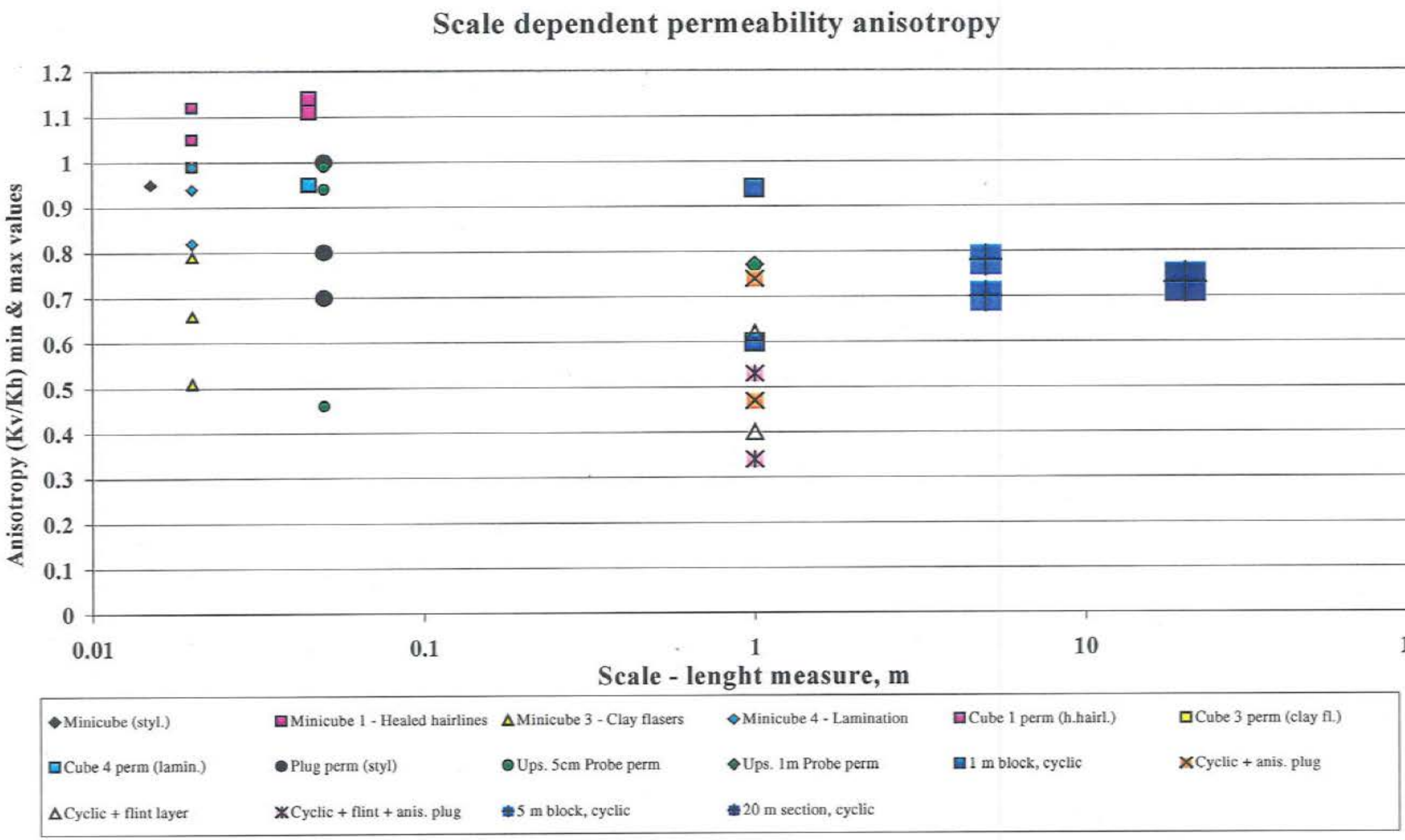

Figure 4.
The figure shows the permeability anisotropy as a function of the scale they are measured at. The increasing anisotropy (decreasing k_V/k_H) seen until the 1 m scale is due to the cumulative effect of nested anisotropy where small- and large-scale features get combined into the 1 m^3 blocks investigated. From 1 m and up to the 20 m scale, nested anisotropy is not in effect, since the same sequence is used for the upscaling. Therefore the anisotropy decreases and the spread is likewise decreased.

QUANTIFICATION OF HETEROGENEITY

In reservoir characterisation heterogeneity specifically applies to variability that affects flow. Heterogeneity and variability is usually used interchangeably.
Heterogeneity is the property of the medium that causes the flood-front spreading and distribution. In single-phase flow it can cause crossflow and/or permeability anisotropy.
When summarising variability or heterogeneity, a considerable amount of information is lost. This is an advantage in upscaling that aims at producing a system with less details and numerical calculations become simpler. The critical step is to preserve the characteristics that have the most effect on flow and retain that information in the summarised system
Heterogeneity measures can be classified into two groups: Static and dynamic.
Static measures are based on measured samples from the formation, and require additional use of a flow model to interpret the effects of variability on flow.
Dynamic measures use a flow experiment and are therefore a direct measure of how the heterogeneity affects the flow.

Static measures of heterogeneity

Several tools are available for the quantification of the variability for a given collection of samples. The simplest is probably the mere posting of the values as a curve (1D), or a map with point values posted (2D). A more advanced step is to calculate the histograms for different data sets to obtain a comparison and show the mean, standard-deviation, median, and coefficient of variation for the sample sets. This is illustrated for two data-sets in Fig 5 and Fig. 6.

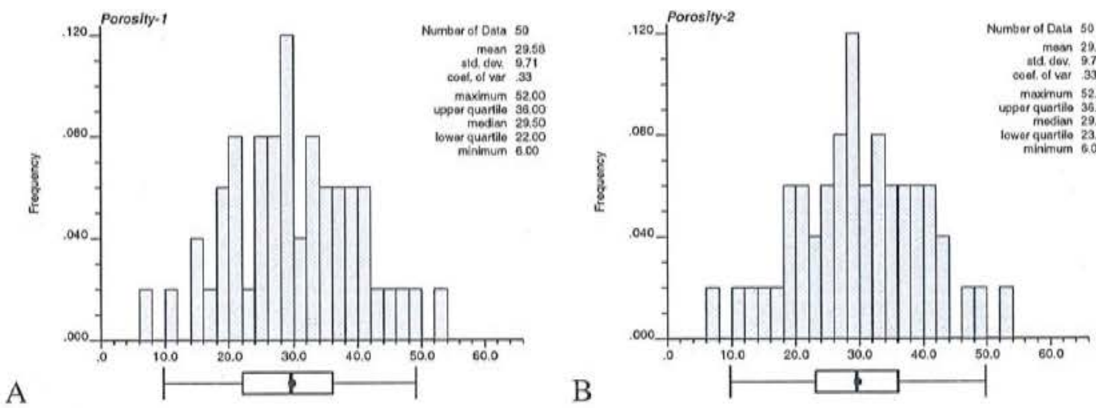

Figure 5
Histograms for two data sets of porosity values.

For the data in Fig. 5 the results are also given in table 1, which shows that very similar values are derived.

Table 1	Porosity-1	Porosity-2
Mean	29.6	29.6
St.dev.	9.71	9.72
Median	29.5	29.5
CV	0.33	0.33

However, when the actual data is illustrated it is clear that the distribution pattern is very different for the two data sets (Fig. 6), and that the summary statistics from the histogram is not sufficient to characterise the population of data.

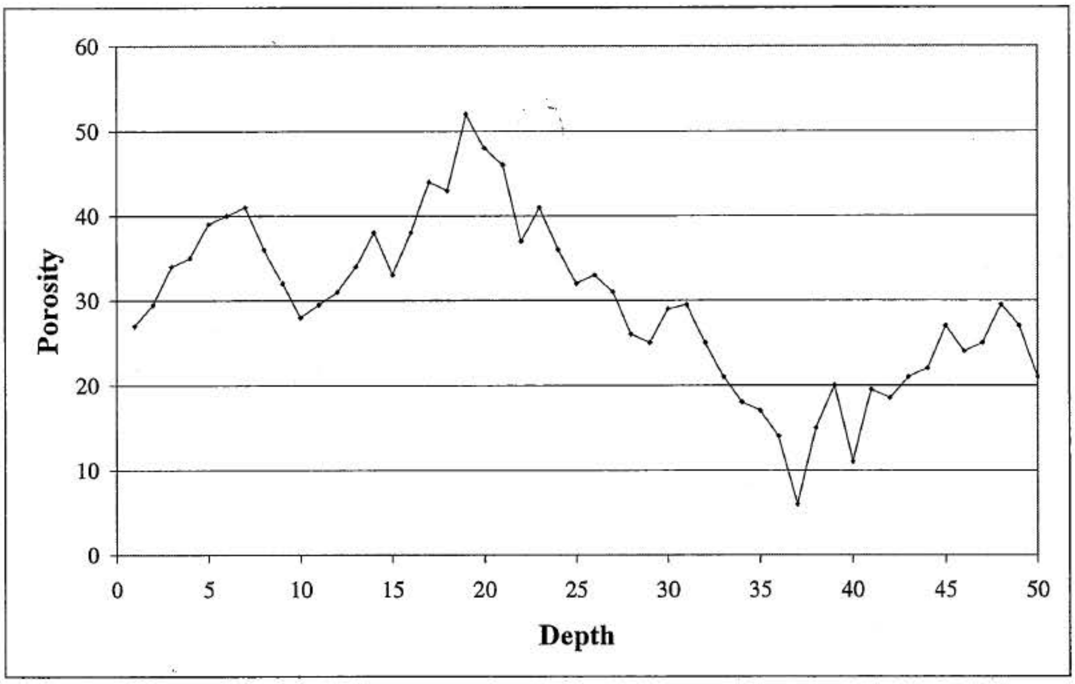

A: Porosity-1

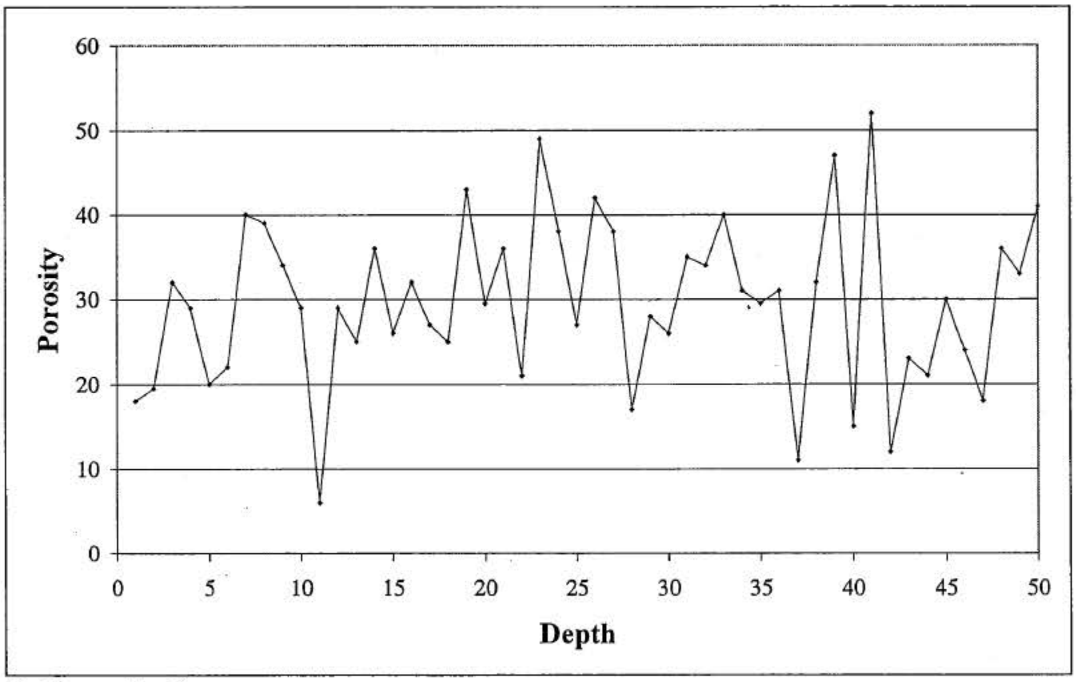

B: Porosity-2

Figure 6
Comparison of data set 1 and 2 showing a very different pattern in the values.

Variogram characterisation

If we want to quantify the pattern we have to use measures of the spatial correlation. This is often given by the variogram, a commonly used tool in geostatistics to determine the correlation structure in data. Technically the correct term is a semivariogram, but in normal use it is just called the variogram. The variogram expresses the average difference for all pairs of values with a given separation distance which is varied in the analysis. As the distance between locations increase, the relationship strength usually diminishes and the variogram value (γ) increases. The variogram value γ is calculated as:

$$\gamma(s) = \frac{1}{2N(s)} \sum_{i=1}^{N(s)} \left[Y(Xi) - Y(Xi+s)\right]^2$$

where Y is the variable value at position X, and X goes through all points from 1 to N (N=number of points). S is the separation distance between the compared points, and S is varied from zero to a maximum value given by the extent of the specific data set.

When γ is calculated as a function of distance for data that are spatially correlated, the values commonly form a curve like the one shown in Fig. 7. The value of γ rises from near zero and levels off at a plateau known as the sill. When a horizontal sill exists, the value of γ at the sill is equal to the variance of the data set. The curve in Fig. 7 signifies that the variability of the data pairs increases with distance until the separation distance is too large for values to be correlated. The distance at which γ ceases to increase significantly is known as the range. The initial value of γ may not be zero, but may be any value up to the value of γ. This is known as the nugget effect, and the higher the initial value is, the poorer or unresolved is the spatial correlation at the small scale. The nugget can be due to either noise (no correlation), or measurement errors, or can be correlation at very small scale not being resolved with the too coarse variogram calculation performed.

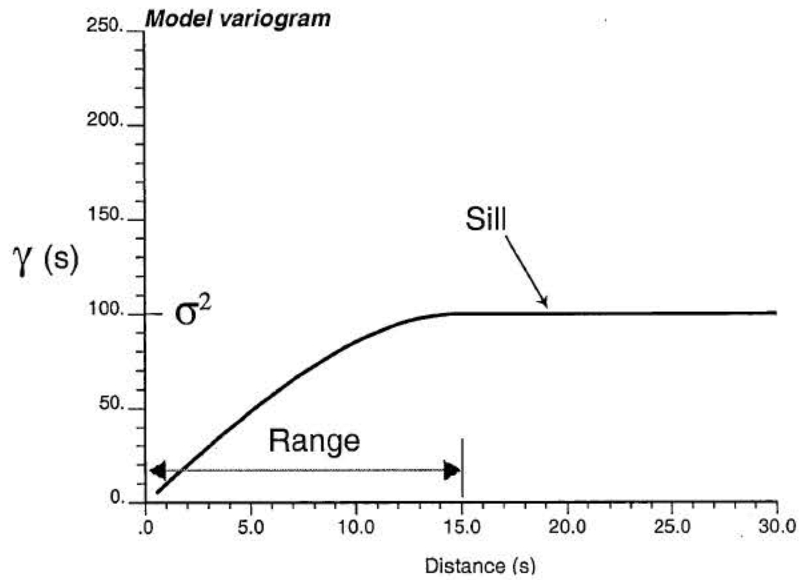

Figure 7
Schematic example showing how the variogram relations are.

The calculated experimental variogram for the two data sets are clearly very different and quantifies the spatial correlation in the data (Fig. 8)

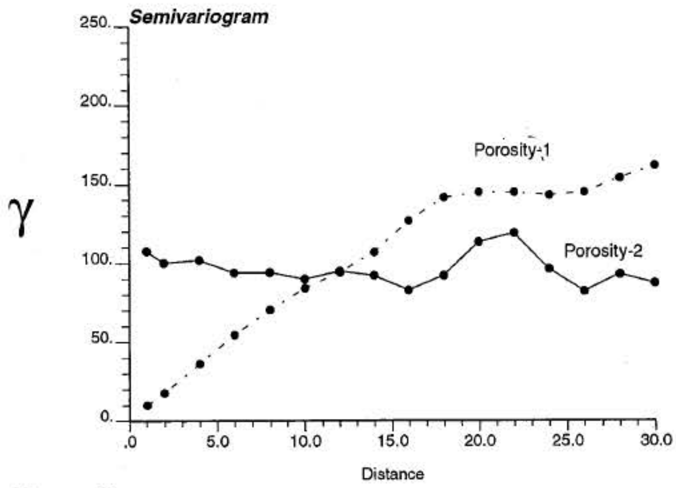

Figure 8
Experimental variogram for the two data sets. The x-axis is the separation distance between the samples compared, normally called lag distance. The y-axis γ is the semivariance calculated as the sum of squared differences for each value of the separation distance chosen. The data from Porosity-1 does not reach a plateau γ value due to a general trend in the data. The variogram for Porosity-2 reaches the plateau (the sill) immediately, and therefore shows no spatial correlation but only pure nugget effect.

The variogram can also be used to estimate if the sample density in a sequence is sufficient for characterisation of the spatial variability. The sample spacing should on average be shorter than half the range of the variogram. This is considered the minimum in order to model the variogram and estimate pattern of the variability.
For different sample sets having a different support volume, i.e. with properties measured on different sizes of rock volume, scaling laws exist for connecting the different scales (Frykman & Deutsch 1999). These laws are applied under certain basic assumptions in order to scale both the histogram and variogram between different scale levels, and estimate the target histogram and variogram for simulating at larger or smaller scales than the original data.

The coefficient of variation

If an estimate of the average permeability for a given sequence is sufficient for the further modelling, a measure involving the *coefficient of variation* - C_V is applicable, and is often used in the description of the amount of variation in a population (Jensen *et al.* 1997).
The coefficient of variation is being increasingly applied in geological and engineering studies as an assessment of permeability heterogeneity. For geologically similar elements in outcrop and subsurface it has been shown that the C_V's remain similar despite changes in the average permeability (Kittridge *et al.* 1990; Goggin *et al.* 1992). Also other studies (e.g (Corbett & Jensen 1992)) suggest that C_V might be linked to scale.

C_V is the square-root of the variance of the variable k, divided by the mean of the k population.

$$C_V = \frac{\sqrt{Var(k)}}{E(k)}$$

This dimensionless measure of sample variability or dispersion, therefore expresses the standard deviation as a fraction of the mean value.

Sampling density

C_V has also been used to guide sampling density. The so-called "*N-zero method*" has been discussed and is based on two results from statistical theory (Hurst & Rosvoll 1991):

1. The Central Limit Theorem states that, if Is independent samples are drawn from a population (not necessarily normal) with mean μ and standard deviation σ, then the distribution of their arithmetic average will be approximately normal.
2. The sample average will have mean μ and standard error $= \dfrac{\sigma}{\sqrt{Is}}$

From these two points, the probability that the sample average $\bar{k}s$ of Is observations lies within a certain range of the population mean (μ) can be determined for a given confidence interval.

For a 95% confidence level, and assuming a normal distribution, we can derive an expression for the appropriate number of samples - the appropriate number of specimens (I_0) for giving the sample mean within ±20% of the parent mean for 95% of all possible samples, which we consider to be an acceptable limitation:

$I_0 = (10 * \hat{C}_V)^2$

This rule of thumb is a simple way of determining sample sufficiency. Since $\hat{C}_V$ is a random variable, I_0 is also random in the above expression. I_0 will change because of sampling variability.

The above approach is called the I_0-sampling approach. Having determined the appropriate number of samples, the domain length, i.e. the length of the sequence investigated (d) will determine the sample spacing *(d_0) as $d_0=d/I_0$.*

Example: Variability and sampling

The example data is taken from the analysis of probe permeameter data that are reported elsewhere in the report. In the 8 m interval from the well N-22 of bedded chalk from core no. 6 in this analysis, the performance of core plugs is compared with the probe permeameter for the estimate of the mean permeability of the interval. Based on the core plugs $\hat{C}_V = 0.20$, giving $I_0 = 4$ and therefore a sample spacing of $d_0 = 2$ meter, which is well above the customary 1 ft. sampling interval. Therefore the mean value is properly estimated from this sampling scheme in this sequence. The probe data give $I_0 = 16$ and $d_0 = 0.5$ meter.

For such variability, only about 16 probe measurements are needed within the 8 meter section for estimates of a valid average permeability within ±20%.

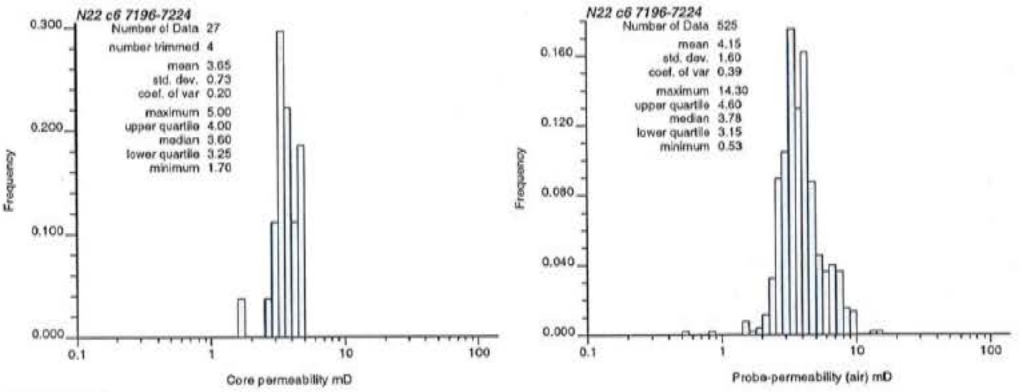

Figure 9

Histogram of core plug and probe permeability values from the core no. 6 interval.

The experimental variogram for the probe permeability data is calculated in order to see any correlation structure in the material (Fig. 10).

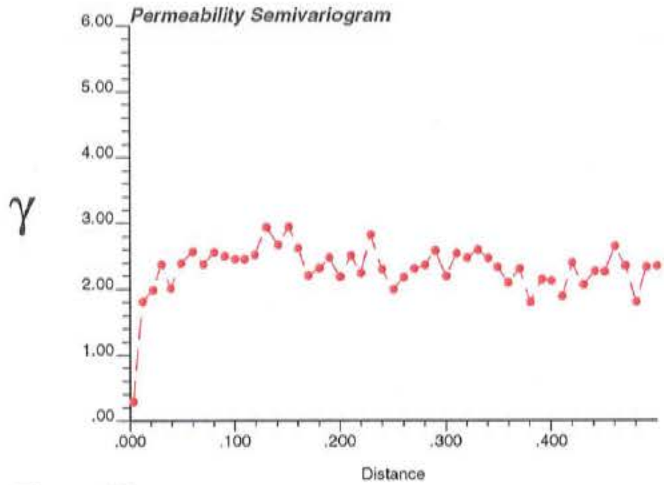

Figure 10

Experimental variogram for the probe permeability values from the core no. 6 interval.. The variogram calculated shows a range around 0.06-0.08 m. This shows that in the investigated section, the amount of heterogeneity captured within a plug volume (ca. 0.02-0.03 m) represents nearly 80% of the total variability in the probe permeameter data.

Conclusion

The very short correlation range (6-8 cm) shown by the probe permeameter data in the example, indicates that a standard core plug of 2 inch length captures most of the small-scale permeability heterogeneity. In order to investigate if the larger scale pattern is sufficiently mapped, the variogram for the plug samples in the sequence must be investigated more closely.

References

Corbett, P.W.M. & Jensen, J.L. 1992: Estimating the mean permeability; how many measurements do you need? First Break **10**(3), 89-94.

Frykman, P. & Deutsch, C.V. 1999: Geostatistical scaling laws applied to core and log data. 1999 SPE Annual Technical Conference and Exhibition, Houston, Texas, 3-6 October 1999, 12 pp. Society of Petroleum Engineers (SPE 56822).

Goggin, D.J., Chandler, M.A., Kocurek, G. & Lake, L.W. 1992: Permeability transects of eolian sands and their use in generating random permeability fields. SPE Formation Evaluation 7(1), 7-16.

Hurst, A. & Rosvoll, K.J. 1991: Permeability variations in sandstones and their relationship to sedimentary structures. In: Lake, L.W., Carroll, H.B.Jr. and Wesson, T.C. (ed.): Reservoir Characterization, 166-196. Orlando: Academic Press Inc.

Jensen, J.L., Lake, L.W., Corbett, P.W.M. & Goggin, D.J. 1997: Statistics for petroleum engineers and geoscientists, 390 pp.: Prentice Hall.

Kittridge, M.G., Lake, L.W., Lucia, F.J. & Fogg, G.E. 1990: Outcrop/Subsurface Comparisons of Heterogeneity in the San Andres Formation. SPE Formation Evaluation **5**, 233-240.

Heterogeneity catalogue

Peter Frykman, Niels Stentoft, Finn Jakobsen, Kim Zinck-Jørgensen (GEUS)
& Ida Fabricius (DTU)

CHARACTERISATION AND MULTISTEP UPSCALING OF FRACTURED CHALK RESERVOIRS.

JCR PHASE V, PROJECT NO. 3

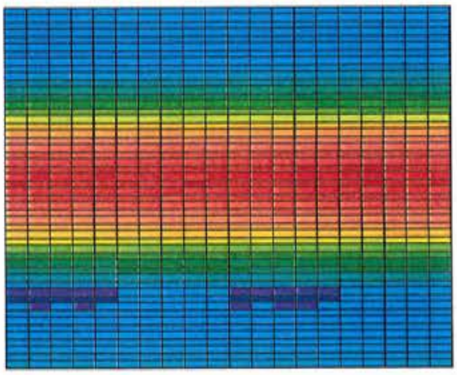

INTRODUCTION

Many heterogeneities are recognised at the scale of a core plug from core material. Therefore the common starting point for many of our investigations is to map the occurrence and effect of heterogeneities at this scale of a few cm. The presented quantifications of the flow properties of heterogeneities are all aiming at supplying the best possible input for the full 3D modelling of fine-scale geological models that are to be used as the vehicle for upscaling.

The arrangement of the plug-scale heterogeneity at slightly larger scale is also important, and therefore a description of the occurrence and genesis of the heterogeneities are given, in order to be related to the other types of heterogeneity existing in a given sequence. The vertical variations and cyclic development of porosity variations in the chalk is studied from several types of data, mostly at decimeter to meter scale. The combination of standard core plug data, fine-scale core-density scanning, and well-log information is utilised to supply input parameters for the 3D models generated at cm resolution. This input is primarily used for generating porosity models, but these have an immediate link to the permeability models that are needed to perform the flow property upscaling.

"Nested heterogeneity"

Heterogeneity is usually linked with a specific scale at which they are recognised, and at which they have an effect on the flow properties of the rock volume. Since several scales can have significant heterogeneity and act simultaneously, their combined effect must be considered. Their effects are not simple additive or products, but rather complex interactions. Therefore their cumulative effect most be investigated by constructing models incorporating heterogeneities at their specific scale, and their effective properties must be derived with dynamic upscaling methods.

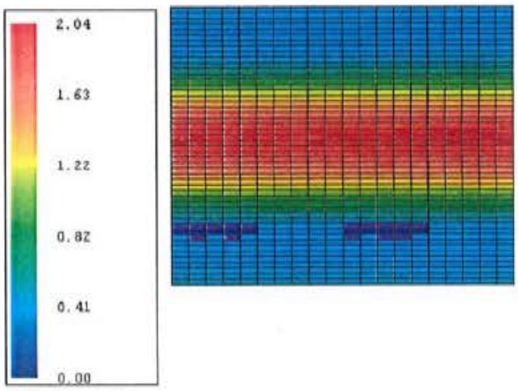

Figure 11

Illustration of the "nested heterogeneity" concept with a permeability model. The model is constructed of small cells, each being the size of a core plug. These cells can have an anisotropy assigned determined by their type of heterogeneity (e.g. lamination, clay-seams, or healed hairline fractures). The meter-scale model incorporates both cyclic layering and two flint nodules that act as flow modifiers at m-scale. At even larger scale, a depth trend or other larger-scale fluctuations in permeability could have an effect.

Overview:

The heterogeneity catalogue is summarising previous work and new studies performed on different types of heterogeneities in the chalk. The summary is focused on the flow properties, and especially on their effects on the permeability anisotropy.

Heterogeneities from small to large scale

1 cm	sedimentary heterogeneities - lamination, bioturbation, intraclasts clay drape, solution seams, flasers healed fractures stylolites stylolite fractures
10 cm	chert nodules and silicified layers
1 m	layering, cyclicity marly layers hardgrounds fractures and fracture zones
10-100 m	vertical and lateral trends

Catalogue Contents:

- Lamination
- Healed hairline fractures
- Solution seams and flasers
- Stylolites
- Stylolite-associated fractures
- Chert/Flint nodules

LAMINATION

Description of feature
A faint mm scale lamination is commonly seen in the Maastrichtian and Danian chalk of the Dan Field (e.g. Fig. 12 showing MFB-7 material). The lamination is rather indistinct in the chalk from the gas- and water-zone, and in places invisible unless the rock is moistened with oil or water. In the oil-zone their visibility is usually enhanced by a variation in oilstaining (Fig. 12), which brings out the laminae, indicating that some microtextural variations influence the capillary forces that act on the fluids in the rock matrix. When this chalk is cleaned for laboratory analyses, the lamination usually disappears.

The examples of lamination in chalk from the Dan Field represents a primary sedimentary structure, that rather easily, by use of a hand lens on a moistened rock surface, can be distinguished from the pseudo lamination arising from the presence of diagenetic structures, such as closely packed parallel lines of microstylolites or solution seams. The primary origin of the lamination is confirmed by studies of the temporal relations of formation between lamination and burrowing (trace fossils), and between lamination and hairline fractures: both burrowing and hairline fractures postdate the lamination. The laminated chalk intervals are usually supposed to be allochthonous of nature, being deposited from distal turbiditic mud clouds. This assumption is based on the need for high sedimentation rate, in order for the lamination to escape destruction by the burrowing organisms roaming vigorously in the uppermost 5-10 cm of the sediment on the chalk sea-bottom.

Origins
Also in other areas the centimetre to millimetre laminations have been widely recorded (Kennedy 1987). The fact that they show clear alternations with bioturbated chalk is supporting evidence of their primary origin, and some fine laminations are cut by burrows. However, there are also many occurrences of micro-laminations that cut across existing burrows of *Planolites* and *Zoophycos*, and these laminations are considered micro-stylolites (Ekdale & Bromley 1988). In clean white chalk it might be impossible to distinguish primary from diagenetic laminations (Hancock 1993).

When studied in thin-section by means of a polarizing microscope it appears that the lamination is caused by variations in the concentrations of skeletal grains, mostly being planktic foraminifera tests and/or calcispheres, in places *Inoceramus* fragments. Alternating thin layers of mudstone and wackestone, or in places mudstone and packstone, are thus resulting in the lamination. No variation is seen in the composition of the micritic matrix across the laminae.
By BSE imaging of polished chalk samples, in which a lamination is demonstrated under a prior microscope investigation, no textural variations outlining the lamination can usually be recognised (Dons *et al.* 1995). Only a relatively few samples have shown a faint lamination caused by variations in the density of allochems. Any possible minute differences in the texture of the micritic matrix related to the laminae is difficult to detect even by use of BSE because of the very high magnification needed for the study of the matrix.

Analysis
X-ray CT-scannings and NMR-scannings of chalk material (small cubes and plugs) in which a mm scale lamination is recognised by eye or under a microscope, usually reveal the presence of horizontal low-porosity layers corresponding to the primary lamination (Dons & Olsen 1996).

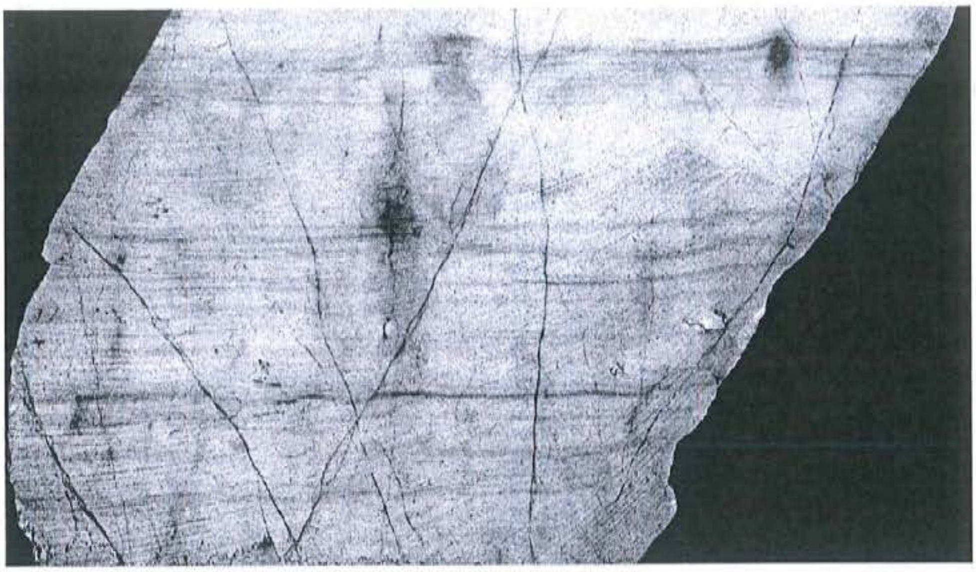

Figure 12
Core from MFB-7 (7570') showing lamination enhanced by the oil staining. The dark lines across the laminae are healed hairline fractures. Core diameter seen here is 11 cm.

Even if laminae-related differences of the texture of the micritic matrix can not be demonstrated, it is expected that some permeability heterogeneity exists in laminated chalk samples. This assumes that the variation in the concentrations of allochems (which causes the lamination) is significant, e.g. when laminae of mudstone alternate with laminae of packstone. In this case the permeability in the directions parallel to the lamination should be a little higher than the permeability in the direction normal to the laminae (in the vertical flow-direction). This prediction is supported by the cube analysis carried out, although the k_V/k_H ratio is close to 1.

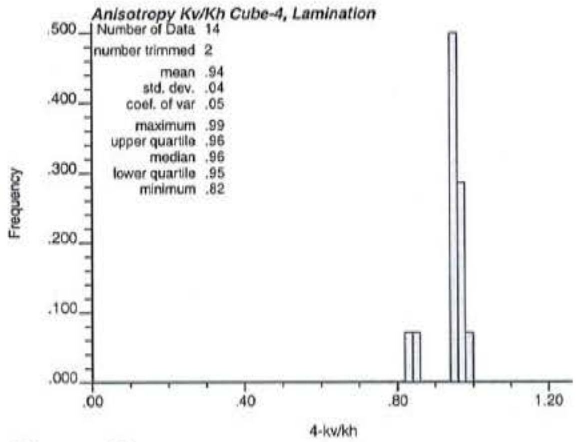

Figure 13
Histogram of anisotropy (k_V/k_H) values from minicubes for cube 4 with lamination.

HEALED HAIRLINE FRACTURES

Description of feature

Three kinds of fractures are usually seen in the chalk of the North Sea: hairline fractures, tectonic fractures, and stylolite-associated fractures. Both the tectonic fractures and the stylolite-associated fractures may be open to fluid flow, acting as avenues for hydrocarbon migration, but also contributing essentially to an increase of the permeability in the reservoir chalk. The hairline fractures, are at best neutral, or might give rise to a slight reduction of both porosity and permeability.

It must be admitted that the term "hairline fractures" is not quite appropriate for these peculiar structures: First of all, they do not always appear as hairline traces on the core surface, as the width of the feature sometimes amounts to a few mm (measured normal to the fracture surface). Secondly, both later diagenetic tectonic fractures and stylolite-associated fractures may also quite often appear as hairline traces on the rock surface. The hairline fractures described above have by some authors been referred to as "healed fractures" and "healed hairlines". These interpretative terms should be avoided, at least without any explanation of the term "healed". The latter term suggests a fracture that has been plugged with precipitates, or a former fissure now being closed, or healed up, due to compressional stress or diagenesis. Even if uncomfortable with these terms, they will be used liberally in the text.

Hairline fractures are observed in chalk from both Danian and Maastrichtian ages, but only a very scattered occurrence is seen in the tight zones of Danian age (e.g. (Dons *et al.* 1995). The density seems to some extent to be related to sedimentary facies, as an increase in hairline fracturation is usually seen in units of more rapidly deposited, allochthonous chalk showing very little bioturbation (cf. Dons *et al.* 1995), and Fig. 14.

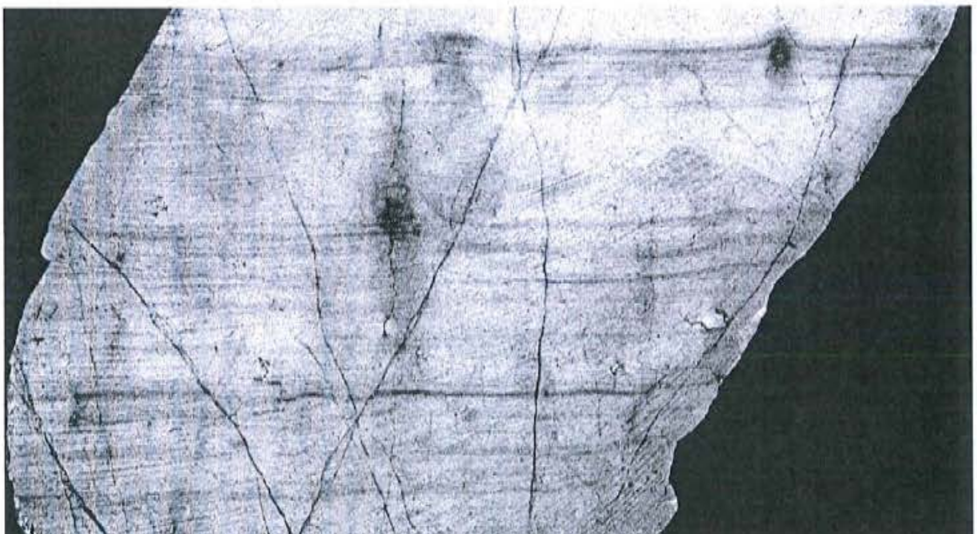

Figure 14

Core from MFB-7 (7570') showing fine-scale parallel lamination enhanced by the oil staining. The dark lines across the laminae are healed hairline fractures also enhanced by the oil stain. Core diameter seen here is 11 cm.

In core material from chalk of the Central Graben the hairline fractures occur both as swarms of small, mostly anastomosing fractures and as single fractures that cross the core. The fracture planes are more or less vertically orientated (dips are usually between 70° and 90°).

They are interpreted to be of relatively early origin, since they are cut by later tectonic fractures, stylolites, and stylolite-associated fractures. At the same time they are seen to cut primary sedimentary structures, such as laminae and trace fossils,. Oil stained hairline fractures are easily seen in chalk cores from the oil zone, whereas they are practically invisible to the naked eye in chalk from the water zone and the gas zone, unless the core surface is moistened with oil or water. Stronger capillary forces seem to act on the fluids in the hairline fractures compared to the surrounding matrix, indicating that the porosity (or maybe only the pore-size range) is lower here.

In outcrop chalk the hairline pattern is only visible if the Bushinsky technique is used to enhance the visibility of the features. This technique (Bushinsky 1947; Bushinsky & Shumenko 1979) has been revived (Bromley 1981) and applied to an outcrop chalk from the uppermost Maastrichtian clearly brings out a complex pattern of hairline fractures (Fig. 15).

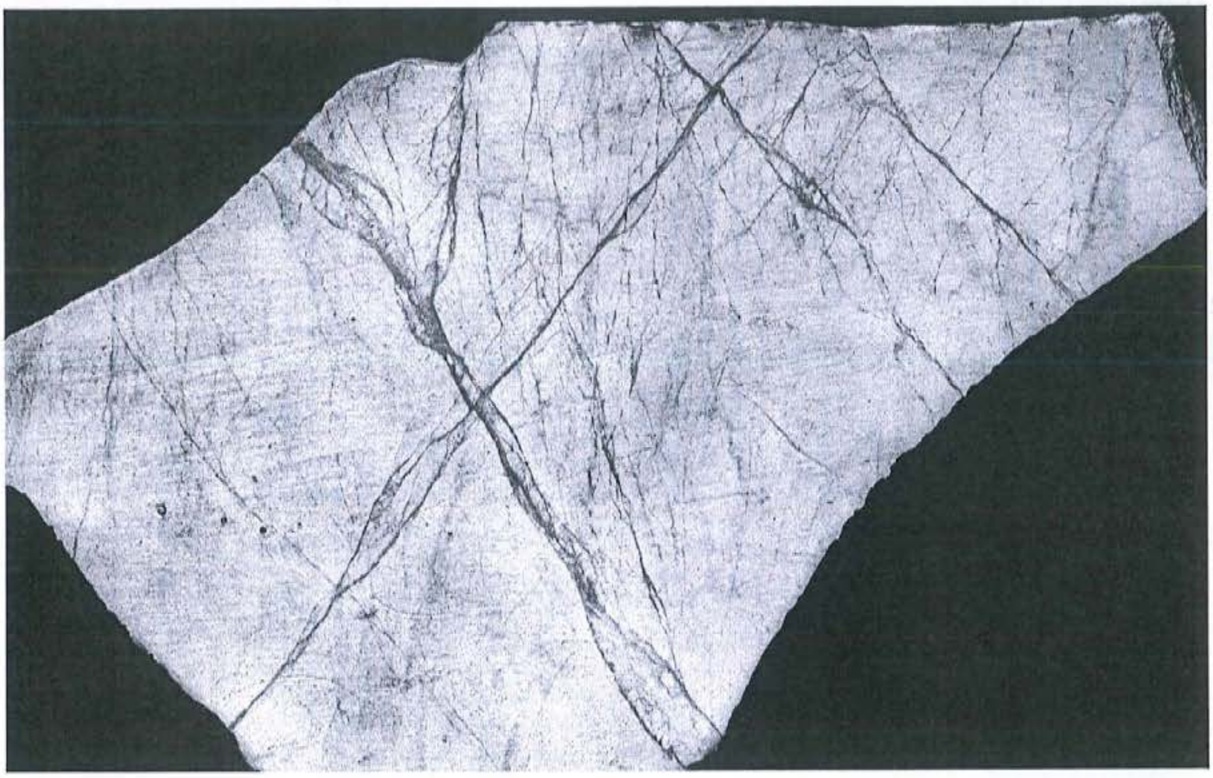

Figure 15
Vertical slice 16 cm across in outcrop chalk from Stevns in the uppermost Maastrichtian clean chalk. The Bushinsky technique has been applied using a light handyman oil. The complex pattern of hairline fractures includes zones of mylonitic nature with small chalk intraclasts.

The width of the hairline fractures varies a lot from about 15 μm to about 4 mm, but most of them are less than 200 μm in width. When observed in thin section under a light microscope it is clearly to see that the hairline fractures are not well-defined: at low to moderately high magnifications they appear as blurred lines or ribbons, and when highly magnified they are usually impossible to distinguish from the surrounding micrite of the rock matrix.

Origin

The prediction that hairline fractures show lower porosity than the surrounding has been confirmed by backscatter electron imaging (BSE) of polished samples from a specific case study (Dons *et al.* 1995). A decrease of about 10 % in the area representing pore space is observed when the interior of hairlines is compared to the surrounding matrix. The grains of the hairline fractures are obviously more densely packed compared to the grains of the surrounding undeformed chalk. The lower porosity of the hairlines is not due to a precipitation of calcite cements, as there is apparently no variations in cementation of the hairline and the surrounding matrix. These circumstances speak in favour of a very early formation of the hairline fractures, being related to an early dewatering of the sediment, after the original lime ooze was somewhat compacted and consolidated.

Analysis

The fact that hairline fractures act as rather indistinct, thin layers of relatively more densely packed, low-porosity micrite is also demonstrated by both X-ray CT-scanning and NMR (Nuclear Magnetic Resonance) scanning studies.

From the description of the origin given above it is likely that a sample with subvertical hairline fractures will show a measurable permeability heterogeneity, the permeability in the direction parallel to the surfaces of the hairline fractures being a little higher than the permeability in a direction at right angles to the surfaces. This has been supported by the investigation of cube material reported in another chapter.

DISSOLUTION SEAMS AND FLASER STRUCTURES

Description of feature

Flaser chalk has been described as composed of ellipsoidal bodies or lenses of chalk surrounded by clay-rich solution seams (Garrison & Kennedy 1977). They note that the latter may be simple, individual clay partings or composite aggregations of clay partings. They further conclude that the flaser structures formed during late burial diagenesis in response to mechanical compaction and pressure dissolution of calcium carbonate, and they note that the most probable range of burial depths at which the flaser structures formed in chalks was approximately 300 – 2000 m.

A distinction was made between stylolites and dissolution seams (Bathurst 1987). He defined a stylolite as a serrated interface between two rock masses, in cross section of sutured appearance. The amplitude of the suture is greater than the diameters of the transected grains, and it cuts indiscriminantly through the rock fabric. In contrast, dissolution seams are smooth, undulating, and lacking in sutures. It was also described that dissolution seams are typical of argillaceous carbonate sediments (with more than 8% - 10% clay), whereas in purer carbonates stylolites form.

Flaser structures has been described in chalk from the deep sea in several carbonate sites. In the Ontong Java Plateau of the western equatorial Pacific they are found below burial depths of 490 m (Lind 1993).

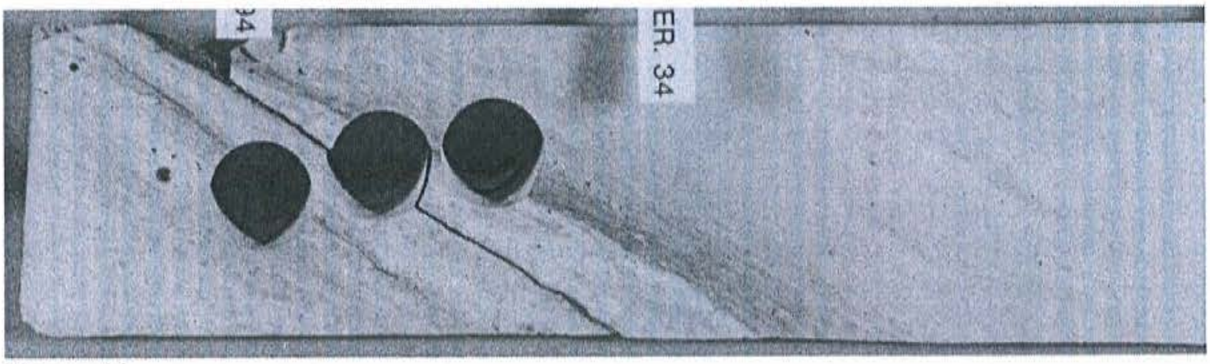

Figure 16

Core-slab, MFA-13 Dan Field, Danian D2b, In the left part is seen short and isolated clay flasers. In the middle a layer with primary generally high content and concentrate of insoluble residue.

Effects

The porosity of a flaser structure has been mapped around a flattened burrow from the Dan field chalk (Lind & Grøn 1996). The porosity was mapped by the microprobe and compared to the porosity of the burrow and a stylolite. The porosity measurement was combined with areal chemical analysis. It was found that the porosity of the dissolution seam (20%) was distinctly lower than the porosity of the burrow (30%), whereas the volumetric calcite content was less reduced in the dissolution seam compared to the burrow (Lind & Grøn 1996). The porosity difference was thus due to a packing of clay particles around the carbonate particles of the dissolution seam. By contrast the carbonate content of the stylolite was markedly low as compared to the surrounding chalk

STYLOLITES

Description of feature

Stylolites are common in the chalk of the North Sea, where they are generally moderate in size with amplitudes commonly around a few millimeters and rarely exceeding a few centimeters (Fig. 17 and 18). The drape covering the irregular stylolite surface rarely exceeds half a millimeter in thickness and is primarily composed of clay minerals (illite, kaolinite and in some cases smectite), pyrite and dolomite. The two latter minerals occur as euhedral crystals. The drape may be enriched or impoverished in quartz relative to the surrounding matrix (Lind 1988; Lind & Schiøler 1994). Pyrite and smectite are thus the primary colouring agents.

Along the stylolite the carbonate has been dissolved away, and because the amplitude of the wiggly surface usually is parallel to the major stress axis, the stylolite formation is described as a process of pressure dissolution (Bathurst 1975), and a distinction was made between stylolites and dissolution seams (Bathurst 1987). He defined a stylolite as a serrated interface between two rock masses, in cross section of sutured appearance. The amplitude of the suture is greater than the diameters of the transected grains, and it cuts indiscriminately through the rock fabric. In contrast, dissolution seams are smooth, undulating, and lacking in sutures. It was stated that dissolution seams are typical of argillaceous carbonate sediments (with more than 8% - 10% clay), whereas in purer carbonates stylolites form (Bathurst 1987).

Stylolites occur in the chalk of the North Sea area, where it is or has been subjected to sufficient effective burial (Lind 1998). Studies of deep sea chalk on the Ontong Java Plateau indicate that stylolites form below an effective burial of c. 800 m (Lind 1993). Several authors (e.g. (Merino *et al.* 1983; Guzetta 1984)) interpreted the process of stylolite formation as a self-organising process in a homogeneous chalk/ clay mixture, where the localisation of stylolites is ruled by statistics. This model has the advantage that the amount of dissolved chalk can be assessed by the drape thickness. By contrast, from studies of stylolites in deep sea carbonates it was also found that chemically distinct primary sedimentary structures can act as localising agents for stylolite formation (Lind 1993), in line with the hypothesis of (Heald 1959). These factors include trace fossils and other features with an anomalous pyrite or silica content, which can trigger stylolite formation. For this reason stylolites have an overall horizontal orientation in areas with a conservative tectonic history dominated by burial. In areas with a more dramatic tectonic history as e.g. above a salt piercement structure, slickensided fractures with clay drape may develop into stylolites with any overall orientation, but generally with vertical local amplitude. This latter type of stylolite is frequently accompanied by frequent more or less cemented centimetre long stylolite fractures (Brewster *et al.* 1986). The fractures are generally oriented in the direction of the local stylolite amplitude. Stylolite-associated fractures are also developed at horizontal stylolites (Lind *et al.* 1994). In some papers stylolite fractures are referred to as "tension gashes". The term "stylolite fractures" is less interpretative and is the preferred term for the described features.

Observation in cores and wells

Stylolites and stylolite fractures were described from the Ekofisk (Brewster *et al.* 1986), in the Albuskjell field (Watts 1983), in the Gorm field (Hurst 1983), and in Tommeliten Gamma (Nielsen *et al.* 1990), whereas no stylolites seems to be described from the high porosity chalk of the Tor Formation in the Valhall field.

In the Eldfisk field, an overall trend of increasing stylolite abundance with burial depth is reported, and with the stylolites being most abundant in the layers with more insoluble residue of the Hod Formation (Maliva & Dickson 1992).
On a more detailed scale, stylolite abundance also vary within m-scale porosity cycles (Scholle *et al.* 1998), where the low-porosity cycle tops have the highest frequency of stylolites compared to the underlying high porosity cycle bases.

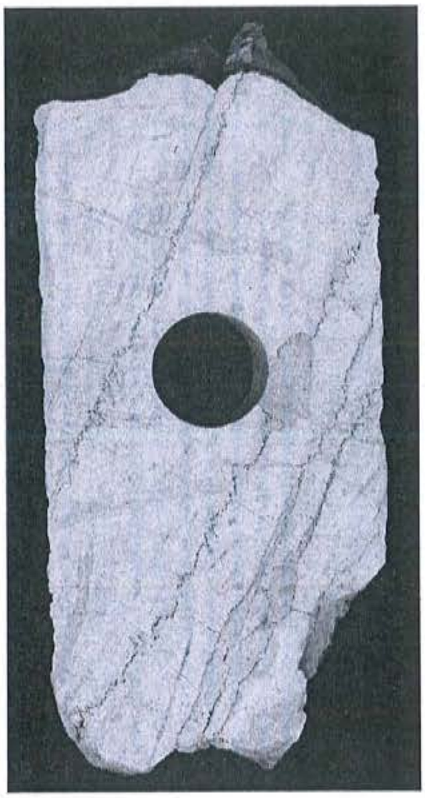

Figure 17
Core slab from MFA-16, horizontal well in the Dan Field, core 2, core-depth 8514'6"-8515'1". Plug hole seen is from horizontal plug no. 79, in same interval vertical plug no.19. Slab width 9 cm. Several stylolites are seen to traverse the core, and the geometry of the trace fossils and other features indicates that the stylolites are formed parallel to the original bedding. JCR coredescription of slab: M,Ch,Gn,Bn,Lpl,Dn,Th,Hm,Chi,Sh,Fhl.

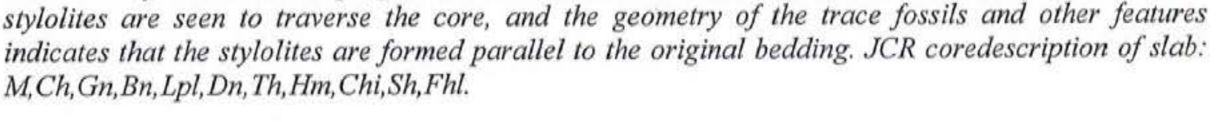

Figure 18
Enhanced contrast image of one of the stylolites in Fig.17. 16 cm long section. Stylolite is seen to be bounded by a darker coloured trace fossil.

The illustrated example is only one, although typical development of stylolites in chalk. Stylolites with larger amplitudes are often seen, and thicker residues, mainly clay, are also observed. The association with tensional fractures being perpendicular to the stylolite is a fairly common phenomenon in some sequences.

Size and geometry

Stylolites are mostly found to be parallel to the original bedding , and can be areally extensive. They can sometimes be developed along fracture planes and therefore in these cases of limited extent.

From studies of core-scanning and logging data (from Choquette (1965) and Dunnington (1967) in (Bathurst 1975)), it has been repeatedly stated (e.g. Bathurst 1975) that stylolites have a negative effect on porosity due to a cementation along the stylolites. However, cementation along stylolites has not been documented in North Sea chalk and neither in deep sea chalk (Lind 1993). As observed by several authors *e.g.* Koepnick (1984) and recently by Scholle *et al.* (1998), stylolites may be relatively frequent in less porous intervals. But a local effect on porosity near the stylolites is more questionable. Electron microscopy and microprobe mapping on mm-scale, has revealed no systematic relation between porosity and distance from the stylolite, nor even a systematic effect on porosity between chalk matrix and clay drape (Lind 1988; Lind 1991; Lind & Grøn 1996).

Permeability effects

Several authors have stated (e.g. Bathurst 1975) that stylolites have a negative effect on vertical permeability because of the clay drape. A negative effect on vertical permeability would seem logical, but has not been documented. In earlier studies, no measurable effect was found of stylolites from the Gorm field (Lind *et al.* 1994) or an unspecified North Sea field (Tobola *et al.* 1998). By contrast it has been reported in an abstract that in a salt diapir field in the North Sea, dissolution seams have developed with a thickness up to 20 cm (Safiricz 1998). He estimates that 50% of the chalk has been dissolved away and states that the seams can hold back up to 500 psi overpressure. Unfortunately the abstract does not include any documentation.

Stylolites on the other hand have a positive influence on permeability when associated with fractures (Brewster *et al.* 1986; Lind *et al.* 1994). The permeability effects of stylolites have been investigated by extracting plugs of different orientation from core material with stylolites (Lind *et al.* 1992; Lind *et al.* 1994). Their conclusion was that at restored reservoir stress no effect could be measured from the stylolites on permeability anisotropy.

When the stylolites were associated with stylolite fractures, the permeability along as well as perpendicular to the stylolite was enhanced relative to the matrix permeability (Lind *et al.* 1992; Lind *et al.* 1994).

For the present investigation, material with thin and low-amplitude, but very typical chalk rock stylolites, has been extracted for investigation with minicube measurements.

From M-2x, Dan Field, core 2, box 1 and 13, has been extracted core pieces from which minicubes of 15 mm sidelength have been cut. The core is in full-core state, and only a superficial core description is therefore available

Sample 1 is from 6446 ft, Stylolitic chalk, M,Ch,Gn,Bn,Ln,Dn,Tn,Hs,Cm,Sm,Msi,Fhl.

Sample 2 from 6411.5 ft. Chalk with few stylolites, Ch,Gn,Bn,Ln,Dn,Tn,Hs,Cm,Sl,Mn,Fn.

Difficulties in cutting and fracturing of the cubes during measurement only leave three cubes that have been measured successfully, although two of them probably have given erroneous results as judged from the permeability measurement itself.

The minicubes extracted from sample 1 is named 1.21 and 1.22, and from sample 2 is cut minicube 13.22.

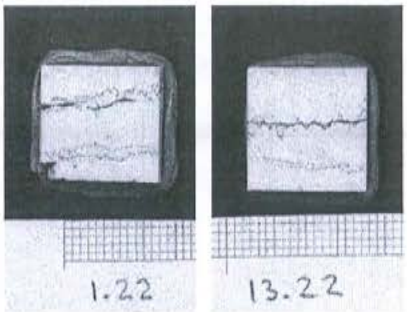

Figure 19 A and 19 B
Minicubes 1.22 and 13.22 showing stylolite and the fracture caused by the core analysis procedure.

A stylolite from the minicube is displayed as seen in the backscatter electronmicroscopy in figure 20. No local low porosity was observed along the stylolite, but the stylolite apparently separates a less porous layer (above) from a more porous (below).

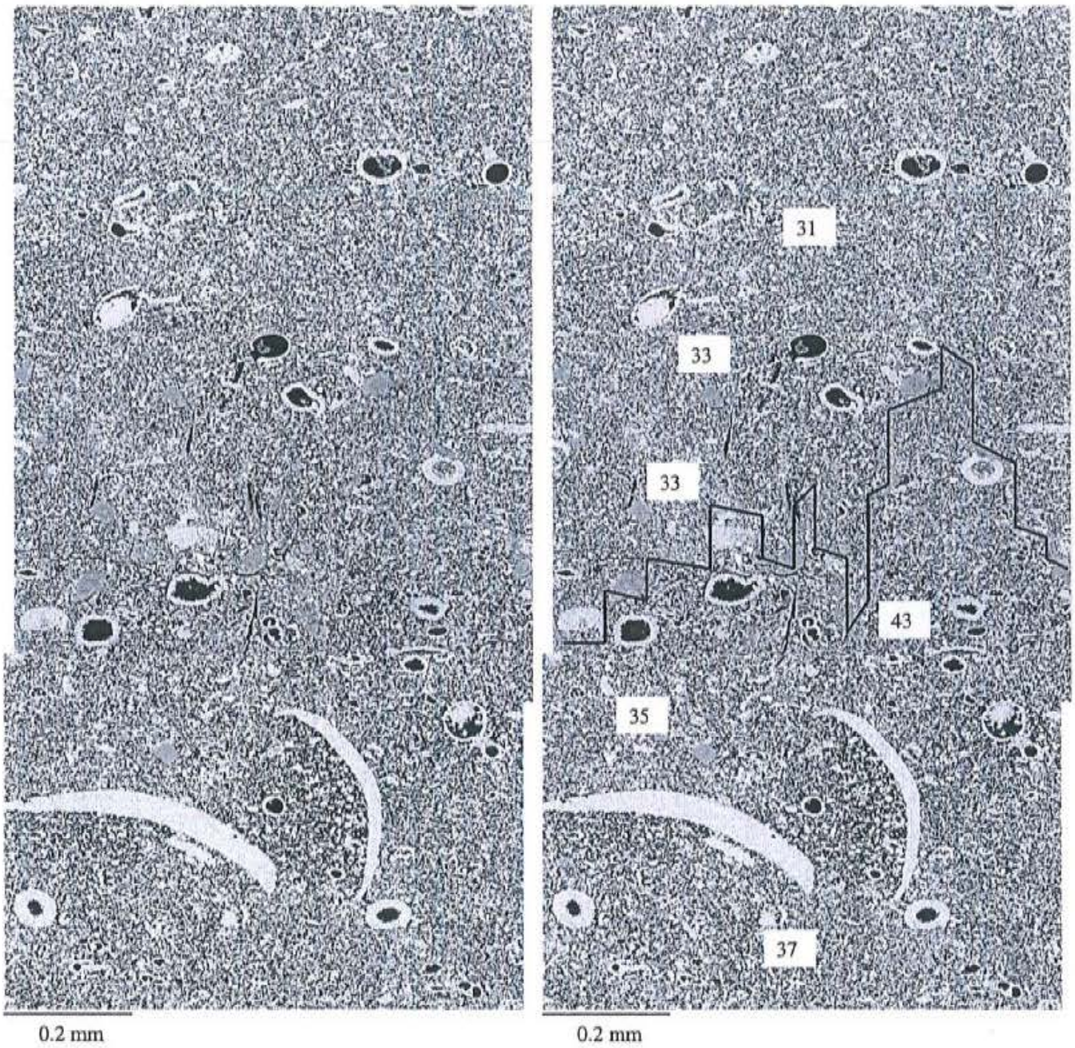

Figure 10
A: Backscatter electron micrograph of stylolite-bearing chalk sample from the Dan field. Please observe euhedral dolomite crystals (grey) and pyrite (white) along the stylolite, and please also observe the high porosity sheltered by shell fragments in the lower part of the image. B: The stylolite is here outlined and local porosities (in percent) are indicated as measured image analysis of large scale micrographs (by L. Gommesen, DTU).(The image was recorded at DTU by F. Kragh and I. Fabricius).

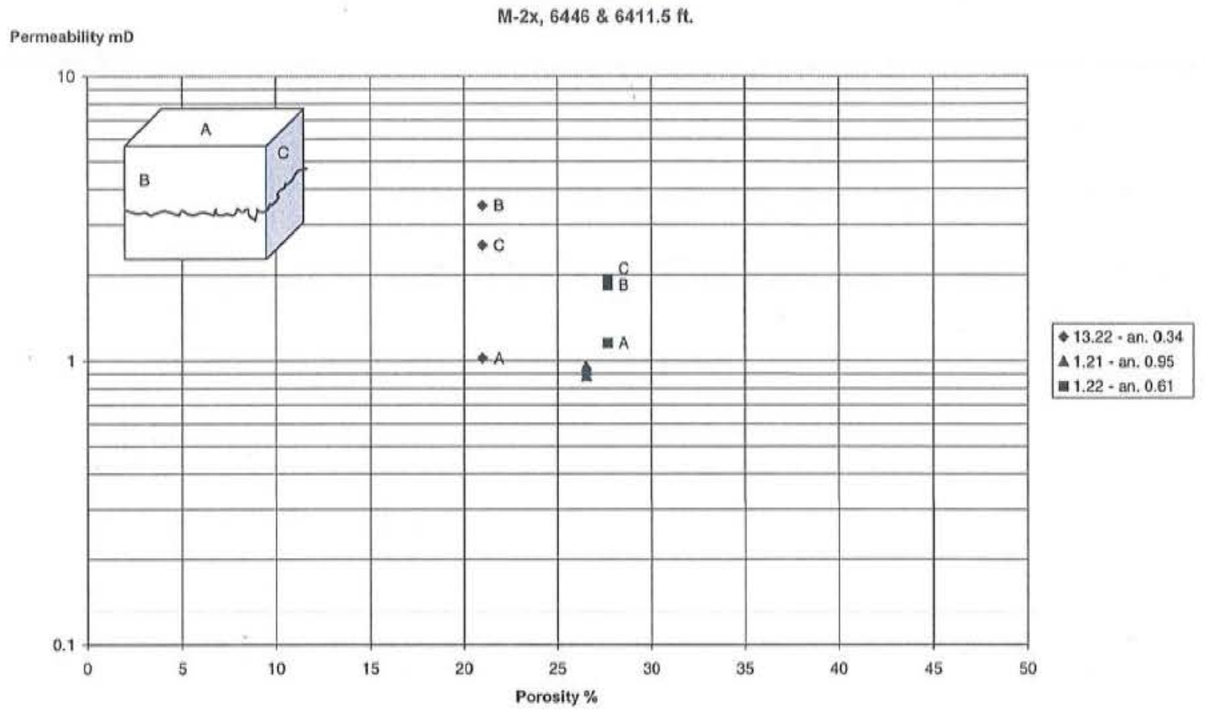

Figure 11
Diagram of the porosity-permeability measurements from three minicubes extracted from the M-2x core material. The cubes all have a stylolite seam across the cube which has 15 mm sidelength.

Interpretation

The porosity-permeability measurements from all three cubes are plotted on figure 21. The measured permeabilities in the A-direction ("vertical" – across the stylolite) all seem to match standard matrix properties for this type of chalk. Therefore, the high permeabilities for the B and C directions (parallel to stylolite) for samples 13.22 and 1.22 could indicate that the stylolite have separated slightly during handling, and that these values therefore are erroneous. The sample 1.21 have been robust enough to give nearly equal values for the three directions. This is interpreted as indicating that this particular type of stylolite does not have any effect on the permeability anisotropy.

Representativity

The analysed examples are endmembers in the wide range of stylolites known. The amount of clay residue and local cementation is not developed to an extent having permeability effect.

Recommendations

Other samples with more developed stylolites with thicker residue have been searched for, but sofar unsuccessfully. Often these stylolites are very fragile and prone to splitting of the material along the stylolite. It is therefore difficult to envisage direct measurements of these types of stylolites.

STYLOLITE-ASSOCIATED FRACTURES

Description of feature

The fractures usually form sub-parallel, anastomosing networks, where the fractures mostly have less than 0.1 mm aperture. The fractures are sometimes filled partially with calcite along the fracture surfaces, and can in these cases be up to 2 mm wide (Andersen 1995). Within each network the fractures are well interconnected. The lengths of the stylolite-associated fractures are usually shorter than the distance between individual networks. They form bedding parallel (sub-horizontal) zones of enhanced permeability, but do not form a pervasive network throughout the formation unless they occur in combination with the tectonic fractures. From the Albuskjell Field and the Ekofisk Field they are reported to be more abundant in the Tor Formation than in the Ekofisk Formation (Watts 1983; Teufel & Farrell 1990), and likewise more abundant in the upper part of the Maastrichtian than in the Danian in the Dan Field (Jørgensen 1993).
One example from a core in the N33 well from the Gorm Field illustrates the geometry and relation to the stylolite seam (Fig. 22).

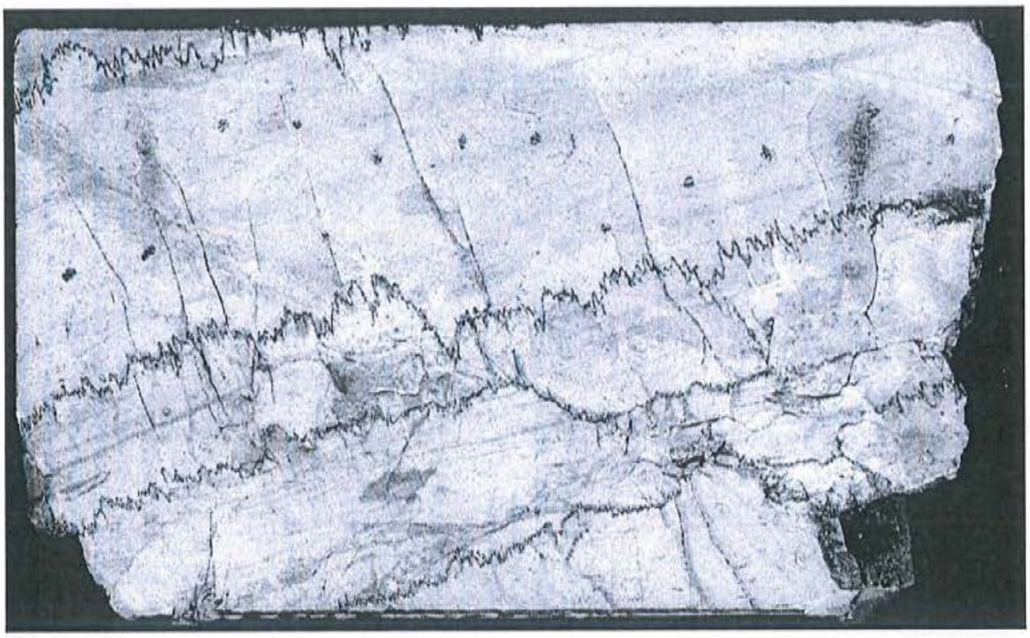

Figure 12
N-33. 8836'6". Slabbed near-horizontal core. The stylolite seams are bedding-parallel, and the stylolite-associated fractures extend perpendicular to the stylolites, with the width tapering away from the stylolite. Core diameter 10 cm (vertical on image).

Effects

Stylolite-associated fractures contribute to the reservoir permeability (Teufel & Farrell 1990; Lind *et al.* 1994). Lind *et al.* (1994) studied five samples from the Gorm field containing stylolites and stylolite associated fractures and compared these to five matrix samples and three samples containing stylolites with no stylolite associated fractures. Plugs were drilled along and perpendicular to the stylolites and porosity as well as permeability under reservoir stress was measured. They found that samples with stylolites without fractures have the same porosity-permeability relationship as samples with matrix only. They also found that for samples with stylolite associated fractures, the permeability along the stylolite was increased from c. 1mD to c. 15mD at a porosity of 28% and from c. 0.7mD to c. 2.5mD at a porosity of 24%. The effect on the vertical permeability was smaller: from c. 1 to c. 3mD at a porosity of 28%, and no significant effect at a porosity of 24%.

Analysis

In an attempt to investigate the 3D geometry of the fracture network of stylolite-associated fractures, CT-scanning has been applied to the core piece shown in Figure 23.
The investigation was only partly successful due to the very narrow nature of the fractures. Even though some parts of the fractures can be recognised on the CT-scan images, they appear to occur both as partly open and partly cemented, as attested by the either low or high density contrast to the porous chalk matrix (Figs. 23,24,25)

N-33, 8836'6", Core diameter 10 cm
80 slices, each 2 mm thick = 160 mm data
End of core piece   Slabbed core investigated with CT

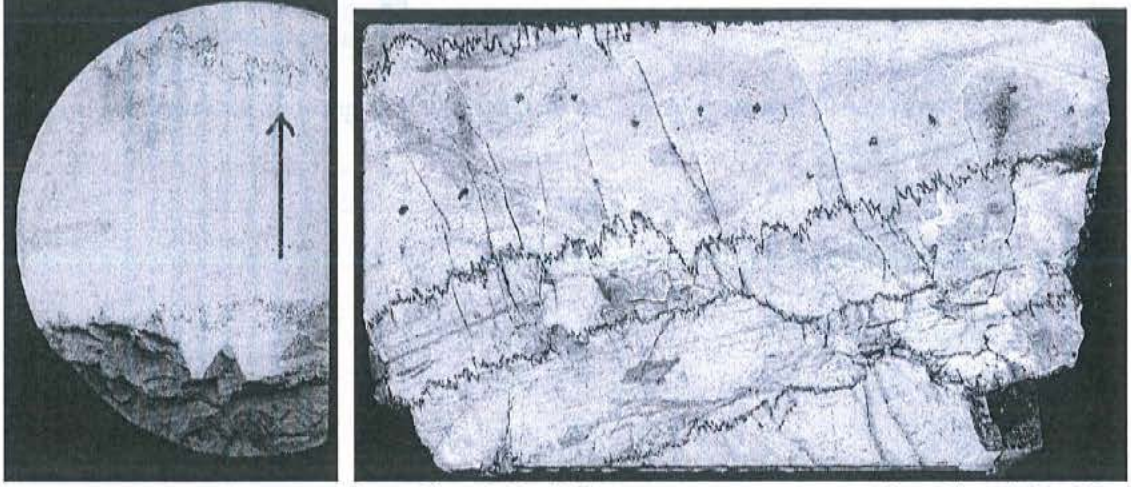

Last slice: TP –129 mm   First slice: TP +29 mm

Figure 23

Two photos showing configuration of the core piece investigated with CT-scanning. The CT images show slices from the end face and through the whole core. Each slice covers 2 mm thickness, and TP denotes the table position in mm.

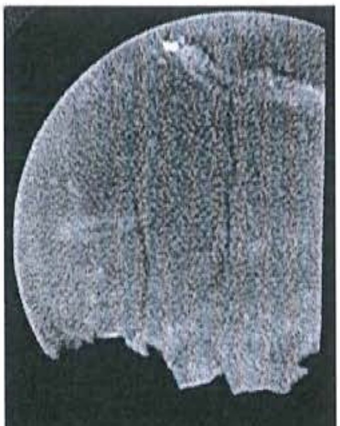

slice tp –127 mm

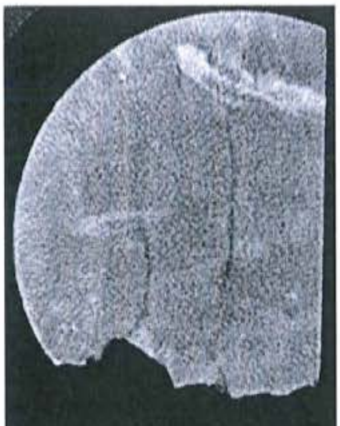

slice tp –125 mm

Figure 24

Two adjacent CT-scan images right inside the core from the end-face in Fig. 23. The open stylolite-associated fractures are slightly darker than the chalk matrix due to their slightly lower density. The light (more dense) areas are probably trace fossils with a lower porosity.

FLINT LAYERS

Description of feature

The studies on flint that has been published has mostly been carried out on outcrop material, whereas the sparse occurrences in core material has not been subjected to any systematic studies.

Flint nodules are common in the chalk sequence and are products of chemical segregation of dissolved silica originally derived from the dissolution of biogenic silica in the chalk deposits.

A minority of flints are associated with body fossils of echinoids, oysters, sponges etc. and found scattered in the chalk section. However, apart from these occurrences and Paramoudra flint (barrel-shaped flint), black flint nodules are normally concentrated in discrete bands or layers. The thickness of the layers seems to be proportional with the intensity and size of flint nodules.

The horizons of black flint as seen in outcrops occur characteristically at irregular intervals, approximately at ½ to 2 metres apart. The flint horizons present a wide array of bed-to-bed morphological variations. In some the nodules are sparsely scattered along single planes or within a finite unit of chalk. Other horizons may have been heavily silicified.

The morphology of the flint nodules often mirror the initial silicification in burrows, most commonly found as *Thalassinoides* burrow galleries (Bromley & Ekdale 1983). In layers with low intensity the flint may occur as slender finger-like nodules in isolation. In higher intensity layers the nodules may interconnect as a network of boxwork or may fuse into massive nodules. In rare cases massive platy flint layers of thicknesses in the order of 10-20 cm may be developed.

Origins

The formation of flint takes place over a long period of time and can be divided into several phases. The first phase starts very soon after deposition, where an embryonic situation is found at a certain depth below sea floor where redox conditions prevail and organic matter provides adsorption nuclei for silica. The depth of the "redox boundary" is quite variable and depends on the sedimentation rate and the major development of flint nuclei may respond to the duration of time for non-deposition periods. The longer the period of non-deposition the deeper the zone is located. No rigid nodules are formed in this early phase, but only an interval with nucleations for subsequent silica accumulation and reprecipitation are formed.

At a later stage dissolution of silica from the matrix takes place and migrates to the embryonic zone where it precipitates and initiates a fine scale replacement of skeletal calcite. This process continues in the main stage of growth by intense precipitation of opal-CT lepispheres. Reworking of the flint at this stage serve only to disaggregate the lepispheres because these are not firmly cemented until the phase of interstitial opal-CT chalcedony precipitation (Clayton 1983).
During late diagenesis the opal-CT protoflint recrystallised to its present state as alpha-quartz mineralogy (Clayton 1983).

The origin of flint is primarily associated to the silica released from disintegrated silica sponges. In outcrops there seems to be an inverse relationship between number of flint nodule layers and presence of preserved sponges.

The appearance of flint seems to be controlled by depositional environment and is dominant in the more basin marginal deposits where silica sponges are assumed to have been abundant. In more basin central deposits the flint deposits also are seen, but are less frequent and appears with generally smaller nodules.

Outcrop observations

A flint layer from the Stevns Klint has been measured in detail over a distance of 10 m (figure 26). The investigation forms a preliminary attempt to quantify the volumetric occurrence of flint. The thickness of the layer is in the order of 15-20 cm and comprises up to 80% flint nodules. Both finger-like nodules and larger fused nodules are observed. The specific flint layer is the prominent layer formed in connection with the omission surface associated with the change from the white to the grey chalk lithology at Stevns. This horizon has been interpreted as related to a sequence boundary (Håkansson & Surlyk 1997; Surlyk 1997; Surlyk & Håkansson 1999). It is also seen from figure 26 that both the size and the connection of nodules are very variable in lateral direction.

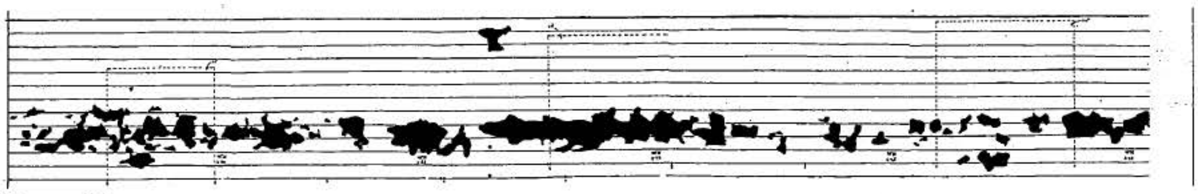

Figure 26
Vertical section in the flint layer ca. 3-4 m below the Maastrichtian/Danian boundary at Stevns Klint. The total section covers 9.5 meters, and shows the very variable distribution of nodules as well as the variable size of the individual nodules and their connectednes. (Flint layer measured and drawn by Jens Jacob Gørtz, Anne Kristensen og Christian Uttenthal 1999 (DTU)).

In the zone of recrystallised and replaced flint nodules virtually no porosity and permeability will be formed. However, between the nodules porous chalk is present and from outcrop observations the chalk within a flint zone is generally of higher porosity than the surrounding chalk.

Representativity

The flint layers as described from outcrop analogues can only be transferred to reservoir situations by means of general outline. The frequency and size of the nodules are not necessarily comparable, which can be due to the reduced availability in biogenic silica as sponge lepispheres, radiolarian tests, diatoms etc. in the environments where the reservoir chalk sequences were deposited

In most off-shore wells flint occur as nodules associated with a flint layer of some unknown lateral extension. It is, however, anticipated that the lateral extension may be comparable to outcrop observations. Horizons of platy flint are not common in the Central Graben chalk.

Observations in cores and wells

In off-shore wells flint nodules are found scattered in the chalk sequence with a dominance in the Danian.

In the clean chalk formations as in the Maastrichtian very little flint and only few flint layers are observed. The flint nodules are of limited size and are found as isolated rounded elements in the cores.

In the tight lower part of the Danian chalk, the flint layers occur at intervals ranging from 15 to 30 cm and are interbedded with a rock matrix comprising relatively high content of clay and dispersed silica. The flint nodules can be larger than the core diameter, but this does not necessarily mean that a massive flint interval in a core represents a platy flint layer. From outcrop data it is more likely that the observed flint only are associated with a nodule of limited lateral extension.

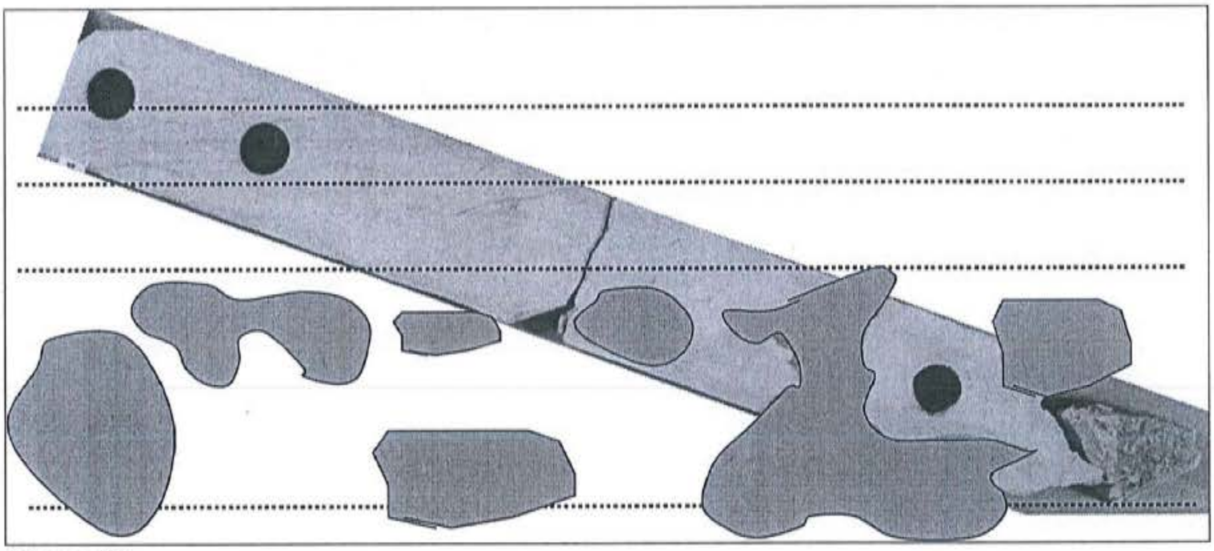

Figure 27
Core from MFA-13, Dan Field, Core-2 6767'5"-6769'8", upper Danian. The sub-horizontal core shows vague indications of bedding and parts of flint nodules which are extrapolated to mimic flint morphology.

Size and geometry

Adopting the observations from chalk outcrops analogues the flint recognised in the cores consist of solitary nodules of varying sizes. The distance between nodules varies from 1 to more than 10 cm and they are separated by a porous chalk.

The accumulation of flint nodules may act as a sealing or permeability reducing layer but with local chimneys with relative high porosity and permeability allowing vertical flow.

Porosity effect

The dissolution of the organic silica particles in the matrix and the recrystallisation and replacement of calcite in discrete zones give rise to a relocation of the porosity. In case of a general content of 10% silica in the bulk volume of the matrix, it will affect the porosity significantly (increase the porosity with a factor of more than 1.5).

Permeability effect

Although the presence of flint layers in a formation would be expected to have an effect on the vertical flow, the effect is not as dramatic as intuitively predicted. The effect on permeability anisotropy has been quantified with flow simulation of a small model example (Fig. 28)

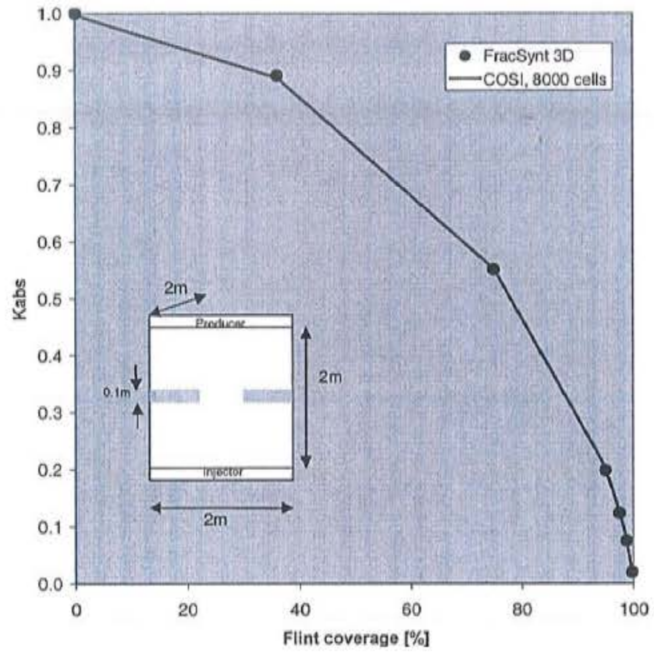

Figure 28

Diagram showing the results from two different flow simulators of the effective permeability in the vertical direction as a function of the flint layer coverage in %. The model used for the simulation is sketched in the diagram as a cube with 2 m sidelength. The flint layer is 10 cm thick, and the hole in the middle is varied as shown in the crossplot. The analytical solution of the same problem gives higher permeability values if harmonic average is used. The difference is caused by the flow simulation correctly accounting for the flow pattern in the model.

From Fig. 28 it is seen that even a coverage of a horizon of 80% by a tight flint layer, only causes a reduction in permeability from 1 mD to 0.4 mD, leading to a k_V/k_H of 0.4. This amount of coverage is considered far too large, and an estimate of 30% coverage would only give rise to an anisotropy of 0.9.

Recommendations

In addition to the layers of black flint, discrete intervals with nano-silica (μ-size particles of α–quartz interpreted to have precipitated and flocculated directly in the free water phase and sedimented in the same way as the coccoliths) are found in the Danian sequence (Jakobsen et al., in press). Visually the intervals with nano-silica appear as chalk but comprises up to 80% silica affecting the bulk density. Conventional petrophysical measurements indicate a slight decrease in porosity and also indication of decrease in permeability as compared to the surrounding chalk intervals.

The more uniform decrease in permeability of a discrete layer with nano-silica as compared to a flint layer may have some impact on the flow in the reservoir and should be studied in more detail in future work.

Another source of error caused by the nano-silica content is the change in bulk density. Since porosity is estimated from log data using bulk density, the actual changes in grain density may cause erroneous results to appear locally. It is therefore recommended in future work to examine the impact of silica rich intervals on the various test results.

References

Andersen, M.A. 1995: Petroleum research in North Sea Chalk (JCR), 179 pp. Stavanger, Norway: RF-Rogaland Research/JCR Phase IV.

Bathurst, R.C.G. 1975: Carbonate sediments and their diagenesis, 658 pp. Amsterdam: Elsevier.

Bathurst, R.G.C. 1987: Diagenetically enhanced bedding in argillaceous platform limestones: stratified cementation and selective compaction. Sedimentology **34**, 749-778.

Brewster, J., Dangerfield, J. & Farrell, H. 1986: The Geology and Geophysics of the Ekofisk Field Waterflood. Marine and Petroleum Geology **3**, 139–169.

Bromley, R.G. & Ekdale, A.A. 1983: Flint and fabric in the European chalk. In: Sieveking, G.d.G. & Hart, M.B. (eds): The scientific study of flint and chert. Proceedings of the fourth International flint symposium, Brighton Polytechnic, 10-15 April 1983 New York: Cambridge University Press

Bromley, R.G. 1981: Enhancement of visibility of structures in marly chalk: modification of the Bushinsky oil technique. Bulletin of the Geological Society of Denmark 29, 111-118.

Bushinsky, G.I. 1947: Textures and structures of Cretaceous chalk and flints (Russian with English summary). Bull. Soc. Natural. Moscow N.S. 52 (Geol.)(22), 37-43.

Bushinsky, G.I. & Shumenko, S.I. 1979: Writing chalk and its origin (Russian). Lith. Min. Deposits, Acad. Sci. U.S.S.R. 2, 37-54.

Clayton, C.J. 1983: The chemical environment of flint formation in Upper Cretaceous chalks. In: Sieveking, G.d.G. & Hart, M.B. (eds): The scientific study of flint and chert. Proceedings of the fourth International flint symposium, Brighton Polytechnic, 10-15 April 1983 New York: Cambridge University Press

Dons, T.D., Jakobsen , F. & Stentoft, N. 1995: Chalk diagenesis and reservoir properties - Dan Field case study. Danmarks Geologiske Undersøgelse Service Report **15/1995**.

Dons, T.D. & Olsen, D. 1996: Dan Field minicube study - porosity and permeability heterogeneity at core scale. (Report no. 8.Technical report for Joint Chalk Research program IV. Project no. 2.). Danmarks og Grønlands Geologiske Undersøgelse Rapport **62**, 65 pp.

Ekdale, A.A. & Bromley, R.G. 1988: Diagenetic micro-lamination in chalk. Journal of Sedimentary Petrology **58**(3), 857-861.

Farrell, H.E., Tobola, D.P. & Baldwin, B.A. 1994: A Study of the Geological and Flow Characteristics of Gouge-Filled Fractures and Stylolites in a north Sea Chalk. EAPG/AAPG Special Conference on Chalk, Copenhagen, Denmark, 1994, .

Garrison, R.E. & Kennedy, W.J. 1977: Origin of solution seams and flaser structure in Upper Cretaceous chalks of Southern England. Sedimentary Geology **19**, 107-137.

Guzetta, G. 1984: Kinematics of stylolite formation and physics of pressure-solution process. Tectonophysics **101**, 383-394.

Hancock, J.M. 1993: The formation and diagenesis of chalk. In: Downing, R.A., Price, M. & Jones, G.P (ed.): The hydrology of the chalk of North-west Europe, 14-34. Oxford: Clarendon Press.

Heald, M.T. 1959: Significance of stylolites in permeable sandstones. Journal of Sedimentary Petrology **29**, 251-253.

Hurst, C. 1983: Petroleum geology of the Gorm field, Danish North Sea. Geologie en Mijnbouw **62**, 157-168.

Håkansson, E. & Surlyk, F. 1997: D - Denmark. In: Moores, E.M. & Fairbridge, R.W. (eds): Encyclopedia of European and Asian Regional Geology, 183-192.: Chapman & Hall

Jakobsen, F., Lindgreen, H. & Springer, N. ; in press: Precipitation and flocculation of spherical nano-silica in North Sea chalk, Clay Minerals

Jørgensen, L.N. 1993: Dan Field – Denmark. Central Graben, Danish North Sea. In: Beaumont, E.A. & Foster, N.H. (eds): Atlas of Oil and Gas Fields, 199-215. Tulsa: American Association of Petroleum Geologists

Kennedy, W.J. 1987: Sedimentology of Late Cretaceous-Palaeocene chalk reservoirs, North Sea Central Graben. In: Brooks, J. & Glennie, K. (eds): Petroleum Geology of North West Europe, 469-481.: Graham and Trotman, London.

Lind, I. 1988: Stylolite formation. Unpublished Ph.D. thesis, Copenhagen University, Copenhagen, Denmark.

Lind, I. 1991: Microprobe Aided Mapping Of Areal Element Concentration And Microporosity In Chalk. Carbonates and Evaporites **6**(1), 45-51.

Lind, I. 1993: Stylolites in chalk from Leg 130, Ontong Java Plateau. Proceedings ODP Scientific Results **130**, 445-451.

Lind, I. 1998: Stylolites in the Chalk Formation of the North Sea as an indicator of burial and exhumation. 23. Nordiske Geologiske Vintermøde, Aarhus, 185.

Lind, I. & Grøn, P. 1996: Porosity variation in chalk. Zbl. Geol. Paläont. **H. 11/12**, 763-772.

Lind, I., Nykjaer, O., Priisholm, S. & Springer, N. 1994: Permeability of stylolite-bearing chalk. Journal of Petroleum Technology **46**(11), 986-993.

Lind, I., Nykjær, O., Priisholm, S. & Springer, N. 1992: Permeability of Stylolite-Bearing Chalk. Fourth North Sea Chalk Symposium, Deauville, France, 1992, .

Lind, I. & Schiøler, P. 1994: Dinoflagellate cyst concentration as an independent reference for monitoring mineral mobilization in stylolites. Sedimentary Geology **92**, 53-65.

Maliva, R.G. & Dickson, J.A.D. 1992: Microfacies and diagenetic controls of porosity in Cretaceous/Tertiary Chalks, Eldfisk Field, Norwegian North Sea. American Association of Petroleum Geologists Bulletin **76**(11), 1825-1838.

Merino, E., Ortoleva, P. & Strickholm, P. 1983: Generation of even-spaced pressure-solution seams during (late) diagenesis: a kinetic theory. Contr. Mineral. Petrol. **82**, 360-370.

Nielsen, E.B., Fraselle, G. & Vianello, L. 1990: Tommeliten Gamma Field - Norway Central Graben, North Sea Treatise on Petroleum Geology, Atlas of Oil and Gas Fields, 85-112.: AAPG

Safiricz, M. 1998: Structural evolution of Central Graben diapir fields, North Sea. AAPG 1998 annual meeting, Salt Lake City, UT, 17-20 May, 1998.

Scholle, P.A., Albrechtsen, T. & Tirsgaard, H. 1998: Formation and diagenesis of bedding cycles in uppermost Cretaceous chalks of the Dan Field, Danish North Sea. Sedimentology **45**(2), 223-243.

Surlyk, F. 1997: A cool-water carbonate ramp with bryozoan mounds; Late Cretaceous-Danian of the Danish Basin. In: James, N.P. & Clarke, J.A.D. (eds): Cool water carbonates **56**, 293-307. Tulsa, OK, United States: SEPM (Society for Sedimentary Geology)

Surlyk, F. & Håkansson, E. 1999: Maastrichtian and Danian strata in the southeastern part of the Danish Basin. 19th Regional European Meeting of Sedimentology, Copenhagen. Excursion A3.

Teufel, L. & Farrell, H. 1990: In Situ Stress and Natural Fracture Distribution in the Ekofisk Field, North Sea. Third North Sea Chalk Symposium, Copenhagen, Denmark, 1990, .

Tobola, D.P., Baldwin, B.A. & Farrell, H.E. 1998: Geological description and flow characterization of a North Sea chalk containing stylolites and a gouge-filled fracture. Society of Core Analysts Conference, The Hague, 14-16 September, (SCA-9832).

Watts, N.L. 1983: Microfractures in Chalks of Albuskjell Field, Norwegian Sector, North Sea: Possible Origin and Distribution. American Association of Petroleum Geologists Bulletin **67**(2), 201-234

Characterisation studies

Peter Frykman, Gert Andersen

CHARACTERISATION AND MULTISTEP UPSCALING OF FRACTURED CHALK RESERVOIRS.

JCR Phase V, Project no. 3

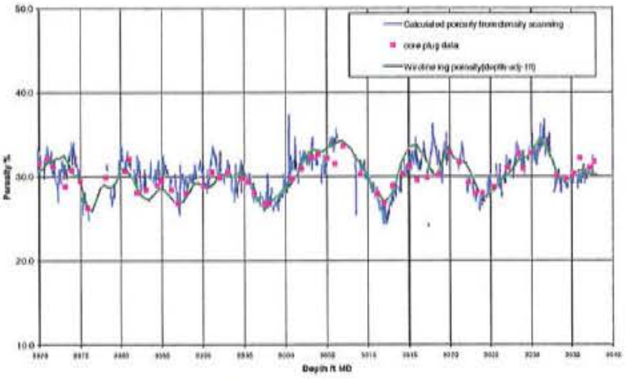

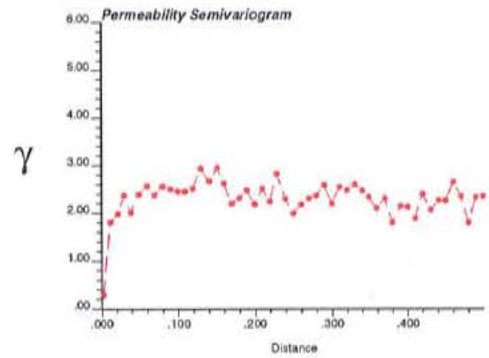

PERMEABILITY ANISOTROPY ANALYSED FROM HORIZONTAL AND VERTICAL CORE PLUGS

Introduction

It has for some time been the standard procedure for obtaining the k_V/k_H ration to compare measurements of plug samples taken in the two principal directions in the core material. This has given rise to very variable values for permeability anisotropy, but usually giving ratios around 0.7-0.8.

For the purpose of illustrating this method an example from the MFA-13 well on the Dan Field has been searched for suitable core plug material. This has been selected in an interval with abundant stylolites, and having 9 pairs of vertical and horizontal plugs that occur at same depth.
The porosity-permeability relation is shown in Fig. 29 to be well-behaved for the selected interval.

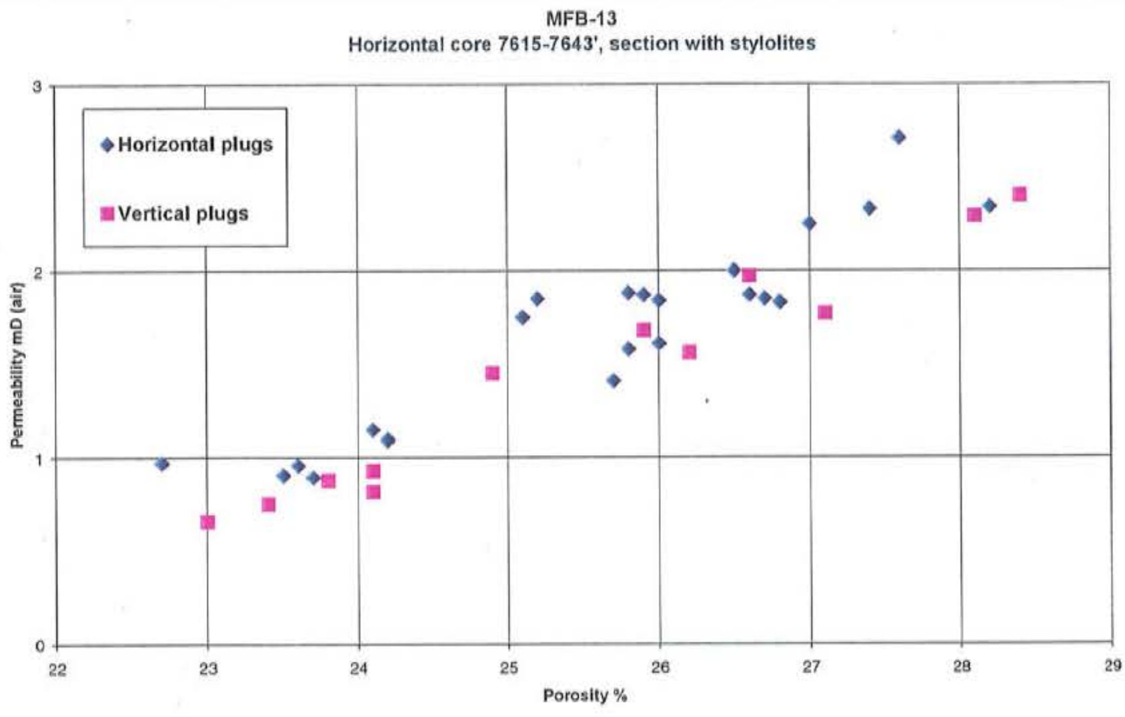

Figure 29
Porosity/permeability relation for plugs in the interval 7615-7645 ft. In the MFA-13 well.

The analysis of the plug-pairs give rise to an illustration of the k_V/k_H relation. Fig. 30.

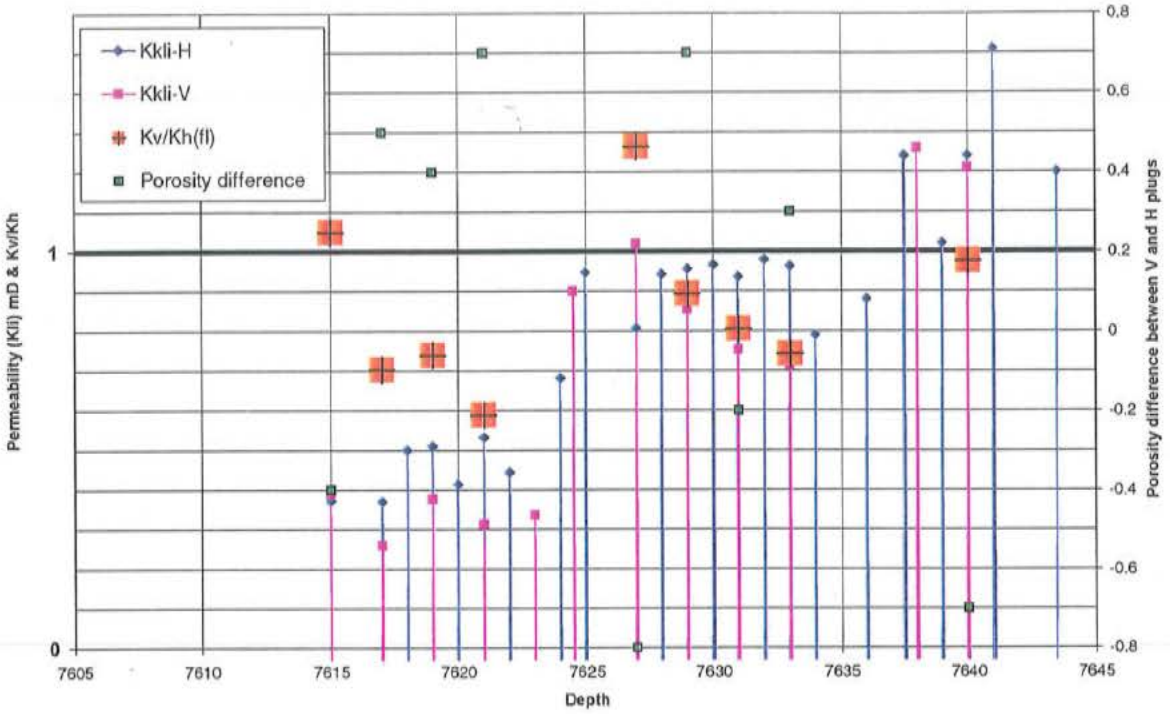

Figure 30
Illustration of the k_V, k_H and ratio k_V/k_H, and the porosity difference between the two plugs in the pairs. This last parameter is considered a quality factor for the present material, and shows porosity deviations below 0.8 porosity units between the two plugs.

The calculated anisotropy is quantified in Fig. 31.

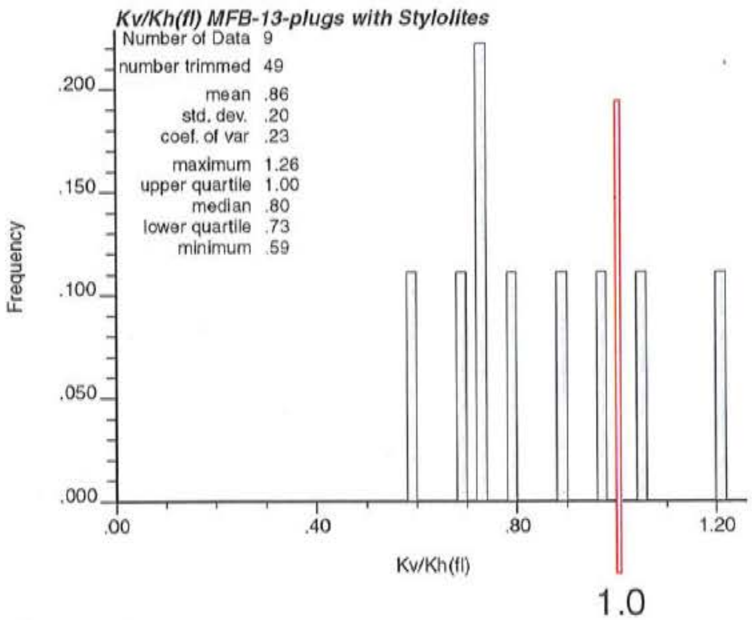

Figure 31
Histogram of k_V/k_H ratios for the 9 plug pairs in the investigated section.

Discussion

When comparing more closely the plug pairs and their properties, it is seen that in 5 out of the 7 cases with k_V/k_H <1.0, the permeability difference is due to a porosity difference and follows the normal trend line for the relation (Fig. 32, green arrows). 2 pairs have reverse porosity/permeability trend (blue arrows), and finally 2 pairs have k_V/k_H ratio >1.0 (red arrows).

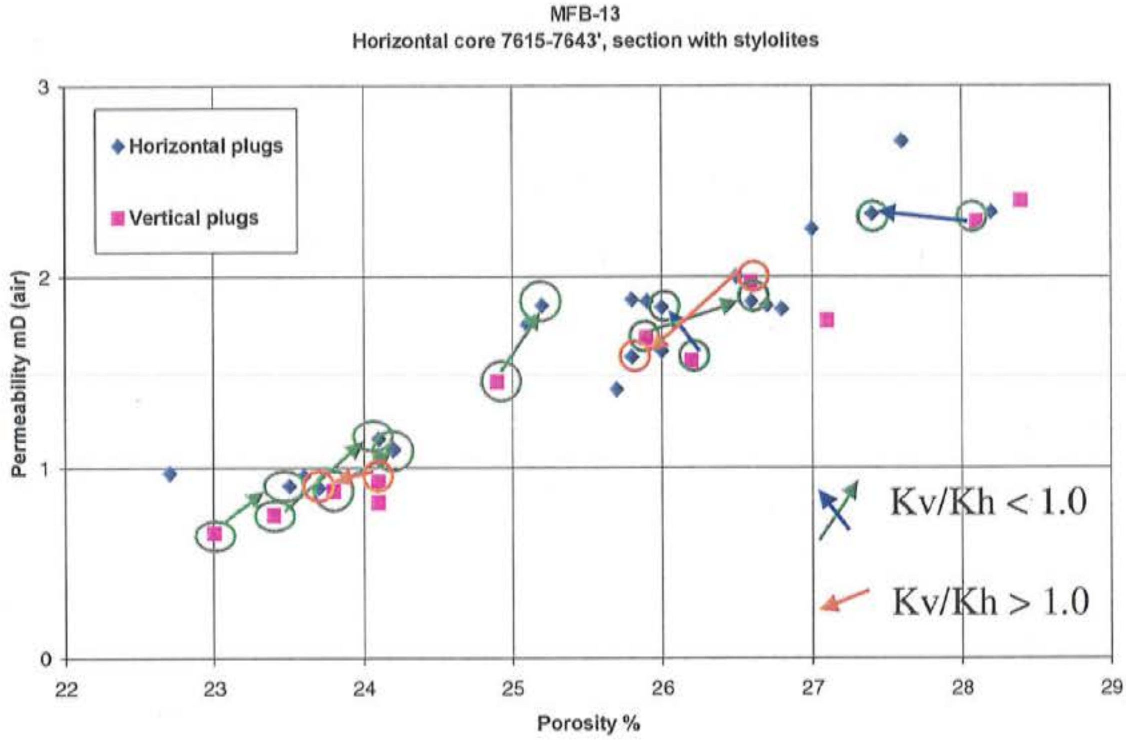

Figure 32
Annotated porosity-permeability plot of the plug pairs analysed.

That the majority of the plug pairs show a $k_V/k_H < 1.0$ is therefore purely incidental in this case, since most of the permeability changes can be explained by the porosity differences between the plug samples. A porosity change of only 1 p.u. is sufficient to create a permeability difference that is visible in the calculation of an anisotropy factor.
This analysis is therefore a warning about treating limited data sets without analysing closely the cause for permeability differences among samples. Only when samples are oriented properly as parallel and perpendicular to the small-scale heterogeneities studied, and the pairing of plug data is analysed closely, will this method give meaningful results for the k_V/k_H ratio.

PERMEABILITY ANISOTROPY ANALYSED FROM PROBE AND CORE ANALYSIS PERMEAMETER DATA

The probe permeameter data and conventional core analyses from the well N-22x have been analysed for variability and the resulting permeability anisotropy.

Material

The N-22x core material analysed ranges from the Danian/Maastrichtian boundary down into the Upper Maastrichtian. The interval analysed is located just above the 50% Sw level (Figs 33, 34, 35)

Probe (or mini-) permeameter

The data have been obtained from Mærsk Olie og Gas, and includes information on core coordinates, calculated permeabilities and pressure characteristics used. The state of the core material and the exact procedure used, have not been investigated in detail in this study. Different estimates exist for the volume being averaged by the probe permeameter measurement. One investigation has arrived at 90% extent of averaging within a range of 4 times the probe aperture radius (Goggin *et al.* 1988). The derivation used a numerical model and assumed a homogeneous material. Another investigation found that 90% extent of averaging is within 2.2 times the aperture, by using Fourier spectral analysis of results on real materials (Jensen *et al.* 1994). Apertures normally used for probes are 5.9 mm or 3.6 mm (Corbett *et al.* 1992), but the probe dimensions are unknown for this specific study.

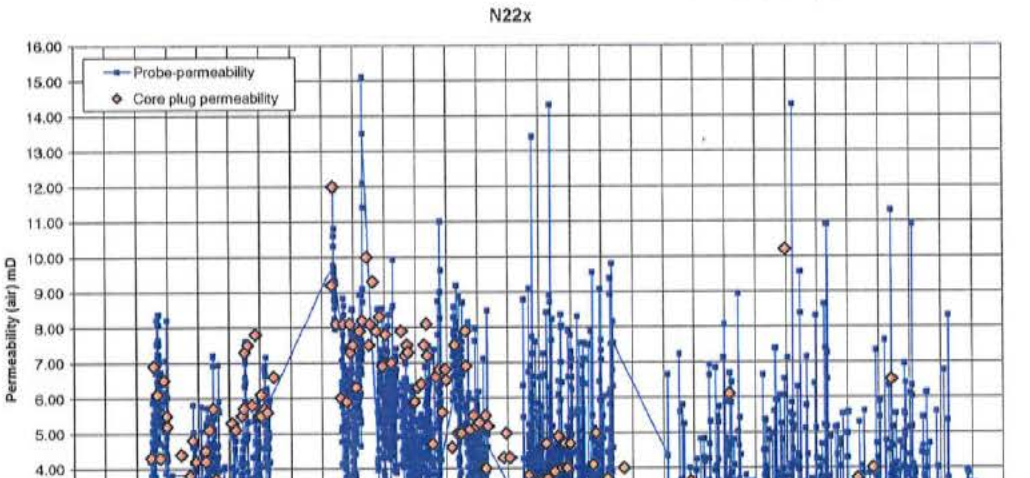

Figure 33

All probe permeability data from well N-22x compared with the conventional core analysis permeability data. Only probe data around 4 mD seem to match the general level of the larger-scale core plug data. This could indicate a calibration problem. The interval for core no. 6 (7196-7224 ft. MD) has been extracted for further analysis.

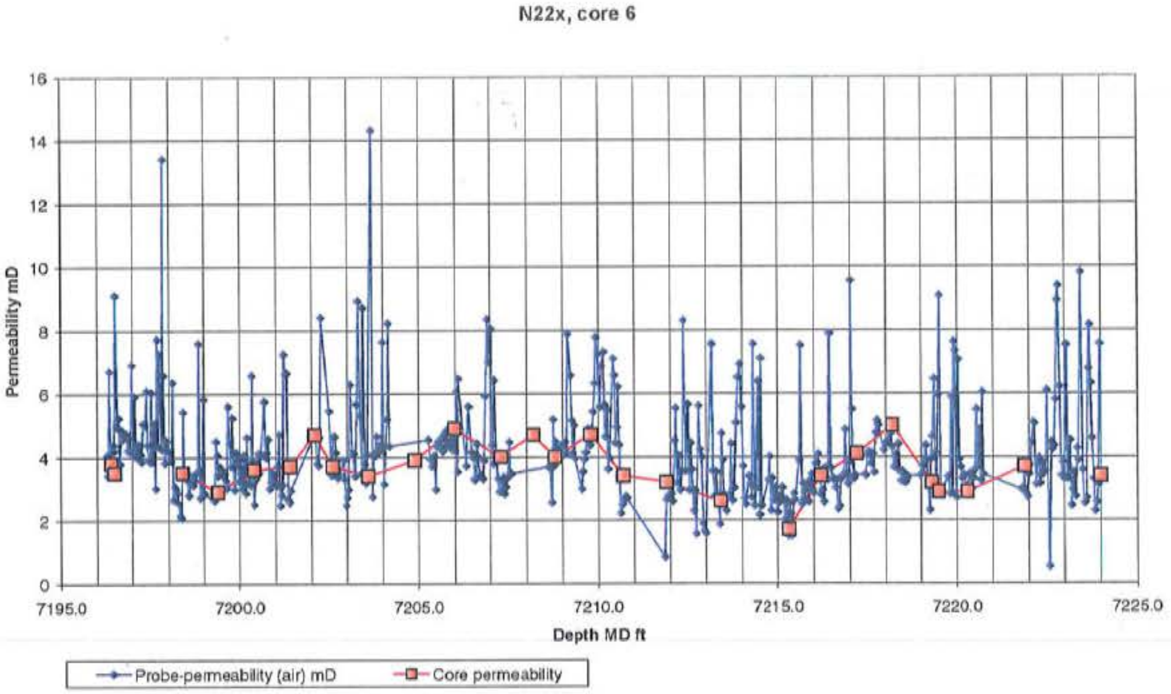

Figure 34
Comparison of probe permeability data and core analysis permeability data from core no. 6. Fair correspondence is seen.

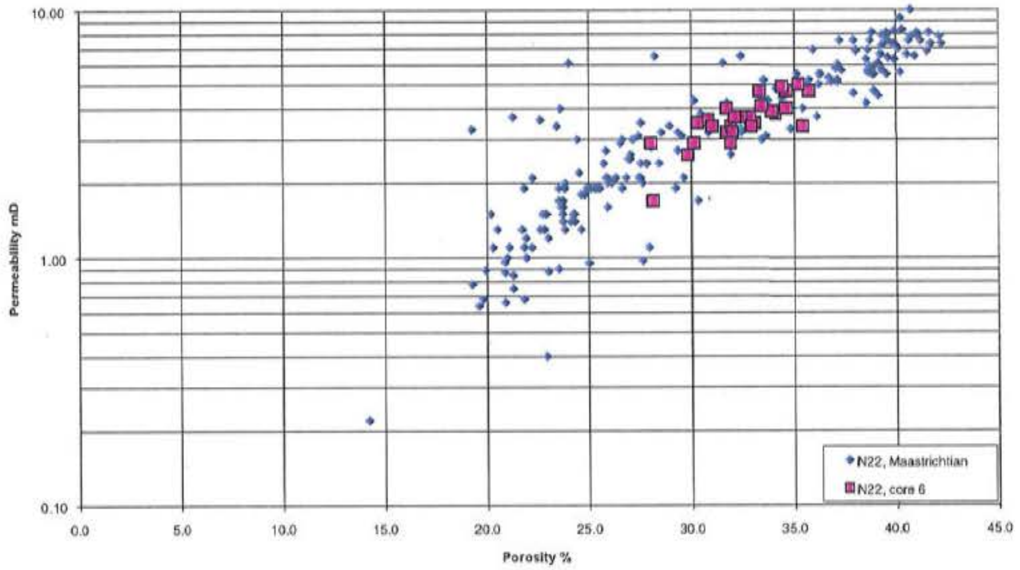

Figure 35
Comparison of porosity/permeability relation for the core no. 6 interval and the Upper Maastrichtian section in N-22x. The relation shows a well-defined trend and correlation with porosity with a variability of factor 2 for the high permeabilities.

For core no. 6, the permeability block-average has been calculated for intervals of 1 meter length (Fig. 36). The sequence has been divided into 1 m sections and the arithmetic, harmonic and geometric averages have been calculated as an average over each 1 meter section in the sequence. The anisotropy has been derived as the Arithmetic/Harmonic ratio, assuming that the chalk is a layered system.

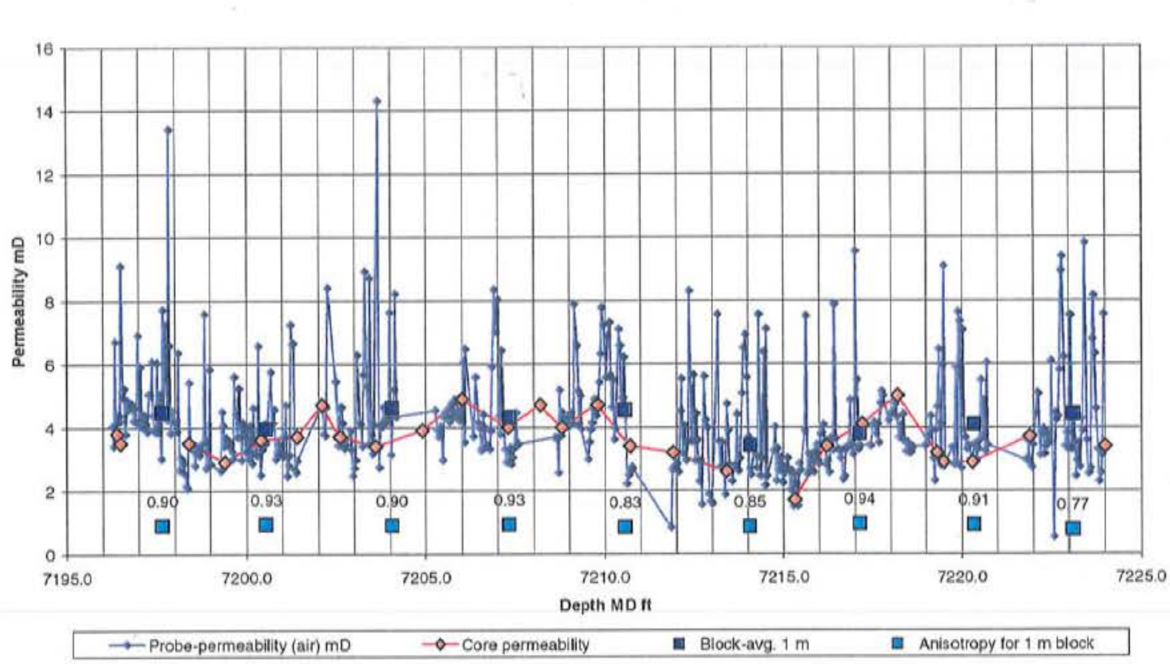

Figure 36
Comparison of 1 m block-averages to the data. The anisotropy has been calculated as the ratio of Arithmetic/Harmonic averages, assuming that the chalk is a layered system. For core 6 this anisotropy ranges from 0.77 to 0.94, depending on the permeability contrasts within the 1 m interval.

In order to analyse the anisotropy closer to the core-plug scale, the average for a 5 cm length measure has been calculated for parts of the core no. 6 interval. This volume of 5 cm length corresponds approximately to a volume of a 2 inch vertical plug. Again assuming a layered nature of the chalk at this small scale, the anisotropy is calculated and ranges from 0.46 to 1.00 (Figs 37, 38).

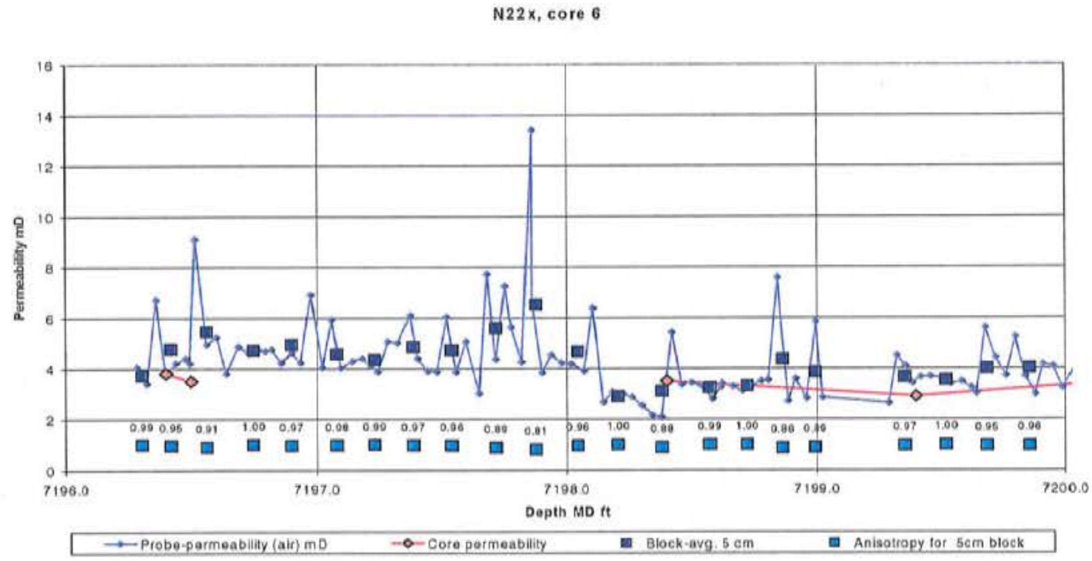

Figure 37
Section showing the 5 cm block averaging and the anisotropy ranging from 0.81 to 1.00.

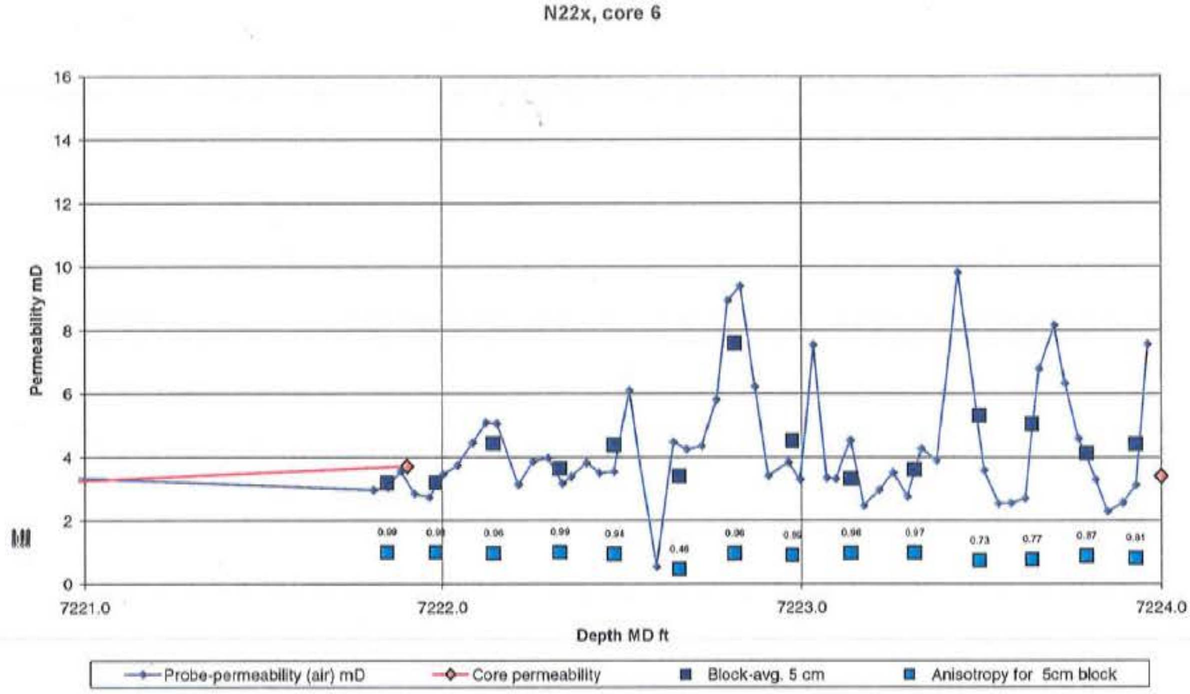

Figure 38
Section of a 1 meter interval showing the 5 cm block averaging and the anisotropy ranging from 0.46 to 0.99.

For the section in core 6, the distribution of permeability values and the anisotropy values for the 5 cm block scale is illustrated on Figs. 39, 40, 41, 42, 43, showing the very few outliers of high anisotropy. The main part of the anisotropy values is between 0.8 and 1.0 (Fig. 43).

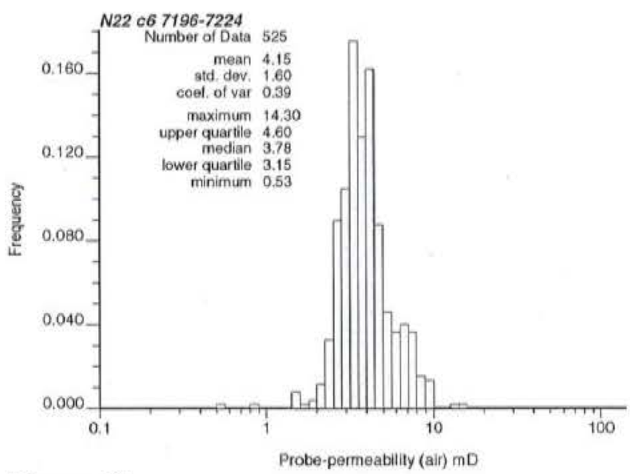

Figure 39
Histogram of probe permeability values from the core no. 6 interval.

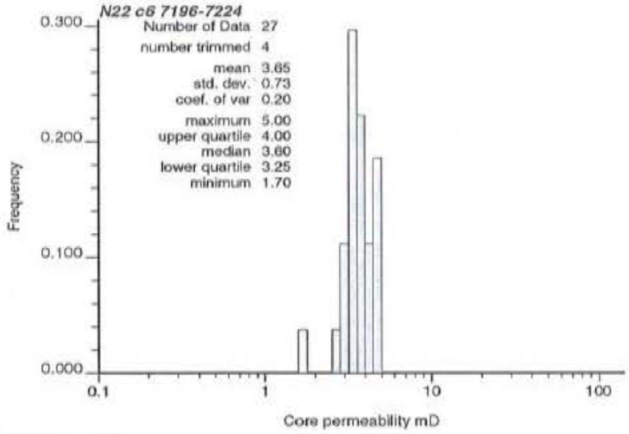

Figure 40
Histogram of core plug permeability values from the core no. 6 interval.

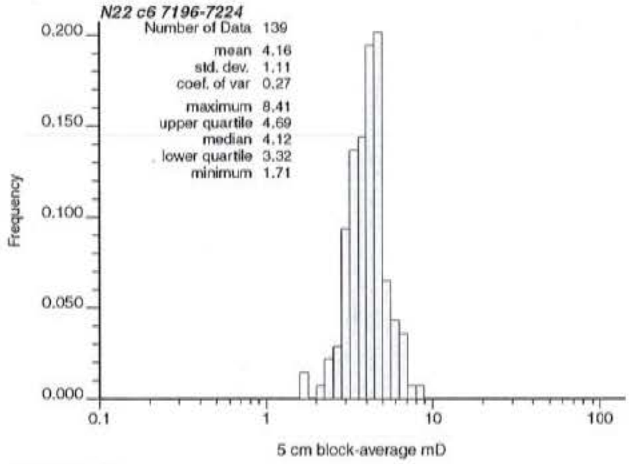

Figure 41
Histogram of 5 cm block-averaged probe permeability values from the core no. 6 interval.

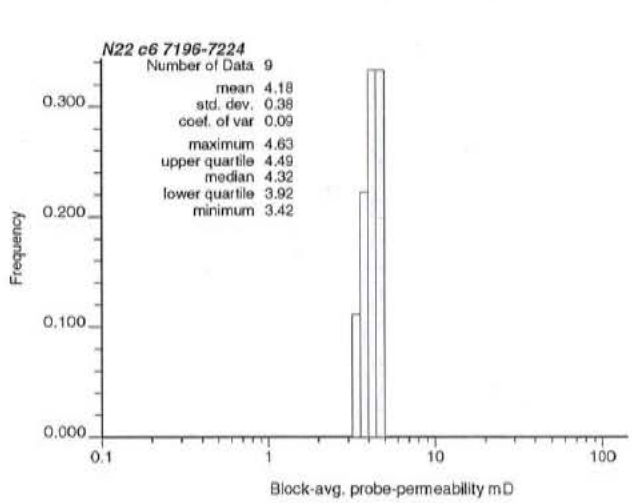

Figure 42
Histogram of 1 m block-averaged probe permeability values from the core no. 6 interval.

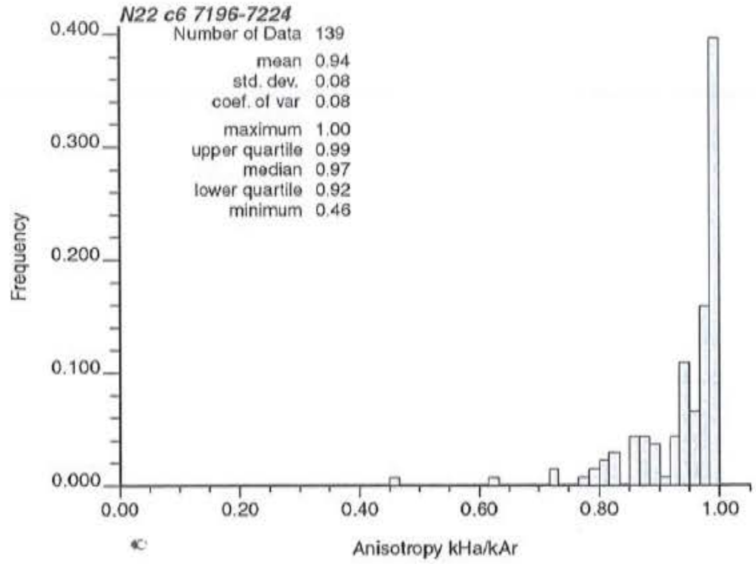

Figure 43
Histogram of the calculated anisotropy values for the 5 cm block average scale..

Estimation of average and sampling

The probe permeameter data is analysed for variability measures. In the 8 m interval of bedded chalk from core no. 6 in this analysis, the performance of core plugs is compared with the probe permeameter for the estimate of the mean permeability of the interval. For this purpose, the coefficient of variation $\hat{C}_V$ is calculated and used for determining the minimum sampling interval needed to correctly estimate the mean for the interval investigated (Jensen *et al.* 1997). Based on the core plugs, the coefficient of variation $\hat{C}_V = 0.20$, giving $I_0 = 4$ and $d_0 = 2$ meter, well above the customary 1 ft. sampling interval. Therefore, the mean value of permeability is correctly assessed. The probe data give $I_0 = 16$ and $d_0 = 0.5$ meter. For such variability, only about 16 probe measurements are needed for estimates of a valid average permeability within $\pm 20\%$ for the interval investigated.

However, the mean permeability of a sequence might be of limited interest in an upscaling issue, since we really want to express the fine-scale variability and analyse its effects on the flow properties from the upscaling study. For this purpose, the spatial variability and the spatial arrangement of the heterogeneities are the most important aspect to quantify. In order to investigate the spatial variability, the experimental variogram has been calculated for the probe permeability values (Fig. 44).

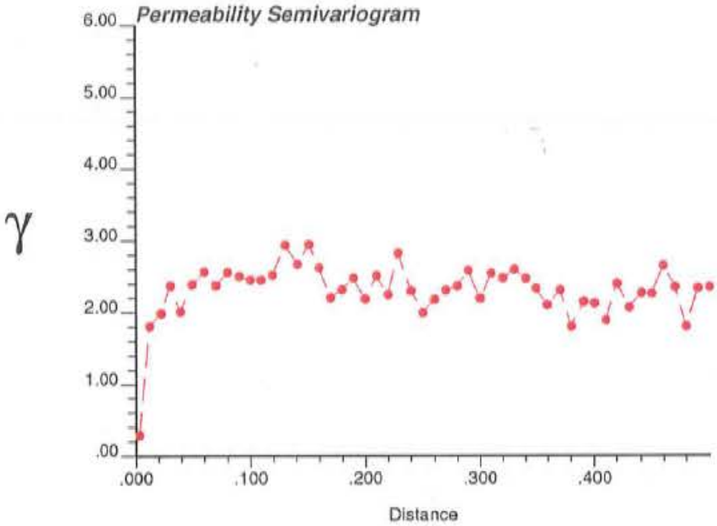

Figure 44

Experimental variogram for the probe permeability values from the core no. 6 interval. The variogram calculated shows a range around 0.06-0.08 m. This shows that in the investigated section, the amount of heterogeneity captured within a plug volume represents nearly 90% of the total variability in the probe permeameter data.

Conclusion

The very short correlation range (6-8 mm) shown by the probe permeameter data, indicates that a measurement for every 3-4 mm is needed to describe the variability at this very fine scale. The short correlation range also indicates that a standard core plug of 1-2 inch dimensions captures most of the small-scale permeability heterogeneity, and that the flow effect of the heterogeneity is correctly averaged during the core measurements of this particular plug.

The maximum anisotropy calculated from probe permeameter data by assuming perfect layering at plug-scale only rarely reaches a ratio of 1:2 for the k_V/k_H. This low ratio is only reached in very few intervals with markedly low permeability outliers, and thereby high contrast. Most anisotropy values for the 5 cm scale are between 0.80 and 1.0.

The I_0-sampling approach used on a single interval of 8 m indicates that a plug for every 2 m is sufficient to estimate the mean permeability within $\pm$20% of the parent mean for 95% of all possible samples. But the selected interval might have lower than usual heterogeneity reflected in the probe permeameter data set.

PERMEABILITY ANISOTROPY ANALYSED FROM CUBE-SAMPLES

Objective

The aim is to show the effects of small-scale (mm-cm) heterogeneities on the permeability anisotropy (k_V/k_H) in chalk volumes of a few cubic-cm (plug-size).

Cube analysis

In order to investigate different types of heterogeneities and their effect on directional flow, four cubes of 45 mm side-length have been cut from core material. After soxhlet cleaning the cubes have been mounted in soft rubber sleeves with a square inner and a round outer shape, and gas permeability has been measured for all three directions in the cubes by standard core analysis procedures (Table 1).

The cubes were subsequently cut into 8 sub-cubes, each being 2x2x2 cm. These 16 cubes for each sample were measured for directional permeability in all three directions with the same method as for the large cubes. The extracted samples and their characteristics are listed in Table 2.

Cube no. 2 with clay flasers disintegrated during cutting into minicubes, and could not give any data.

The remaining three cubes have yielded data.

Cube 1: Healed hairlines, MFB-7, core 2, 7395.5', D1 unit.

Cube 3: Clay flasers, MFA-11, core 4, 7758'7", D2b unit.

Cube 4: Lamination, MFB-7, core 5, 7570', M1 unit.

CUBE 1

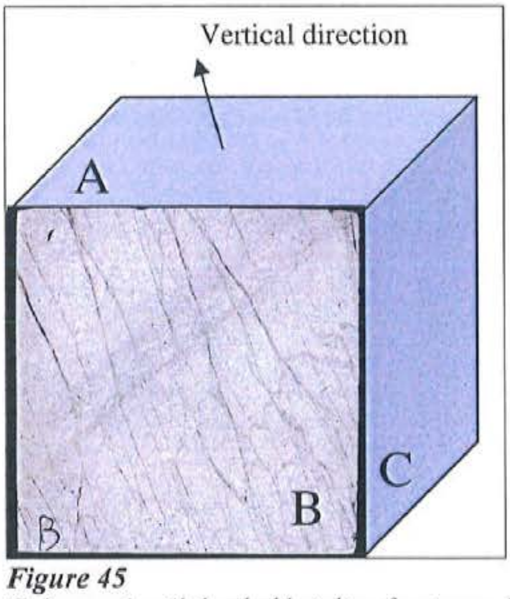

Figure 45

Cube no. 1 with healed hairline fractures. MFB-7, core 2, 7395.5', D1 unit

This cube is an attempt to analyse the effect of the healed hairline pattern. Unfortunately, the sample was not extracted exactly perpendicular to the features in the core, but the A direction is *along* the healed hairlines (vertical) although the pattern is complicated. A Zoophycos tracefossil is crossing over the sample in near-horizontal position.

CUBE 3

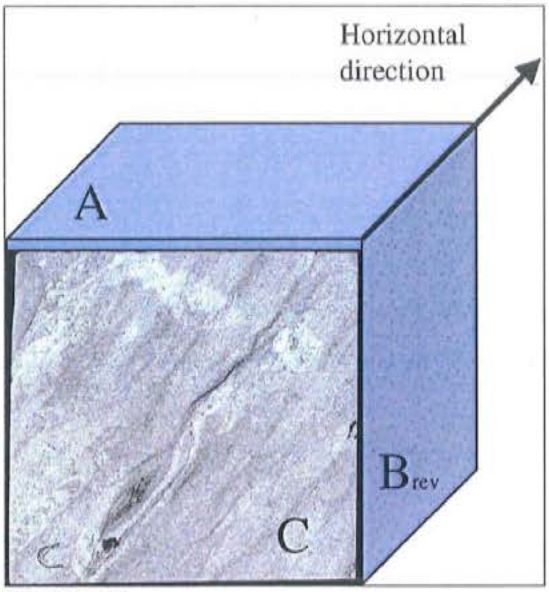

Figure 46
Cube 3 with clay flasers. MFA-11, core 4, 7758'7", D2b unit. The orientation of the cube is rotated around the horizontal axis, so the C measurement is the horizontal permeability, whereas A and B have an angle to the vertical.

This cube should analyse the effect of clay flasers. Unfortunately, the sample was not extracted perpendicular to the features in the core, but the C direction is *parallel* to the clay flasers although the pattern also here is complicated.

CUBE 4

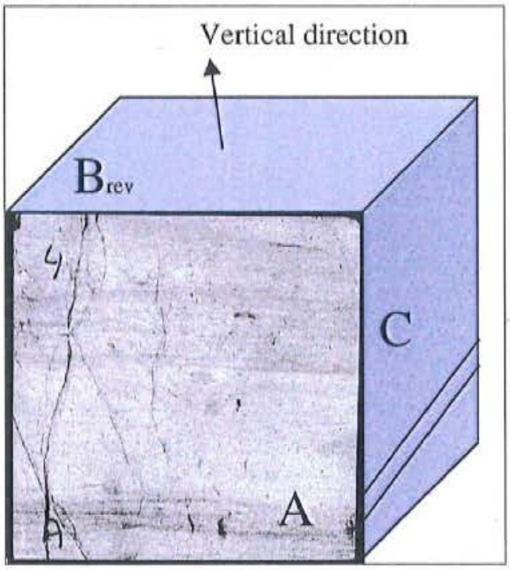

Figure 47
Cube 4 with lamination. MFB-7, core 5, 7570', M1 unit

This cube should analyse the effect of lamination. The sample was extracted close to perpendicular to the features in the core, and the B direction is *perpendicular* to the lamination. The sample contains a few healed hairline fractures, that could complicate the measurements slightly.

Mini-cubes

Each cube was cut into 8 sub-cubes, and the porosity and directional permeability was measured on each cube (Table 1), and the data are shown on figures with the porosity/permeability relation (Figs. 48, 50, 52) and histograms of the k_V/k_H on Figs. 49, 51, 53.

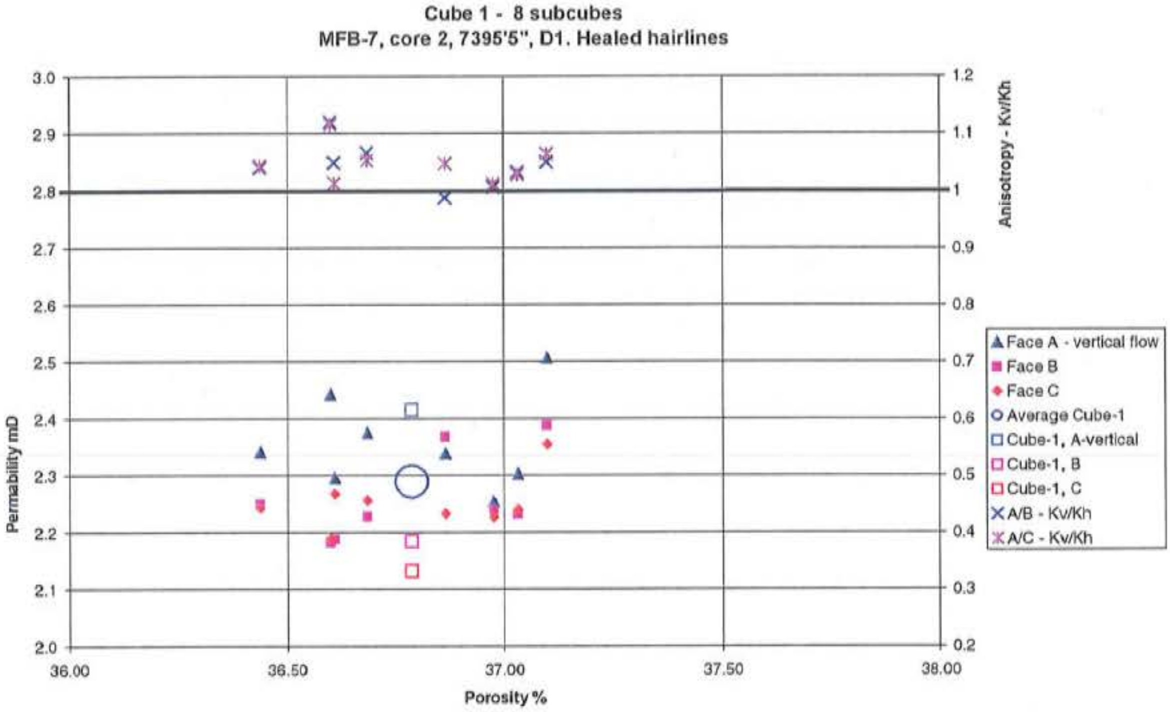

Figure 48

Porosity/Permeability plot of the measurements of minicube data, cube 1. For comparison the average porosity and directional permeability data for the large cube are also shown on the diagram. All anisotropy values lie above 1 due to the vertically aligned healed hairline fractures.

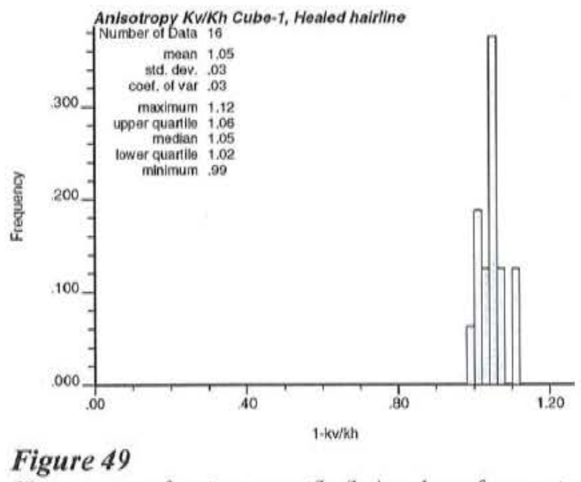

Figure 49

Histogram of anisotropy (k_V/k_H) values from minicubes for cube no. 1 with healed hairline fractures.

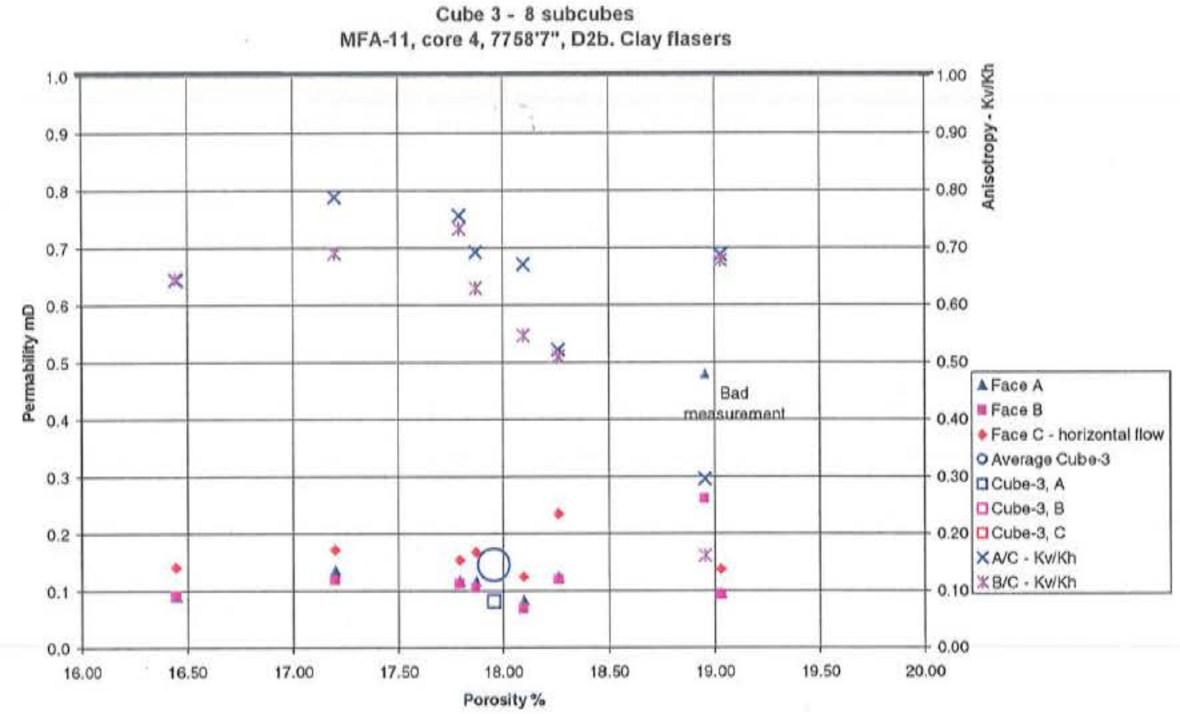

Figure 50
Porosity/Permeability plot of the measurements of minicube data, cube 3. All anisotropy values lie significantly below 1 due to the horizontally aligned clay seams. The permeability measurement of the intact large cube has given reliable results only for one direction which is the only value shown on the plot.

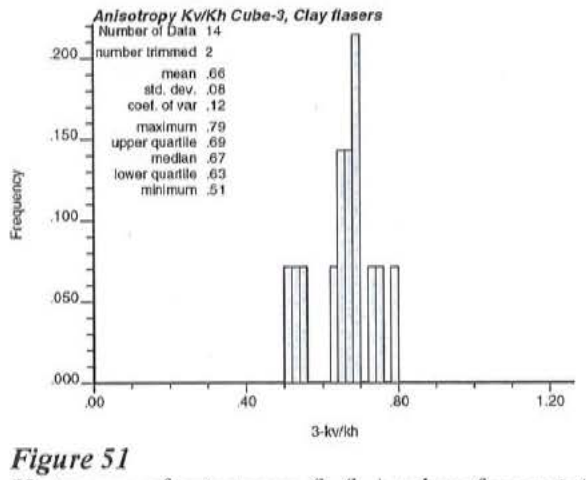

Figure 51
Histogram of anisotropy (k_V/k_H) values from minicubes for cube 3 with clay seams.

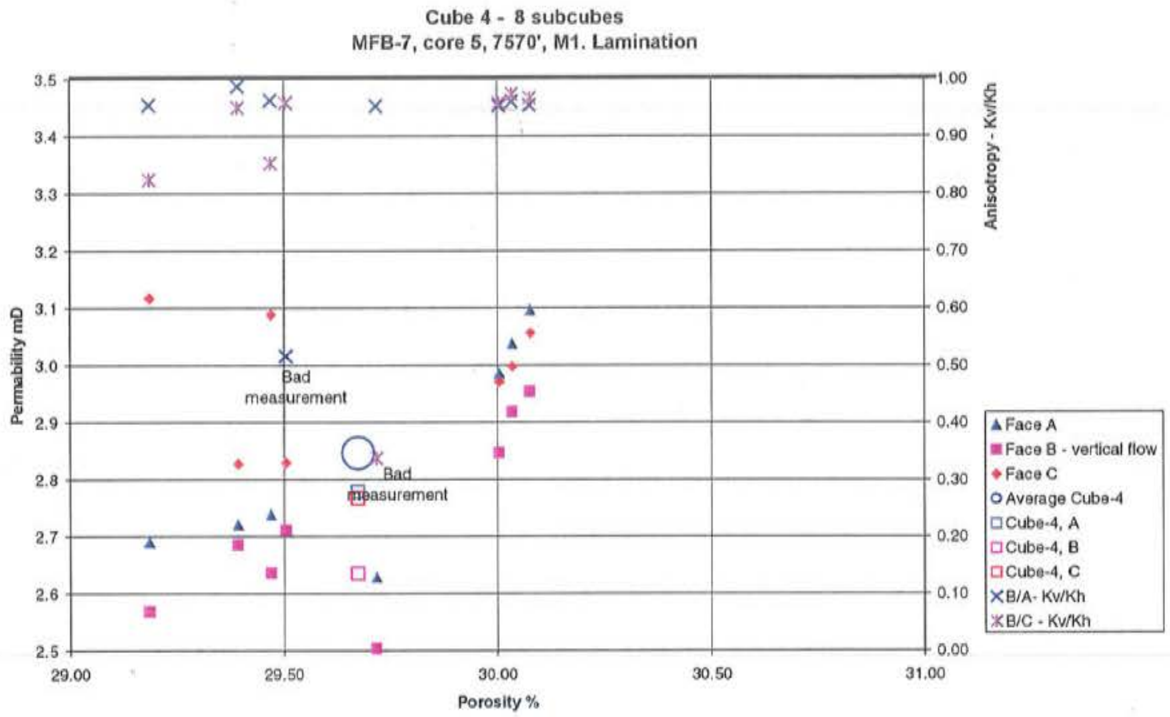

Figure 52
Porosity/Permeability plot of the measurements of minicube data, cube 4. For comparison the permeability data for the large cube are shown. All anisotropy values lie below 1 due to the horizontally aligned lamination.

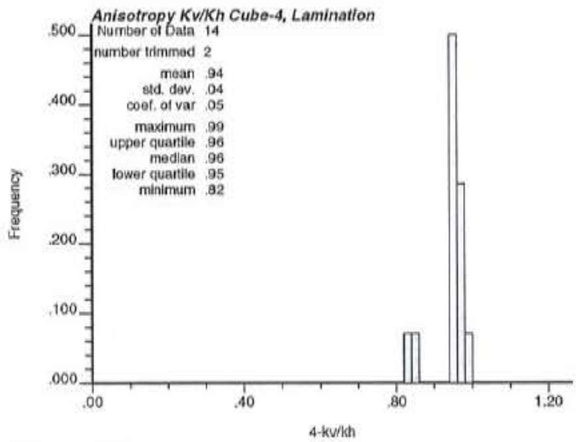

Figure 53
Histogram of anisotropy (k_V/k_H) values from minicubes for cube 4 with lamination.

Interpretation

The effect of small-scale heterogeneities seems to be detected for all the three different types analysed. The effect is detected within a volume of 8 cm^3 (2x2x2 cm) which is a volume fairly close to the volume of a standard plug. The anisotropy values derived in this analysis are therefore considered valid for the plug-scale level of sample size, and can be used for input to modelling if input cells have plug size.

An effect from the very subtle features of **healed hairline fractures** have been consistently detected as an anisotropy above 1.0 (except for one single sample with 0.99 k_V/k_H), and the mean k_V/k_H arrives at 1.05 ranging up to 1.12.

For the heterogeneity of **clay flasers**, a more dramatic effect is seen, ranging from 0.51 to 0.79, with a mean of 0.66.

For another subtle feature like **lamination**, the k_V/k_H ranges from 0.82 to 0.99 with a mean at 0.94.

Although the material is limited, the measurements have given very consistent indications on the parameters we were looking for. The shown distributions can therefore be utilised for modelling of variable k_V/k_H, or a mean value be assumed, with the endpoints available for sensitivity studies.

VARIABILITY OF POROSITY ANALYSED FROM FINE-SCALE CORE DENSITY SCANNING

Scanning procedure

The obtained core from the Tor Formation has arrived in approximately 1 meter sections in boxes approximately 10 days after the drilling operation. It has been surface-cleaned for drilling mud and placed in a plastic sock (but not welded at the ends), and these 1 m segments have been placed in boxes.
Two weeks after the cleaning procedure started, the density scanning was initiated and the core segments have been placed on a conveying belt transporter and scanned for bulk-density and gamma ray activity. It was assured that the bedding was oriented vertically and parallel with the scanning beam in order to get the best resolution of the density variations. The extraction of the preserved sample set was carried out after the scanning procedure, and the core was therefore in an optimal state during the scanning.
The scanning speed was set to 1 cm pr. minute. For every 1.0 cm a reading of the bulk-density was calculated as a conversion from the accumulated signal from the gammaray-source during the time window of 1 minute, reaching the detector after passing through the core (Fig.54). The bulk-density data has been derived assuming a constant core diameter, and also relies on a calibration procedure using reference material.

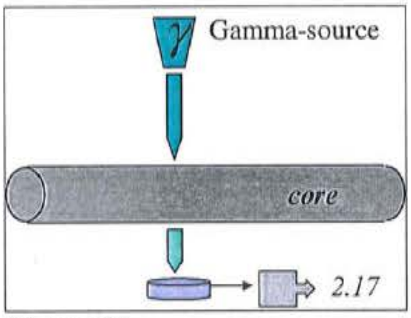

Figure 54
Schematic illustration of the scanning set-up for a core.

The collimator window opening is 9 mm for the density scanning tool. Due to the small time interval used for the capture of the density, and the well defined collimator window, the filter-function (response curve) is considered to be a near-triangular function with a width of 18 mm, giving an overlap of ca. 25% for the successive readings. The resolution is defined as 18 mm, since this is the minimum thickness of a layer in order to be represented by its true value for a particular reading.
The raw bulk-density data has point values for each 1.0 cm (Fig. 55).
Due to the effect from fractures and the separation between the core segments, the resulting erroneous and artificially low densities have been edited away for the detailed analysis. Further editing is necessary of the data to obtain a more reliable estimate for the true density distribution. The influence from the top and bottom of the core segments is checked as seen on Figure 55.

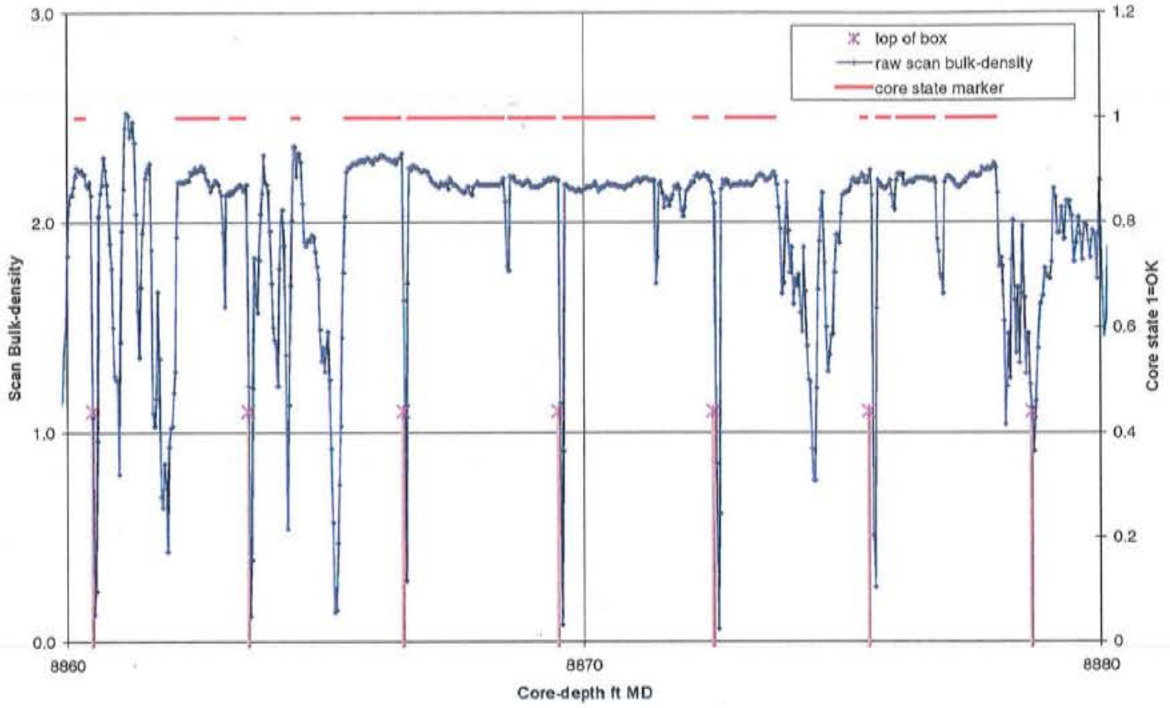

Figure 55
Plot of the raw bulk-density data calculated during the scanning procedure. All the very low density points are due to separation between core pieces or fractured or crumbled core material. Most of the very low peaks are associated with the separation between the individual boxes. The editing of the bulk-density data is based on a core description recording the state of the core material regarding fractures or irregularities that can influence the density recording. The core state marker is used for sorting the data.

Conversion from density to porosity

The calculation of porosity from the bulk-density data assumes that the core has a constant diameter, that mud-invasion is limited and evaporation is negligible, and that the grain-density is constant. For the conversion is assumed that the matrix material is pure calcite (density 2.71) and the porosity has been calculated by the simple formula

$$\textit{Porosity} = \frac{2.71 - \textit{scanbulkdensity}}{\textit{pore(fluid)density}}$$

The major uncertainty is the fluid density, since both variable fluid composition through the core, and variable evaporation effects can have modified the pore fluid density at the scanning time. Therefore a matching procedure has been used by comparing to the available core analysis data from plug material. By this procedure a fair match is obtained using a pore fluid density of 1.85.

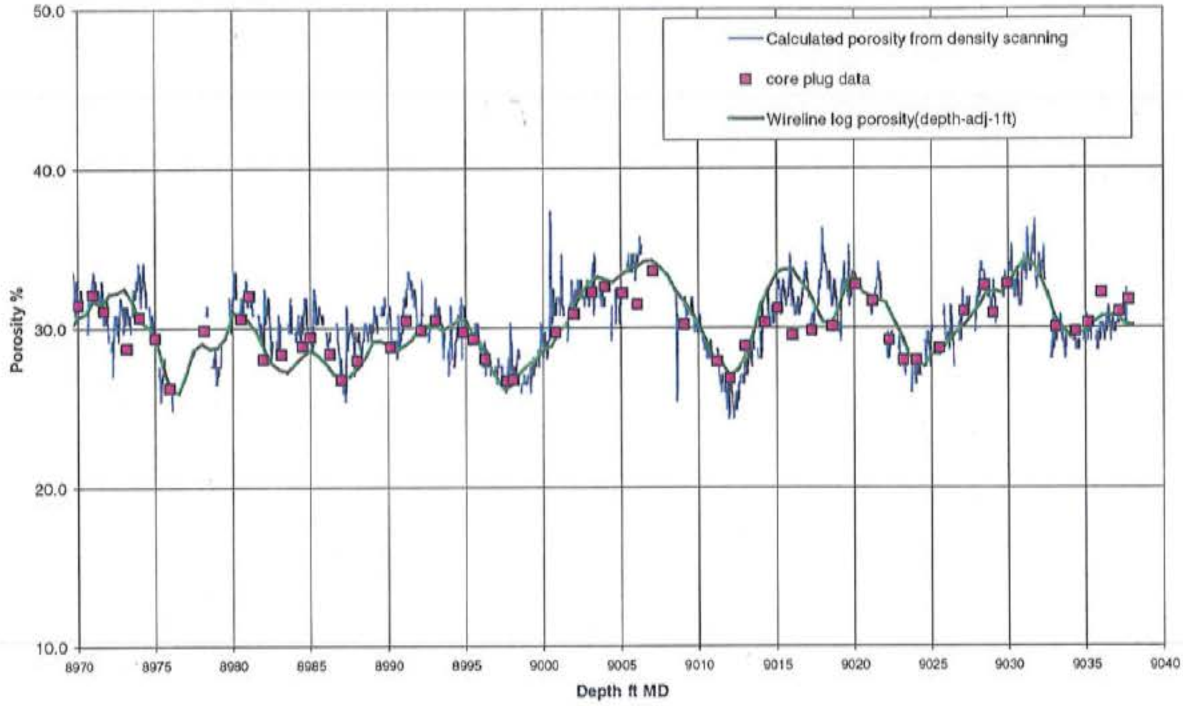

Figure 56
Comparison of the calculated porosity from the fine-scale bulk-density data by using a fluid density of 1.85, and the core analysis data from plug material. The porosity calculated from the wireline well log data is also shown. The depth measure is in MD from the core material, and does not show the true thicknesses due to the deviation of the well which reaches more than 60 degrees in this interval.

The core material spans a total of 56.6 meters, and from this a 20 m log section has been selected (Fig. 56) for the detailed analysis presented here to show the principle in the treatment of the data.

Comparison of the porosity histograms from the different sources (Figs. 57, 58, 59) shows only small differences in the porosity distribution, and the crossplot between core plug porosity and density calculated porosity is fair (Fig. 60).

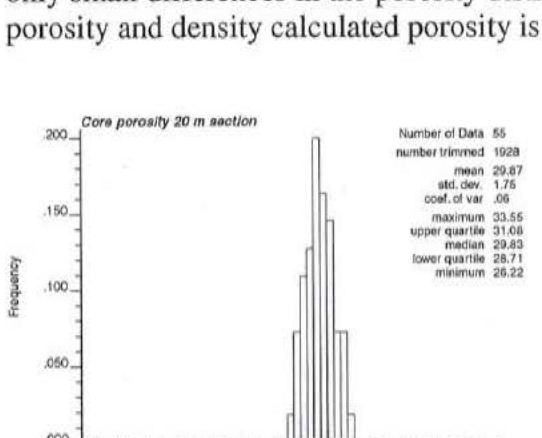

Figure 57
Histogram of core plug porosity from the 20 m section analysed in the well.

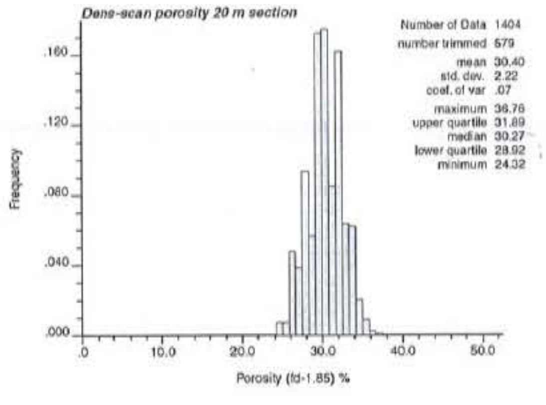

Figure 58
Histogram of porosity values calculated from the scanned bulk-densities in the same section.

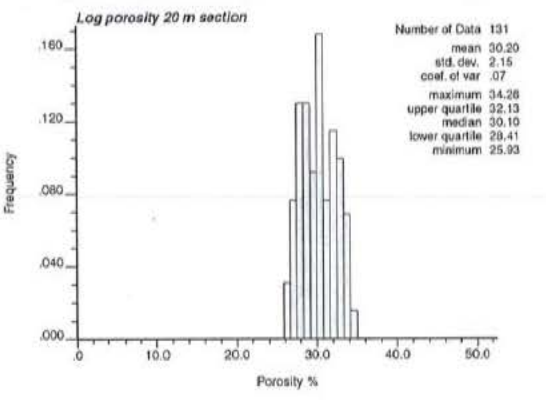

Figure 59
Histogram of the well log interpreted porosity values from the same interval.

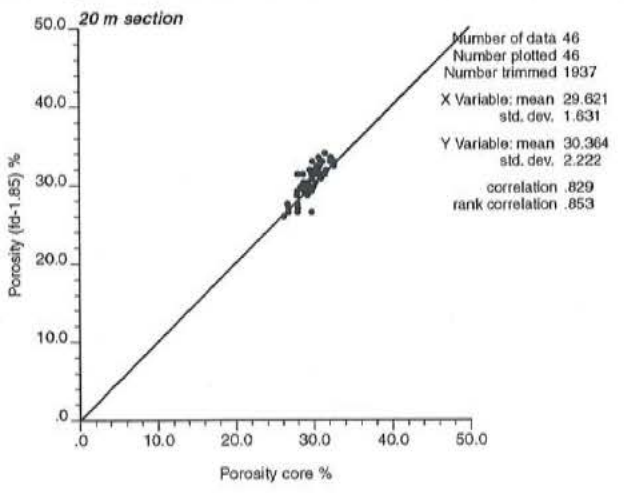

Figure 60
Crossplot of standard core plug analyses porosity and bulk-density calculated porosity showing a good correlation.

The porosity/permeability relation for the core plug material is well behaving (Fig. 61), and comparable to existing trends for Maastrichtian core material.

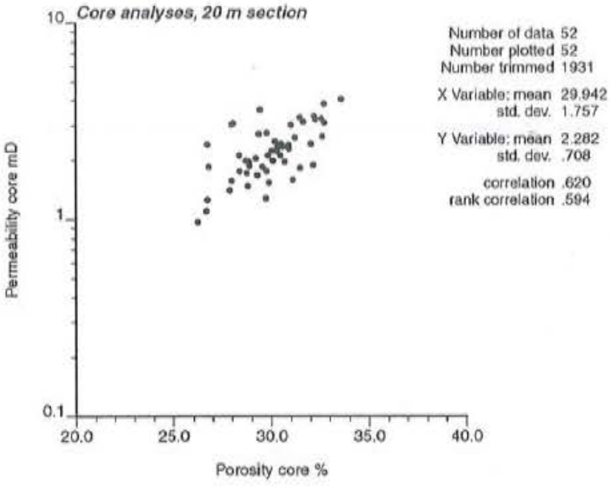

Figure 61
Porosity/permeability relation for the core analysis material. The trend is comparable to the normal tend relation for Maastrichtian chalk.

Spatial variability

In order to analyse the spatial variability, the variogram is calculated for the three different porosity data types in the 20 m section (Fig. 62). The variogram describes the variance for the two-point statistics of the data as a function of the separation between the compared data points. The variogram can show if there is any consistent spatial correlation in the data or if there are any signs of periodicity.
The variogram for the fine-scale density data is modelled with a small nugget and two structures. The nugget of 0.60 is probably signifying that a very small scale variability is present in the material or alternatively the nugget can be assigned to noise. A spherical structure with 0.35 m range describes the initial part of the variance, and an additional hole effect with an amplitude of 1.80 m describes the periodic signal seen to be in the porosity fluctuations. The same periodicity is preserved also in the core analysis data and the log porosity data. The distance measure for the variogram is in true vertical depth (TVD) meter values, which is a caution to be taken because of the deviated well.

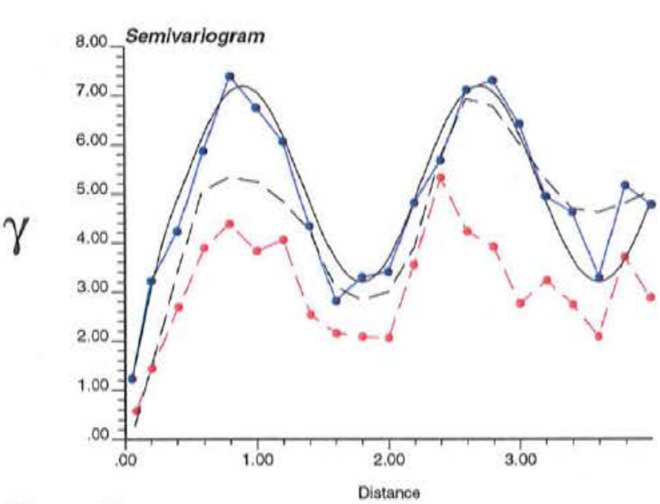

Figure 62
Experimental and model variograms. The distance is in meters true thickness, and the γ value is the variance for that specific lag distance. The experimental variogram for the fine-scale porosity data converted from the bulk-density data is shown in blue line with dots, the core analysis porosity data (red stippled with dots), the log porosity data (stippled black), and the variogram model for the fine-scale data (black line).

In order to describe the spatial structure of the data, a variogram model is fitted for the cm-scale porosity calculated from bulk-density data:

Nugget effect: 0.6

Two structures:

1. *Spherical structure with sill 2.6 and vertical range 0.35 m*
2. *Hole effect structure with variance contribution 2.0 and peak distance at 0.90 m (=wavelength 1.8 m).*

Discussion

On Figure 62 it is seen that the variance of the wireline log data is slightly higher than that of the core plug data. This is unexpected since the log data is a filtered version of the finer scale values. From this it seems that the extraction of the plug material has not succeeded in recording the intervals with extreme values, which only is expressed in the fine-scale core scanning data, and partly recorded by the log data. This is also illustrated on Fig. 56 where the log data shows a filtered version of the fine-scale porosity variations recorded by the density scanning. The pattern seen where the fine-scale porosity deviates 3-4 p.u. from the log curve, is a pattern that is aimed for in the simulation exercises where the fine-scale porosity is generated from knowing only the structure of the log data from the well.

Conclusion

The investigation shows that these detailed data recording the porosity variations in the chalk core can be used to asses the short range correlation structures at a very fine scale not hitherto investigated in this material.

The extracted plug material has not succeeded in reflecting the full variation in the porosity. Until further analysis is done to support an explanation, this is considered due to the selective extraction of plugs, avoiding intervals with weak material.

The variograms strongly suggest cyclicity expected in the porosity signal in the sequence. The histograms and variogram analysis illustrate the change in correlation structure, especially the variance, as a function of the change of support volume from 1.8 cm scale of the scanning density to approximately 2-2.5 cm scale for the core analyses.

References

Corbett, P.W.M., S., R.P., L., J.J. & Sorbie, K.S. 1992: Laminated clastic reservoirs: The interplay of capillary pressure and sedimentary architecture. SPE 67th Annual Technical Conference, Washington DC, 4-7 October 1992. SPE Paper **24699**, .

Goggin, D.J., Chandler, M.A., Kocurek, G. & Lake, L.W. 1988: Patterns of permeability in eolian deposits; Page Sandstone (Jurassic), northeastern Arizona. SPE Formation Evaluation **3**(2), 297-306.

Jensen, J.L., Glasbey, C.A. & Corbett, P.W.M. 1994: On the interaction of geology, measurement, and statistical analysis of small-scale permeability measurements. Terra Nova **6**(4), 397-403.

Jensen, J.L., Lake, L.W., Corbett, P.W.M. & Goggin, D.J. 1997: Statistics for petroleum engineers and geoscientists, 390 pp.: Prentice Hall.

Fine-scale models and upscaling studies

Peter Frykman

CHARACTERISATION AND MULTISTEP UPSCALING OF FRACTURED CHALK RESERVOIRS.

JCR Phase V, Project no. 3

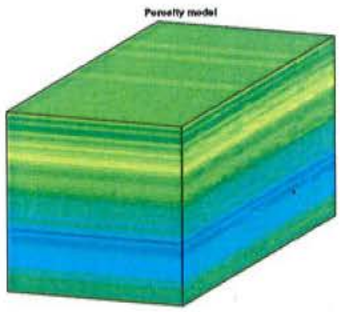

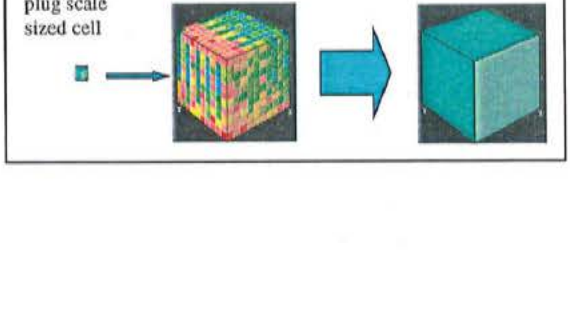

FINE-SCALE MATRIX GEOMODELS FOR UPSCALING

Abstract
This report describes how fine-scale geostatistical models are constructed to include data from reservoir characterisation at their correct scale. Information from both the available core plug data and from the wireline log interpretation is included in the modelling. The fine-scale geostatistic reservoir models of matrix properties can be utilised for investigating the upscaling of single-phase and two-phase flow properties. The study shows that the permeability anisotropy reaches 0.73 ($=k_V/k_H$) for a selected 20 m section of reservoir chalk. This anisotropy is caused solely by the meter-scale porosity variations and layered nature of the sequence, and the anisotropy will be further enhanced if any additional anisotropy at core plug scale is included in the study.

Introduction
Chalk reservoir rocks contain many types of small-scale heterogeneities from mm to cm. Although they are often subtle and difficult to discern, they have significant consequences for the flow of fluids. The single-phase flow is depending on the pattern of heterogeneities and the contrasts in the models, and in particular two-phase flow is influenced, since low-permeable chalk has high capillary forces and imbibition processes are important during production.
Since Scholle entitled his paper "Oil from Chalks, a modern miracle" (Scholle 1977), the miracle has not lost its power. Chalk reservoirs are peculiar in that they are high-porosity, low-permeability reservoirs of very fine-grained limestone with pore-throats around 0.1 - 1 micron (Fig. 62).

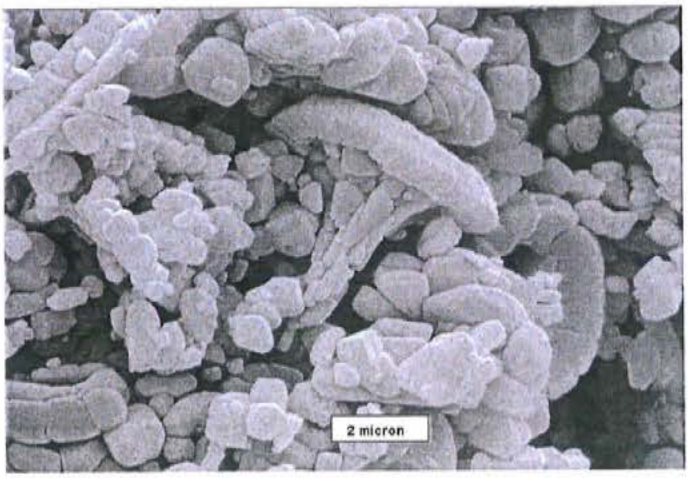

Figure 62
SEM image of outcrop chalk from the Sigerslev quarry in the Stevns area showing a typical Upper Maastrichtian chalk with 48 % porosity and 7 mD air permeability.

The high capillary forces combined with wettability of a slightly water-wet nature give rise to high imbibition potential in the rock. Accordingly, massive water-injection plans are seen to enhance productivity considerably, although in some cases they are aided by other factors than imbibition alone. Over the last few years (1992-1996) the estimate for average recovery factor for chalk fields undergoing water-injection has risen from 16% to 35% (DEA 1993; DEA 1997).This overall improvement in production is ascribed to a combination of horizontal wells, hydraulic fracturing and massive water injection (Fine *et al.* 1993; Nederveen & Damm 1993; Ovens *et al.* 1998).

As a precursor to evaluating the behaviour during two-phase flow, it is found necessary to develop an upscaling strategy and investigate the upscaling behaviour of single-phase flow. For this purpose, models incorporating the most detailed geological information is needed. One of the challenges is that the geological and petrophysical information is obtained from very different scales, i.e. measurements of volumes of different sizes e.g. the core plug volume versus the volume detected during wireline logging with a density log for the porosity estimation. Therefore the modelling procedure has to account for the disparate scales and their data contribution.
Some of the small-scale heterogeneities (mm- to cm-scale) in the matrix are investigated during core analysis of samples extracted from chalk core. Their combined effects are subsequently incorporated in the plug-measured properties. Heterogeneities larger than the sample size and combinations of different types of heterogeneities at scales larger than the cm-scale are not represented by any measured properties. As a consequence, the laboratory-measured properties are not suitable for the reservoir engineer who needs to input permeability and anisotropy values for simulator blocks at a scale of 10-100 m. This is a classic problem in upscaling procedures.
In this report, the problem is approached by starting at fine scale, using the plug-measured properties as input at their correct volume scale in a flow simulator. The simulation is designed to derive the effective permeabilities and in that the expression of the combined effects of the heterogeneities at the larger scale (Fig. 63).

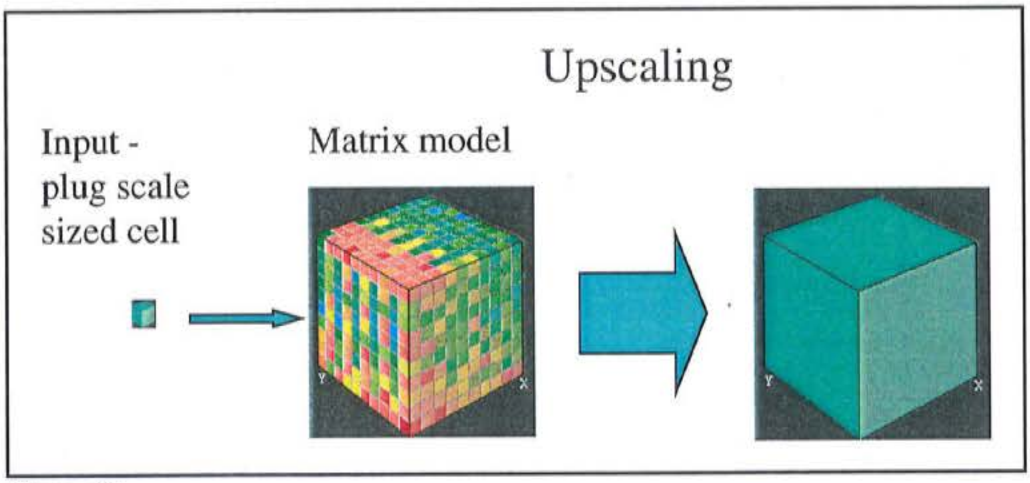

Figure 63
Schematic illustration of the upscaling from a fine-scale heterogeneous model with input data at plug scale.

This report describes how geostatistical models of matrix properties are constructed to include data from reservoir characterisation at their correct scale. The cubicmeter-size of the geomodel used in the first step of upscaling is sufficiently large to include characteristic layering aspects of the formation. Much of the reservoir section in the North Sea chalk reservoirs is considered to have a cyclic development of the porosity layering, with a layer thickness in the meter range. Variations of 5-8 percentage points between the low- and high-porosity layers are common, which corresponds to at least a factor of 2 for the permeability contrasts. Core-plug measured data of porosity and permeability, are used for the plug size cells in the geomodel. The small size of the individual simulation cell (5x2x2 cm) is chosen in order to allow the direct representation of core plug-measured parameters at centimetre scale. Subsequent reservoir flow simulation can be used to derive the upscaled properties for the full geomodel. The derived upscaled parameters are applicable as input for the next step of upscaling at a larger scale level, eventually leading up to full field reservoir simulation studies.

Geological background for model

The fine scale model used as an example for the upscaling procedure is based on a section of relatively non-fractured chalk from the MFB-7 well in the Dan Field in the Danish North Sea. The Dan field has been described in detail (Jørgensen 1993; Kristensen *et al.* 1995). Present production is currently taking place mainly in the uppermost Maastrichtian chalk section just below the top Maastrichtian hardground which separates the main reservoir section from the low permeable Lower Danian section (Fig. 64).

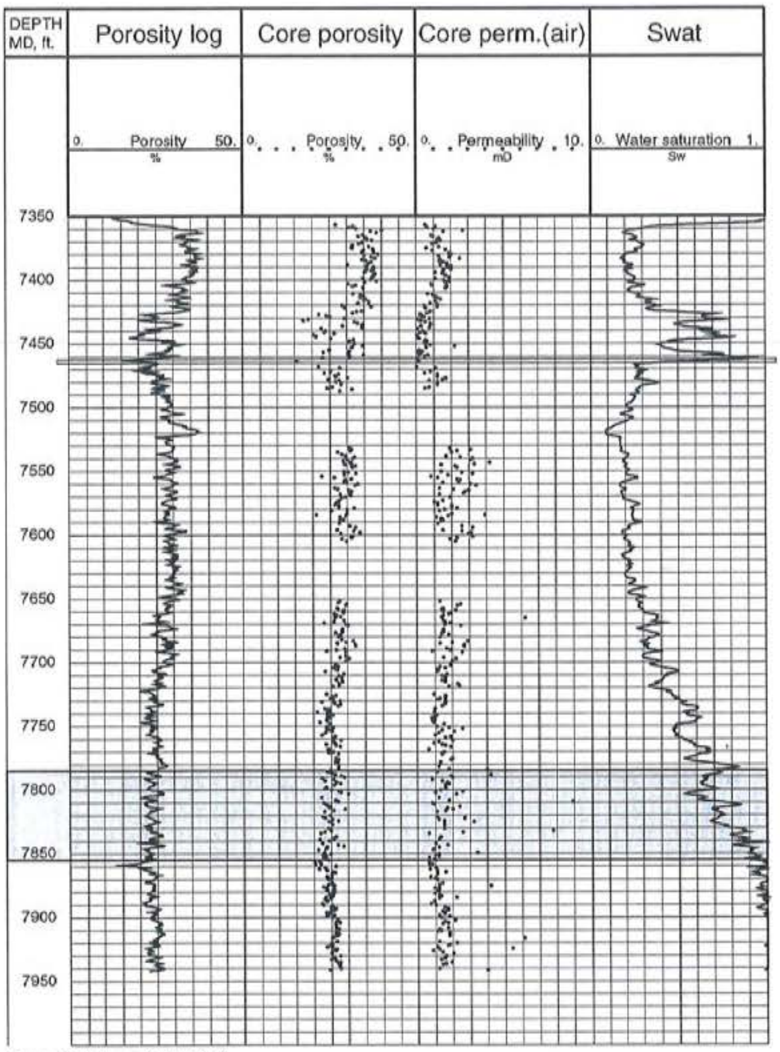

Dan Field, well MFB-7

Figure 64

Section in the MFB-7 well on the Dan Field showing wireline log porosity as well as core porosity and permeability and the log interpreted water saturation. The Maastrichtian/Danian boundary is marked at 7464 ft., and the selected section of ca. 20 m used in the upscaling study is marked in the lower part of the well section.

This reservoir section has a limited oil zone and a long transition zone caused by the high capillary forces in the low-permeable chalk. The porosity as seen from the wireline log interpretation and the core data varies from 20 to 35 % throughout the Upper Maastrichtian section (Fig. 65). An interval in the lower part of the transition zone has been selected for the analysis (Fig. 65).

The selected interval has a range for the porosity from 20 to 30 % (Figs 65, 66, 67). Similarly, the permeability variation is from 0.6 to 9 mD for the selected section (Fig. 68). However, the two high permeability values seen on the histogram are considered to be erroneous measurements due to damaged plug material, and have been excluded for the following analysis and for the simulation. The ranges are also illustrated on a porosity-permeability relation plot and compared to a larger data set from the same stratigraphic interval in the Dan Field (Fig. 69).

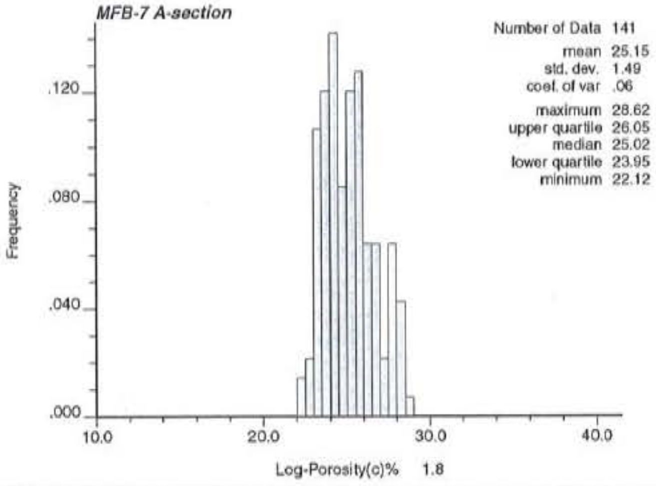

Figure 65.
Log interpreted porosity histogram.

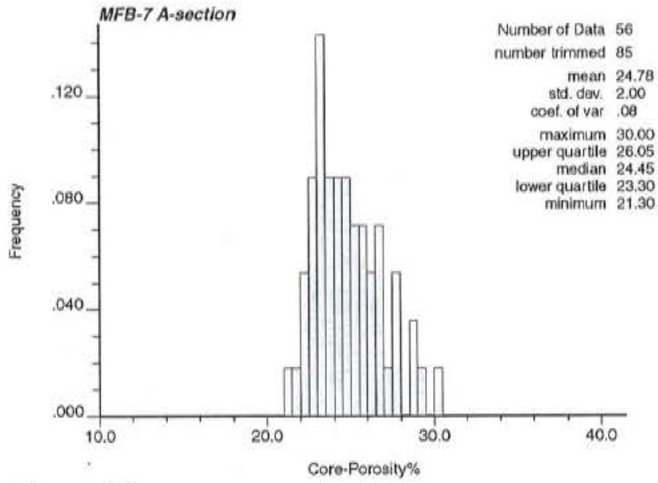

Figure 66.
Core plug porosity histogram.

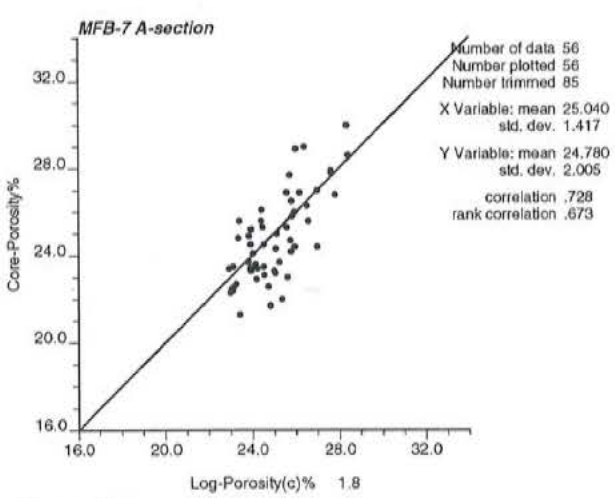

Figure 67.
Comparison of log and core obtained porosity values.

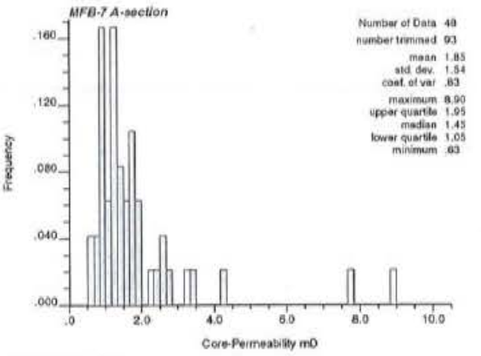

Figure 68.
The range of permeability values for the selected section. The two outlier points around 7 and 9 mD are excluded from the further analysis based on the interpretation as being erroneous measurements. This reduces the std.dev. to 0.75 and the mean to 1.57.

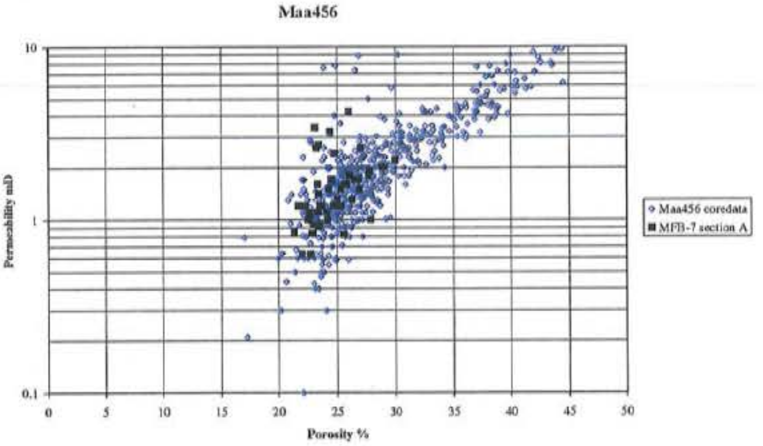

Figure 69.
Comparison of the porosity-permeability data from the selected section and a larger data set from the same stratigraphic interval in the Dan Field.

For evaluating the representativity of this section, the data is compared to a range of data assembled from North Sea chalk reservoirs and different outcrops in chalk (Fig. 70). The porosity and permeability distributions within the selected interval clearly shows a layered or cyclic variation in both data types, also illustrated by the log and core porosity (Fig. 71).

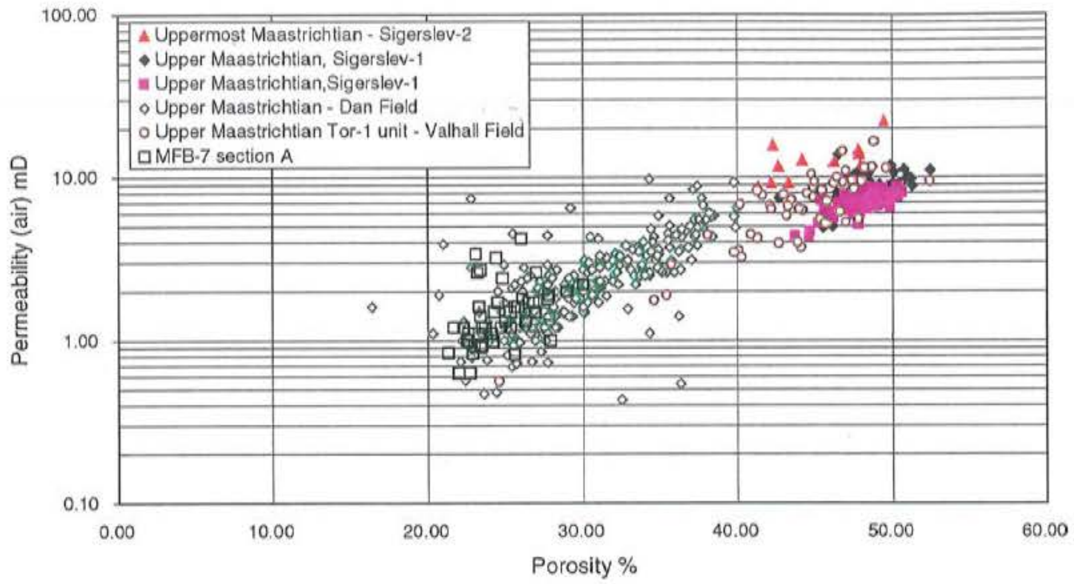

Figure 70.
Comparison of porosity-permeability data from the selected section in the MFB-7 well (section A), outcrop material from Stevns (Sigerslev), and the Tor Formation on the Valhall field in the Norwegian North Sea. All these data are considered to behave as one single Upper Maastrichtian trend for the porosity-permeability relation.

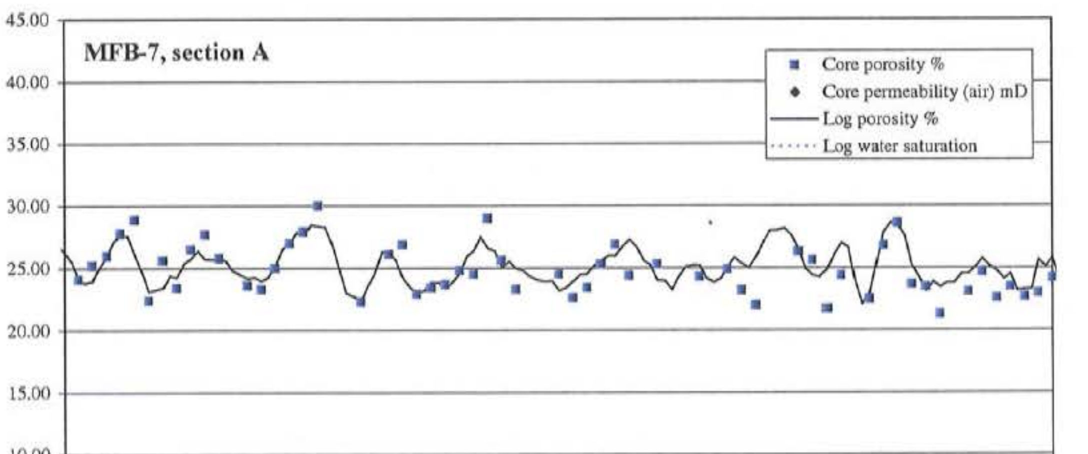

Figure 71
The section from the lower part of the MFB-7 well. The section from 7785-7855 ft MD is equalling 18 m true thickness. The two high permeability values at depth 7808.00 and 7831.00 ft. MD are the excluded data values.

The layering and the nature of the porosity variations in the reservoir chalk can partly be examined by a variogram analysis of the porosity data, which will give an indication on the wavelengths of the porosity variations (Fig. 72). The most clear indication of cyclicity is seen in the core porosity showing a wavelength of ca. 2.0 m. This pattern is also supported by the analysis of the log porosity data.

This cyclic concept for parts of the chalk section is supported by both other works on reservoir examples as well as outcrop studies (Jakobsen 1996; Toft *et al.* 1996; Scholle *et al.* 1998; Stage 1999). The vertical variability can therefore be described fairly accurately in the geostatistic models. With regard to the horizontal variability, only outcrop studies have the lateral extent to quantify the correlation structure, and a fairly long correlation range for both porosity and permeability is indicated from such data. Investigations of outcrops at Stevns (Zealand, Denmark) on a horizontal section of 30 m in Upper Maastrichtian chalk, show that the horizontal correlation range could be much larger than the 30 m extent (Frykman 1994). This would give rise to significant zonal anisotropy of layered chalk sections.

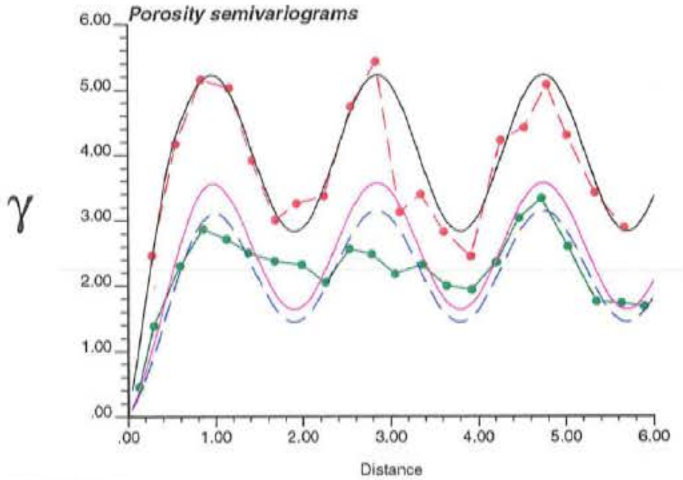

Figure 72
Experimental variograms for the core data and the log porosity data. The uppermost line with dots is the experimental variogram for the core data, and the stippled line is the model variogram for core scale. The lower stippled line with dots is the experimental variogram for the log porosity data, and the full and stippled line are the theoretical predictions of upscaled variogram assuming 50 and 60 cm averaging length of the log tool respectively.

The amplitude or variance of the porosity is, however, reduced in the log-interpreted porosity data compared to the core analyses extracted from the material in the same section. This is due to the different resolution of the tools used. The wireline log tool for porosity has an effective resolution of about 50-60 cm, whereas the core analysis naturally has the plug size resolution which is about 2 cm. This is illustrated earlier where the core data is seen to have a larger range of values than is reflected in the log-interpreted porosity, and likewise the difference in sill value in the variogram in Fig. 72.

Geostatistic modelling

The fine-scale geostatistic type models in the first step of upscaling are generated in a string of 20 as a vertical 2D model measuring 1 x 20 m. An elementary volume of 5 x 2 x 2 cm for the constitutive cells has been chosen. This size mimics the typical standard one inch plug normally taken from core material and used in core analysis studies, i.e. a section model comprises 20000 simulation grid cells. The individual 2D model used for the upscaling comprises 1000 cells, and if extended into 3D it would comprise 50.000 cells. This size of the first simulation step is sufficiently small to be efficient to work with in a flow simulator, and is at the same time large enough to describe the heterogeneities existing at the scale of a m^3. The 2D vertical slab geometry has been chosen as a first model geometry because of the distinctive layering and anisotropy of the chalk as described previously.

As long as there is no difference in directional variations in the lateral dimension, the principle of using 2D-derived properties for the next step is considered safe to follow for other upscaling steps.

It should be mentioned that if the upscaling procedure for the model were made to incorporate effects from fracture patterns, this simple scheme of using only 2D models could lead to significant errors in the connectivity, as the main connectivity for fracture patterns is normally greatly dependent on the 3D geometry of the network. In this study only matrix properties are investigated, and the 2D approach is considered valid for the present purpose.

The size and scale of the upscaling steps that follow should be guided by the evaluation of the heterogeneities that are expressed at the larger scales. This includes, for example, the vertical trend in average porosity which is often seen close to the top of the main reservoir section in the Upper Maastrichtian interval.

Modelling procedure

The geostatistic models are generated in several steps with a routine for sequential gaussian conditional simulation (SGSIM) from the geostatistic program library GSLIB (Deutsch & Journel 1997).

The first simulation generates a porosity model with cells of 0.02 m scale for the porosity distribution as recorded in the logging data. This step is mainly to create a dataset with full coverage at the 2 cm scale which is going to be used as soft data for the simulation of the core scale data in the next step. SGSIM is using the log data point values at half-foot intervals as hard data, a variogram model derived from the log data, and a target histogram for porosity also derived from the log data in the section. The generated data set is synthetic regarding its resolution, but is only used for the guiding of the porosity simulation based on the core data in the following step.

1. This step is a simulation of an exhaustive porosity model at the core scale (2 cm scale) using the measured core plug porosity data from the section as hard data, and the previously generated model of the well log porosity data as soft data. The link between the two porosity data sets is given as the correlation coefficient of 0.7 as estimated between the log and core porosity. The variogram model used is derived from analysis of the core data. The target histogram cannot solely be taken from the core data in the section since the amount of data points is limited. Therefore a synthetic normal distribution of porosity values with mean and variance as the core data is generated and used for target histogram for the simulation.
2. Having the core scale porosity model we can derive the permeability model by simulation using the previous porosity model as soft data for the simulation. The variogram model is assumed similar to that for the porosity data. The target histogram is estimated using the bivariate relation between porosity and permeability as analysed from existing core data from the whole Dan Field in a model-based declustering scheme. This scheme including co-simulation of the permeability distribution is nearly similar to that described in other chalk modelling studies (Frykman & Deutsch 1996; Frykman *et al.* 1997).

Step 1: Porosity modelling – well log data

The model of the log porosity is established mainly to have the log data available as soft data for the subsequent modelling of core scale data. Therefore the model is generated in order to mimic as closely as possible the original log data recorded at half foot intervals, and at the same time cover the fine scale of 2 cm, by having values posted at this scale. The smoothness of the log porosity curve is ensured by using a gaussian variogram model including a small nugget value to stabilise the simulation. The model variogram used for the simulation is shown in Fig. 74.

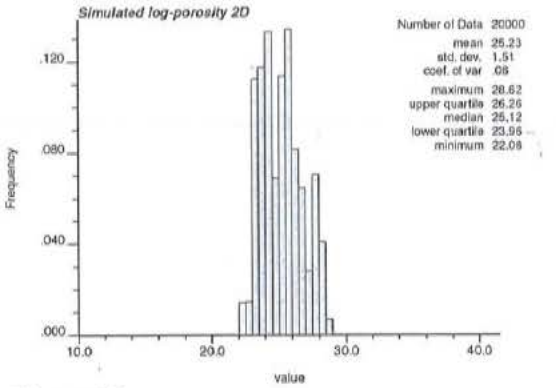

Figure 73
Histogram of simulated log porosity model at fine scale.

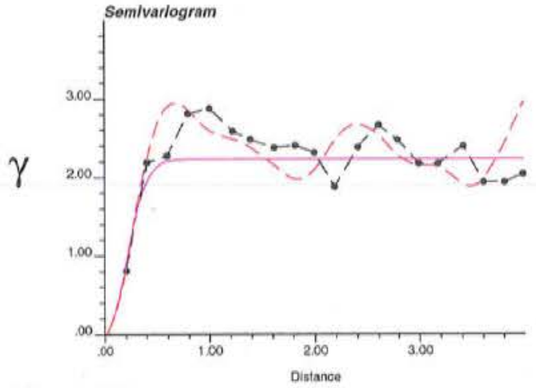

Figure 74
Variograms for the log porosity data (dashed line with points), the variogram model (line) used for simulation and the variogram for the resulting porosity model (dashed line).

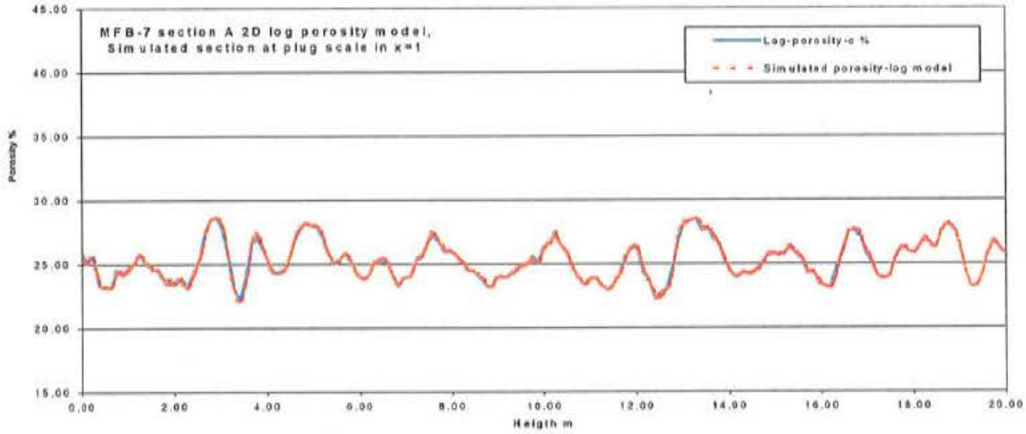

Figure 75
Comparison of original log porosity data and the simulated log porosity model at fine scale.

Step 2: Modelling of core porosity

The common scarcity of core analysis data in many parts of the reservoir, however, normally reduces the possibility of precisely describing the correlation structure of porosity and permeability at the cm scale resolution which is needed for general models at this scale. However, this specific section selected has good coverage of both types of data, and therefore illustrates the scaling relation between core- and log-scale data. The difference in variance between the two types of data is also shown by the histograms for porosity data from the same section from logs and core analysis respectively (see figs. 65, 66). The different variance of porosity has also been illustrated in a study where the porosity at fine resolution has been obtained by means of core density scanning and compared to wireline log data in the same

section (Lind & Grøn 1996).This relation is also shown in the chapter on density core scanning.
For the modelling purpose of this particular section, an estimate of the target porosity distribution has to be established prior to the simulation of the porosity model. This estimation is simplified by constructing a normal distribution with the mean value and variance taken from the core porosity data from that section. The target population is shown in (Fig. 76).
The variogram model used for the simulation is the one obtained from analysing the core plug data from the section (Fig. 72).
The simulation is carried out with the collocated cokriging option using the prior log porosity model as soft data with a correlation coefficient of 0.7 as shown by the crossplot between the two porosity data types (Fig. 67). Thereby the log porosity guides the simulation in intervals where no hard data from core plugs exist (Fig. 77). The honouring of the variogram model is shown in Fig. 78, and the histogram of the simulated core porosity model is shown in Fig. 79.

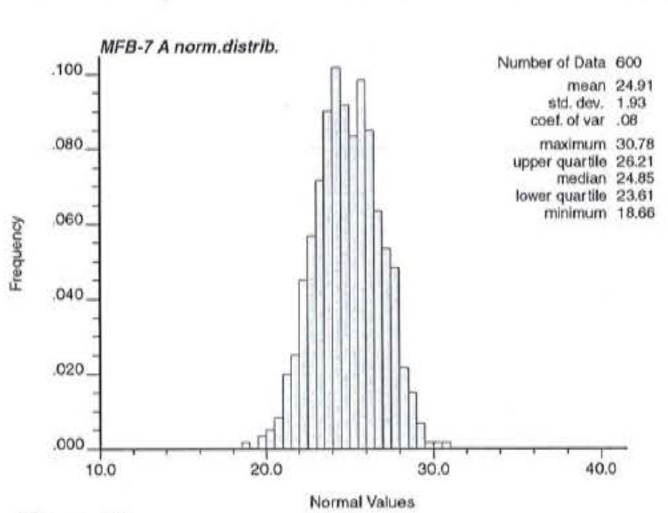

Figure 76
Target porosity distribution is obtained with the Drawnorm 'program for generating 600 values with the target mean of 24.78 and the variance of 4.0 taken directly from the core data.

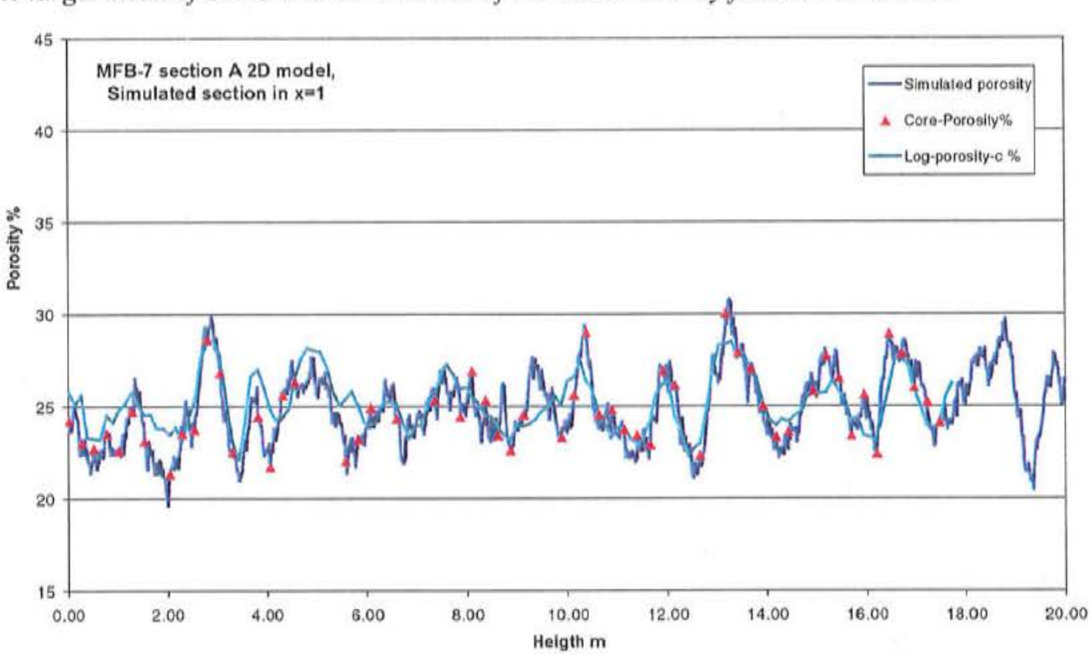

Figure 77
Comparison of the simulated porosity at core scale with the data from the core plugs and the log porosity.

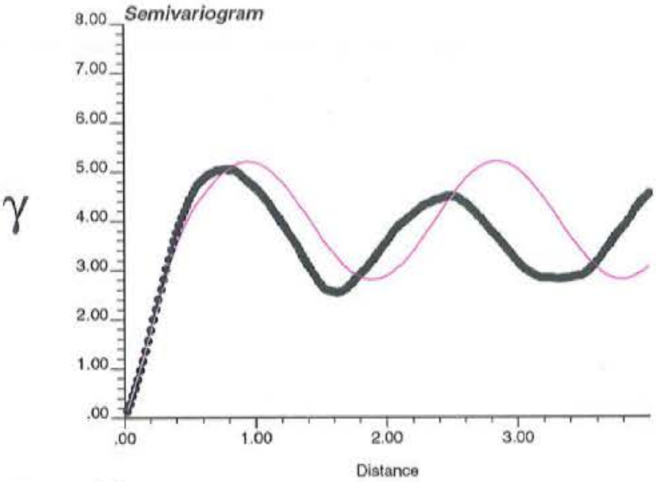

Figure 78
Variogram model for the core porosity simulation (pink line) and the experimental variogram for the simulated porosity model (dotted line). The shorter range for the hole effect is a result of the influence from the log data.

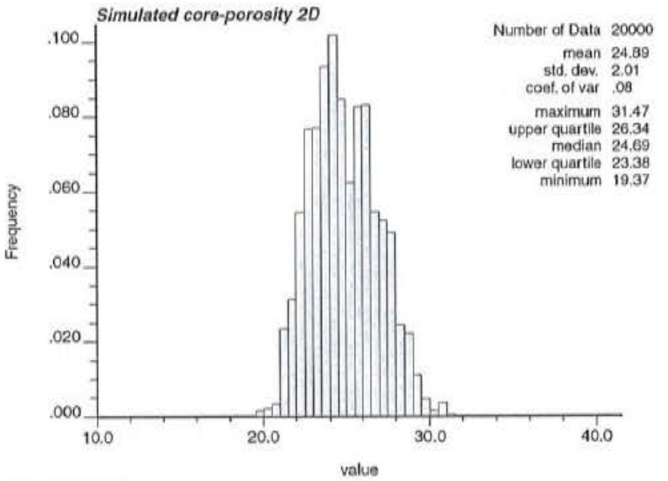

Figure 79
Histogram of simulated core porosity.

Step 3: Permeability modelling

The simulation of the permeability model is carried out with SGSIM and the collocated cokriging option, using the core porosity model as soft data with a correlation coefficient of 0.7 to the permeability. The crossplot of the core plug porosity-permeability is not very informative due to the limited amount of data (Fig. 80), therefore a larger population has been obtained from the upper Maastrichtian section in the Dan field to illustrate the general relation between porosity and permeability (Figs. 81, 82). A synthetic relation has been constructed limiting the permeability variance of this population and is shown as decile lines (10% fractions) in Fig. 82.

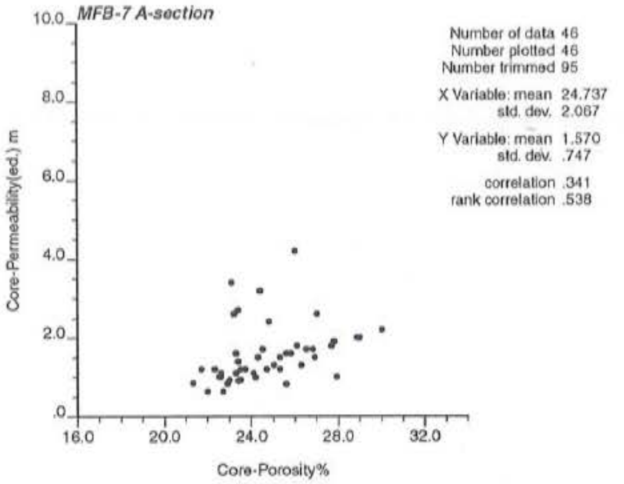

Figure 80

The core porosity and permeability values show a rank correlation of ca. 0.5, which is accounting slightly for the influence of the outlier points on the diagram.

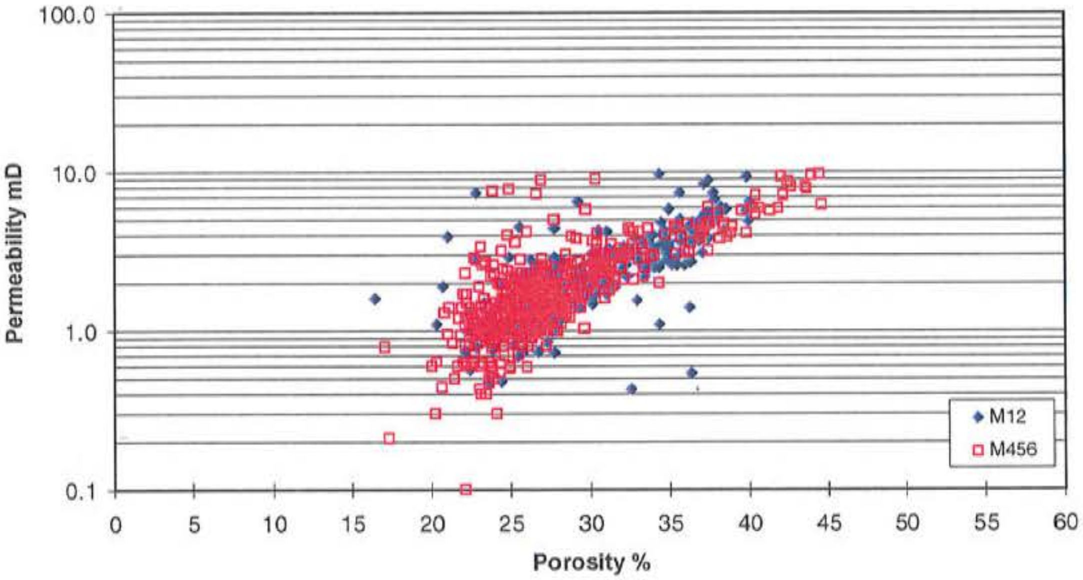

Figure 81

Data for porosity-permeability from two different reservoir units in the Dan Field, M12 (Uppermost Maastrichtian) and M456 (Upper Maastrichtian).

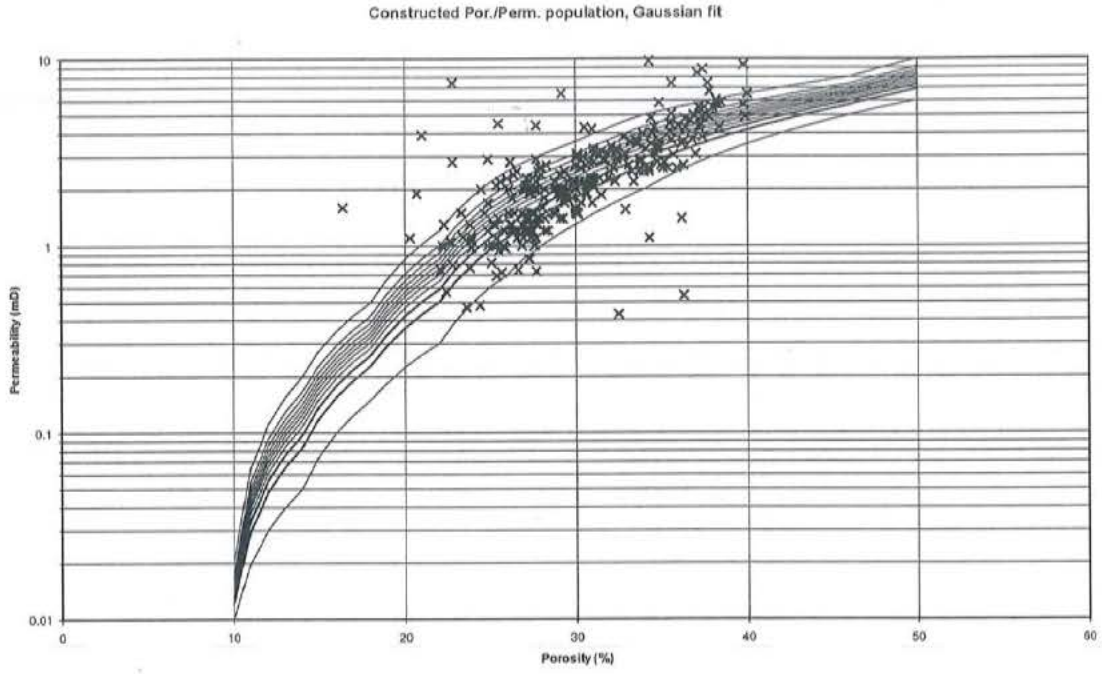

Figure 82
The constructed bivariate population of porosity-permeability based on the data from M12. The curves delineate the deciles (10% fractions) of the conditional probability distribution function (cpdf) for the permeability for every porosity measure.

This bivariate description is used for a model-based declustering in order to obtain a predicted target population of permeability for the full range of porosities Figs. 83, 84. For the present porosity interval in the selected section this population is limited as shown in (Fig. 85), and the histogram in (Fig. 86).

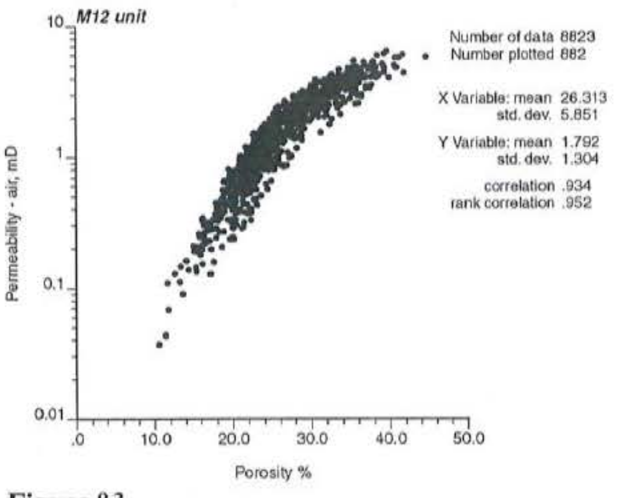

Figure 83
The declustered porosity-permeability population for M12 unit.

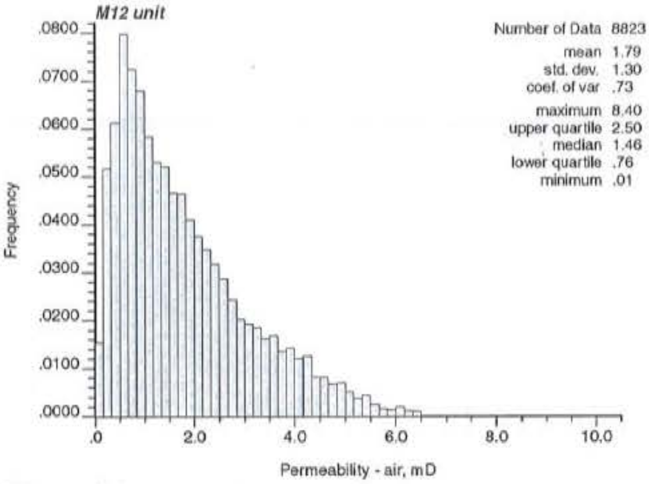

Figure 84
Histogram of the total declustered permeability population for the whole M12 unit.

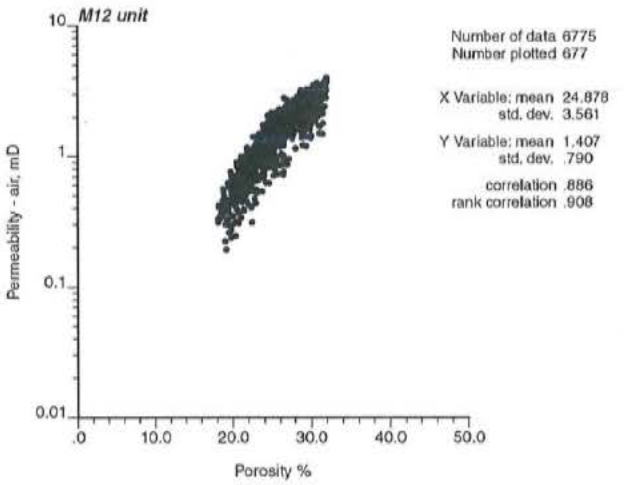

Figure 85
The subpopulation of porosity-permeability used for the simulation of permeability in the selected section.

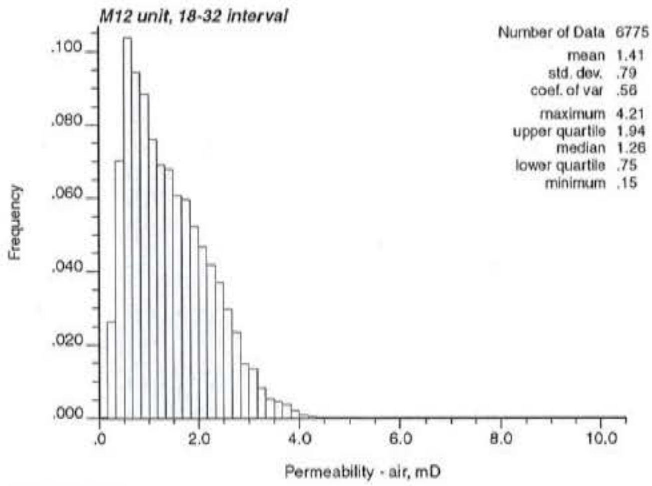

Figure 86
Histogram of the permeability subpopulation for the porosity interval of 18-32 % used for the target distribution for the simulated permeability.

The simulation of permeability at core scale is carried out with SGSIM using the collocated cokriging option with the prior core porosity model as soft data with a correlation coefficient of 0.7 to the simulated core permeability. Although the correlation between porosity-permeability in the selected section is 0.5 as shown in Fig. 91, the variability of permeability is assumed to be less than shown by the data present, and therefore with increased correlation. The resulting permeability model for the section is shown in Fig. 87, and the histogram of the simulated permeability in Fig. 88.

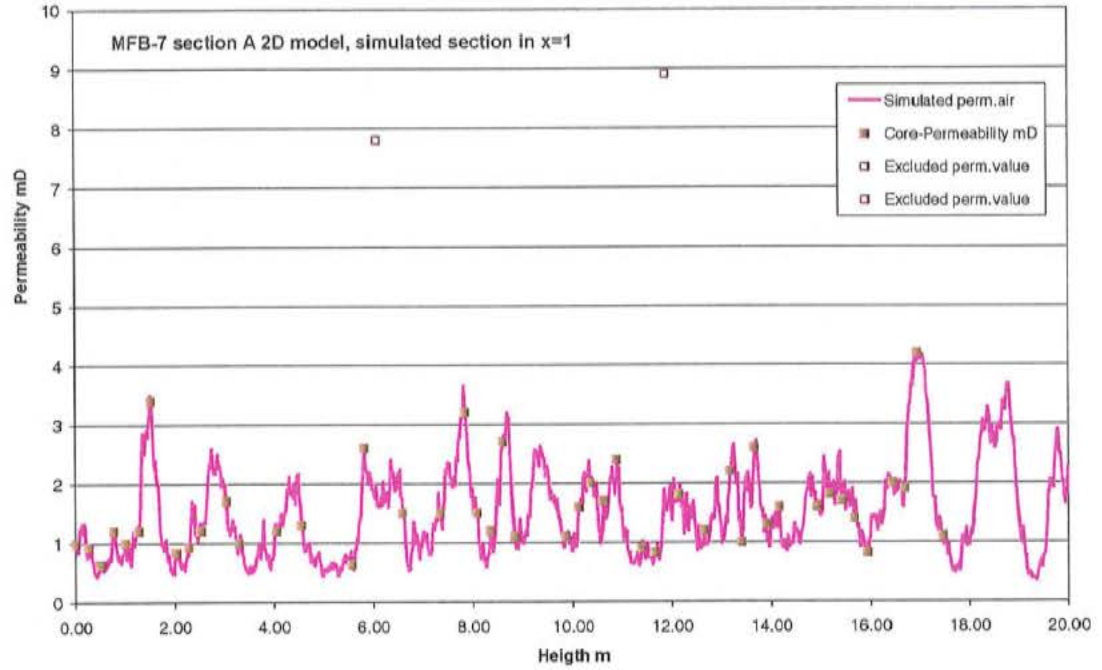

Figure 87
Section with the simulated permeability at core scale.

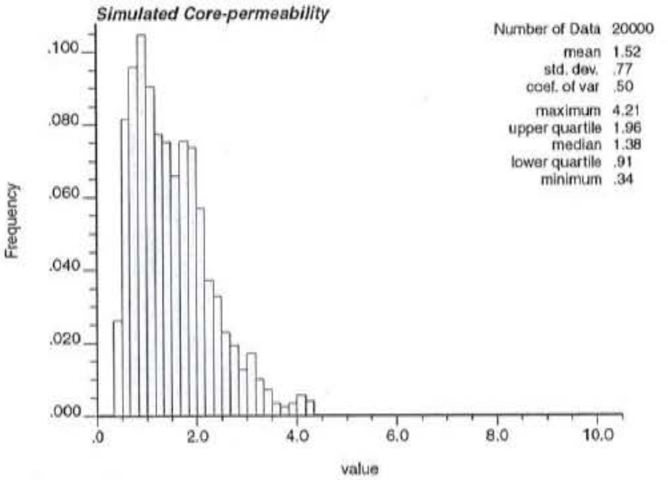

Figure 88
Histogram of the simulated permeability.

The honouring of the variogram model is shown in Fig. 89, and a comparison between the porosity and permeability models are shown in Fig. 90.

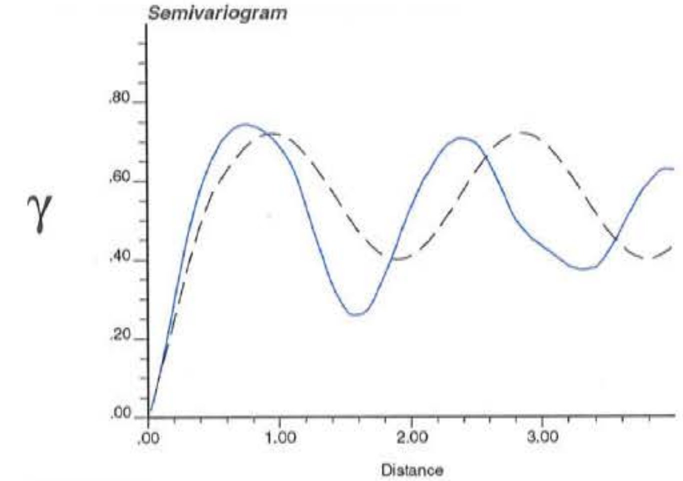

Figure 89
Variogram for the permeability model (blue line) simulated with 0.7 correlation to the prior simulated core porosity model. Dashed line is the input variogram model.

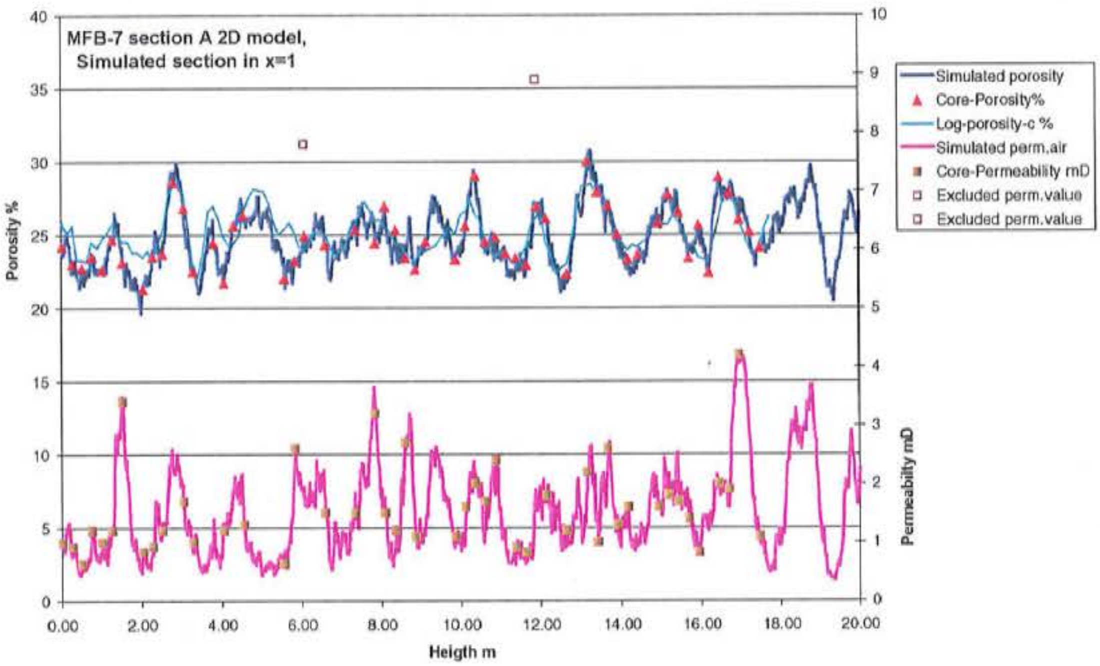

Figure 90
Comparison of the simulated porosity and permeability for the section.

Step 4: Permeability conversion

The permeability used in this modelling is the gas permeability, as this is the basic data derived from cores and outcrops. However, in such low permeable materials as chalk, the absolute permeability is fluid-dependent. Gas absolute permeability e.g. is higher than that obtained by using a liquid. The transformation into liquid permeability is based on the existing concurrent analysis of air and liquid measured permeability or alternatively Klinkenberg-corrected permeabilities. The equation used is:

$$\mathrm{Perm}_{(\mathrm{fluid})} = 0.52 \times \mathrm{perm}_{(\mathrm{air})}^{1.083}$$

The porosity-permeability relation for fluid relevant data is shown in Fig. 91.

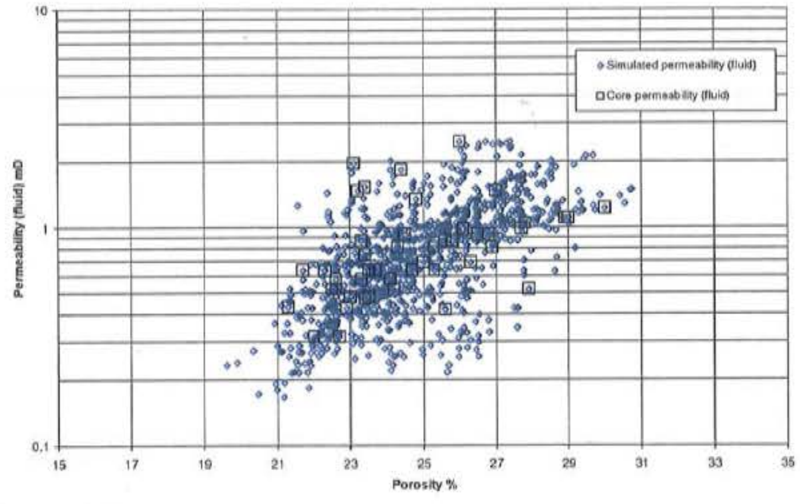

Figure 91
Porosity-permeability(fluid) comparing the core permeability data and the simulated model. The simulation has preserved the variability that was described via the correlation coefficient and the target histogram for permeability.

Conclusion

By using geostatistic analysis and conditional simulation it is possible to honour the data existing in a sequence and their scaling relationships, and generate a model of the full 3D porosity and permeability distribution. The method is applied to the present chalk reservoir example showing a pronounced layered or cyclic development of both porosity and permeability, but in principle the method can be developed to model other types of heterogeneity and variations in their geometry.

UPSCALING OF FINE-SCALE GEOMODELS

Introduction

This report presents procedures for analysing fine-scale geomodels. The geomodels are constructed in order to carry original measured data at the correct scale in the input stage. This is achieved by selecting cell size at the same scale as the core analysis data used for input. The purpose of investigating these models is to analyse effective properties as a consequence of the layering and contrasts in the model. The detailed geomodel has been subjected to single-phase flow simulation, and the average anisotropy factor k_V/k_H can be derived for each model. The porosity/permeability relation for the effective properties reflects the upscaling that is carried out with this procedure.

Example of upscaling

The previous chapter described the construction of a type model section measuring 20 x 1 m (2D) with the constitutive cells of plug-size (5x2x2 cm = 20 cm^3) resulting in 20000 cells in the 2D model.

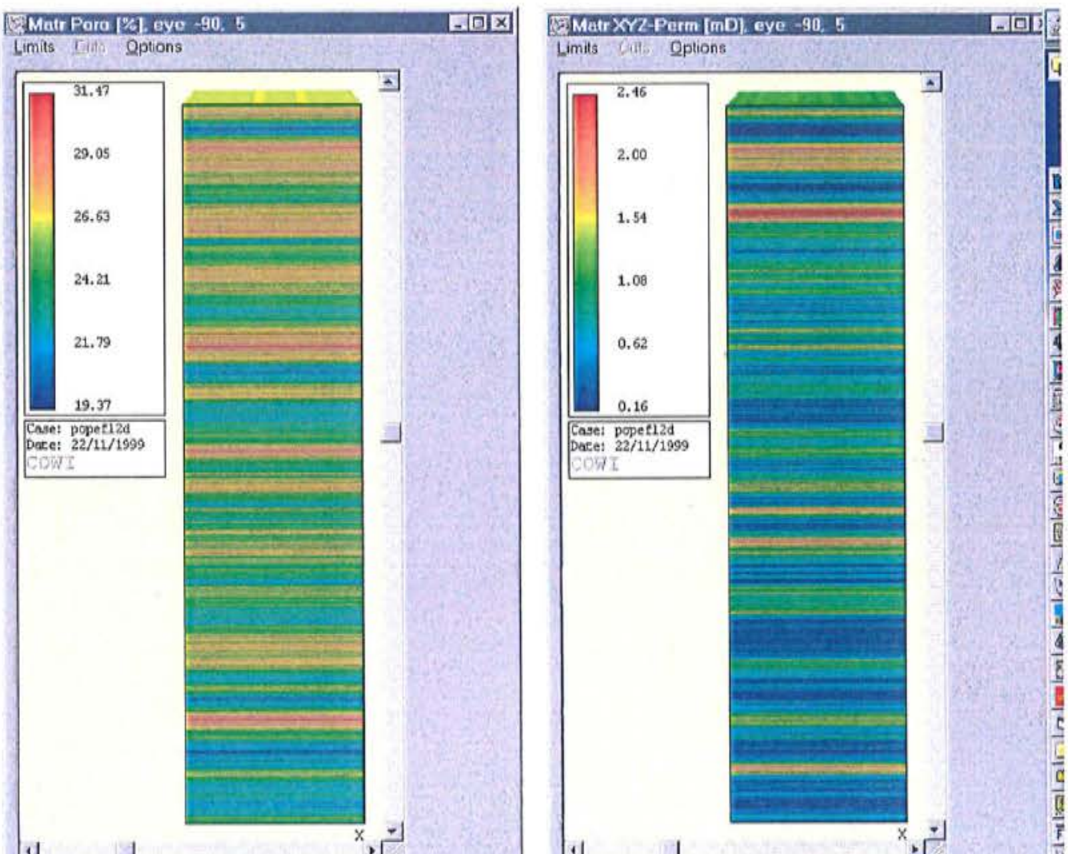

Figure 92

2D models of the 20 m high section simulated using data from the section a in the MFB-7 well.

Extension into 3D is possible (1 mio. cells) if required by the spatial pattern of heterogeneity (Fig. 93).

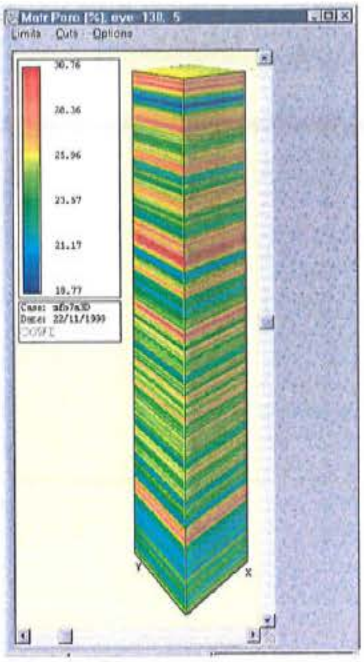

Figure 93
3D model of porosity distribution in section A. The layering is seen to be very regular.

The 20 m model section is then subdivided into 20 individual cubicmeter size type models that are used for the upscaling exercise. In this way we get an evaluation of the variability of the impact of heterogeneities existing in a limited section of a chalk reservoir. To illustrate the upscaling concept for the present study of single-phase flow, one single 2D model of 1x1 m is selected as the lowermost block in the 20 m section modelled. The porosity and permeability models are shown in Fig. 94, and property distribution and relation in Figs. 95, 96. For this upscaling study, the program *FracSynt©* has been used throughout to visualise the models and calculate the effective properties.

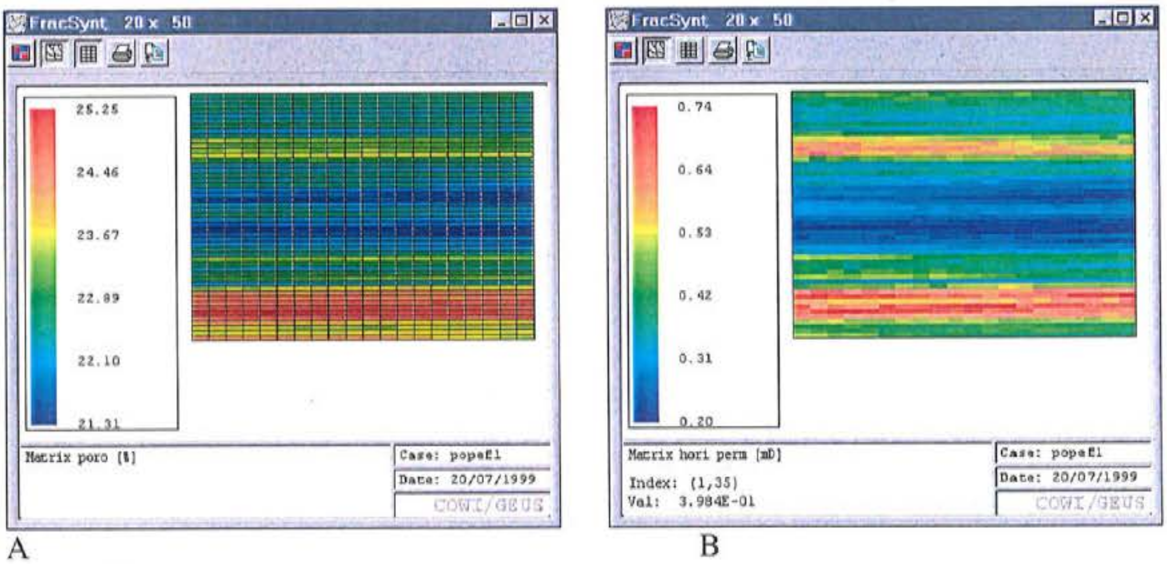

Figure 94
A: Porosity model for block-1 showing the layering. The overlain grid shows the plug size cells in the simulation model. B: Permeability (fluid) model for block-1 showing the layering and correspondence to the porosity model due to the cosimulation.

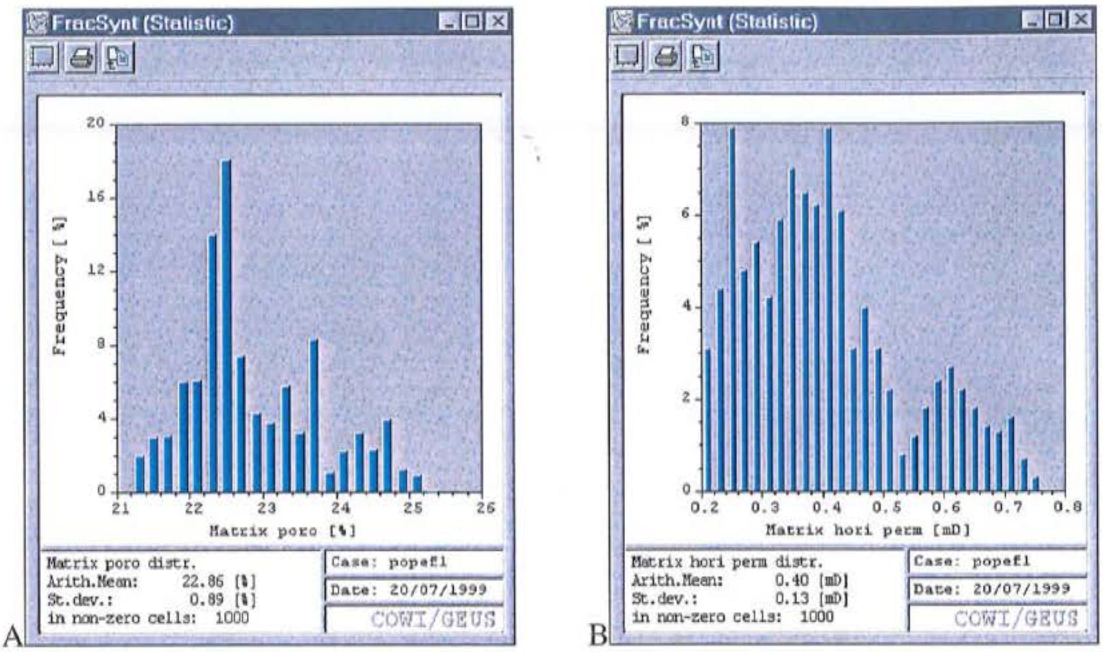

Figure 95

A: Histogram of the porosity values in block-1 having a mean (upscaled) porosity of 22.86.
B: Histogram of horizontal permeability (same as vertical permeability for the plugs) with the arithmetic mean of 0.40 equal to the upscaled horizontal permeability.

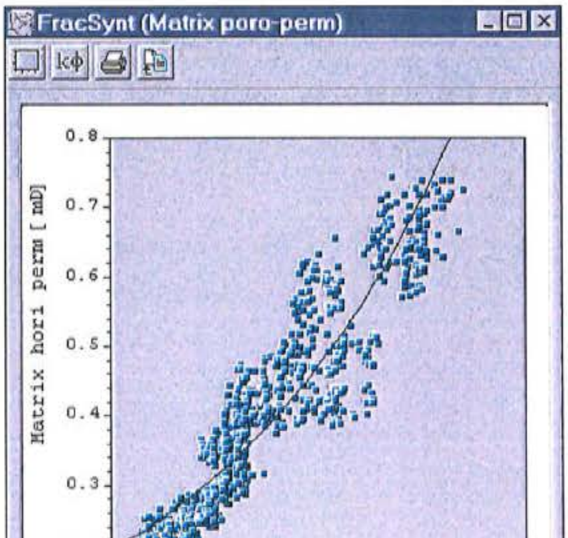

Figure 96

Plot of values in block-1 that shows the bivariate relation between porosity and permeability as derived during simulation. The regression parameters for the line is given.

For the upscaling of the single-phase flow in the present model, a finite difference pressure solver based reservoir simulation is performed. In order to show both the horizontal and vertical flow, pressure gradients have been imposed in both directions, and the resulting permeabilities k_H and k_V are calculated from the flux registered.
The directional permeability is illustrated as a tensor in an x-z coordinate system in Fig. 97. The anisotropy shown is solely caused by the layering in the selected model block.

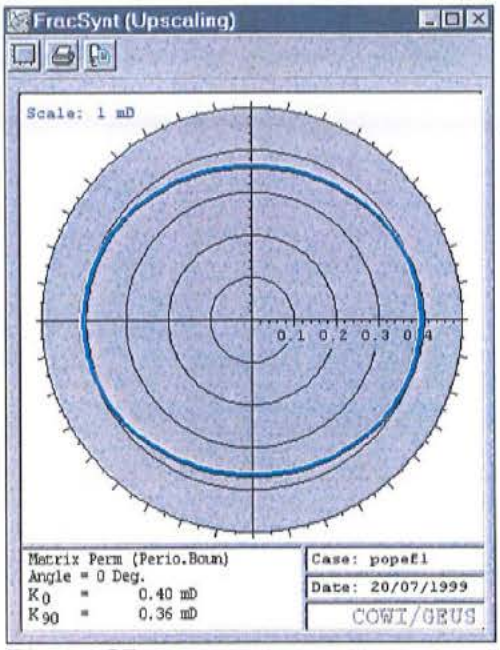

Figure 97

Tensor description of the upscaled permeability for block-1 showing a k_V/k_H value of 0.9 due to the layering.

This upscaling scheme is repeated for all the 20 blocks in the model section, and their effective upscaled properties are compared to the finescale model data in Fig. 98. The range of anisotropy values (k_V/k_H) in relation to the horizontal permeability is shown in Fig. 99, and is seen to span from 0.6 to 0.94 depending on the amount of contrast between the layers in the individual blocks.

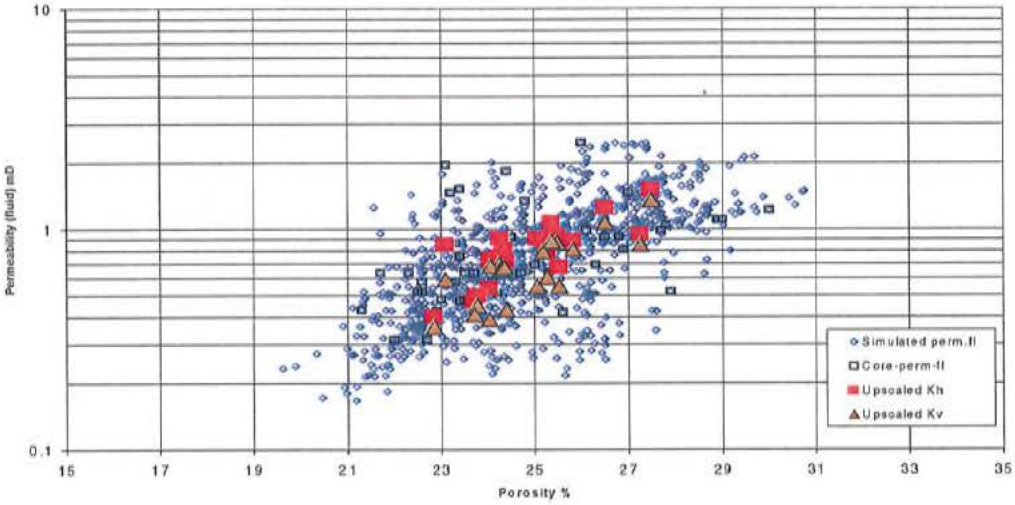

Figure 98

Comparison of the simulated porosity-permeability values in a string through the 20 m long section model and the upscaled values for the 20 individual cubicmeter size models from that section.

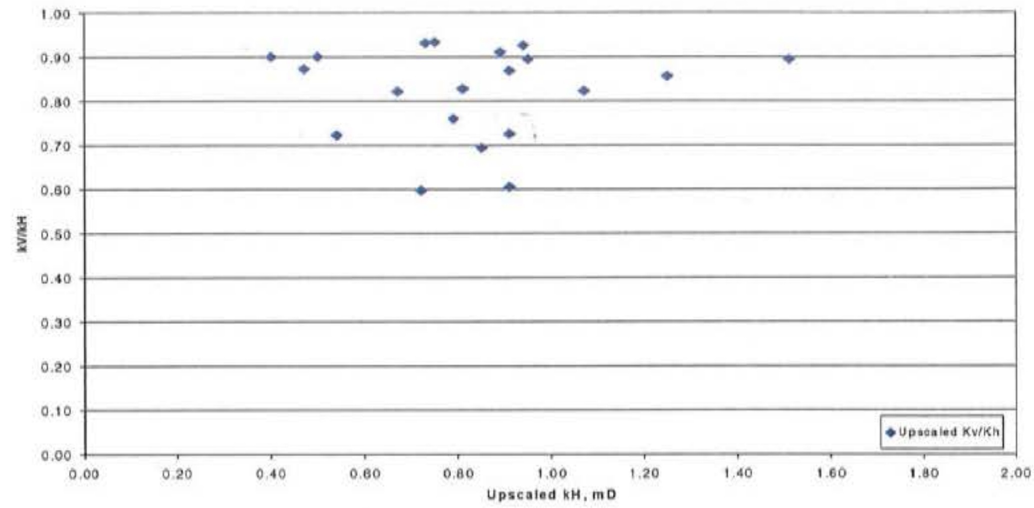

Figure 99
Plot of the resulting k_V/k_H of the upscaled models.

The net anisotropy of the full 20 m long section is seen to be 0.73 which is solely the effect from the layering in this 20 m sequence (Figs 92, 93 and 100). The distribution of porosity and permeability for the full section are seen to be nicely normal and log-normally distributed as shown in Fig. 101.

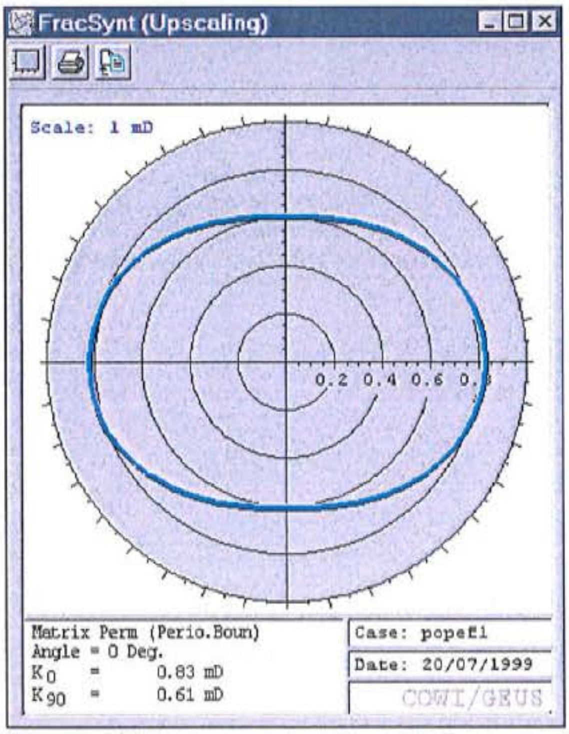

Figure 100
Tensor plot of the upscaled permeability for the full 20x1 m section model. k_V/k_H is 0.73 for the full section.

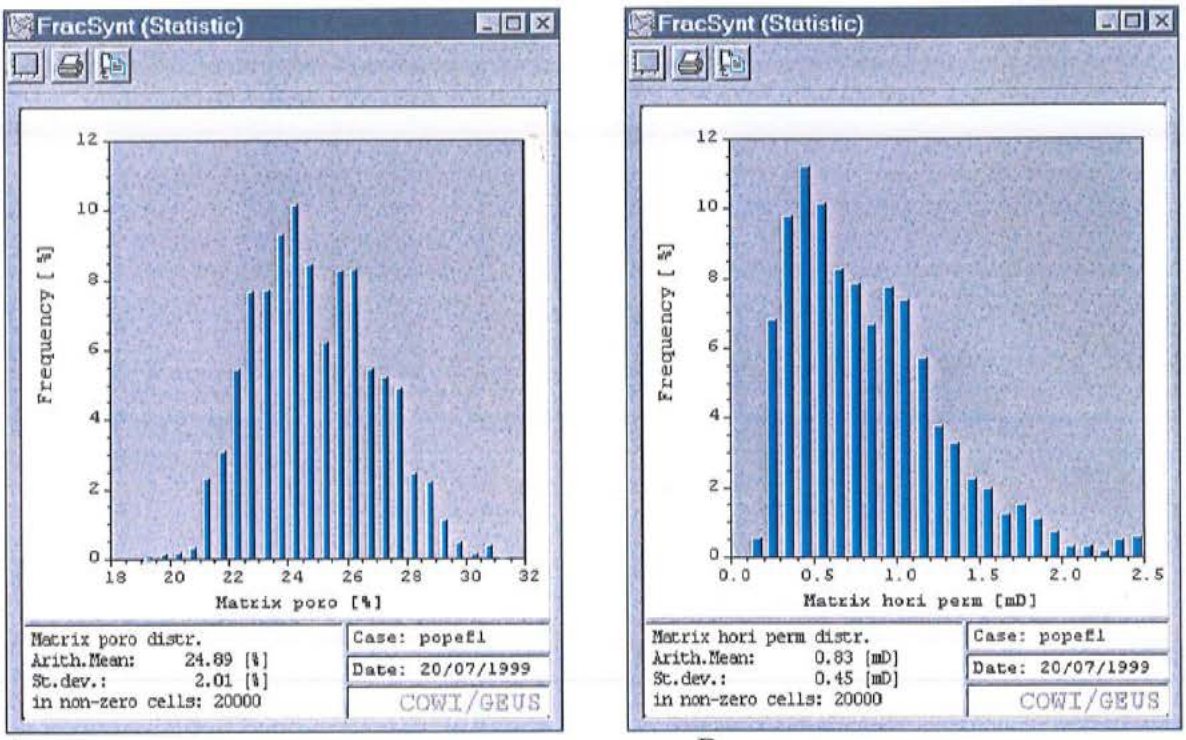

A B

Figure 101

A: Porosity distribution for full 20 m section model, and B: Permeability (fluid).

Conclusions

The upscaling software is shown to be an efficient tool to inspect and visualise the models and their flow effects.

The upscaling of the 20 m section shows that the collection of 1 m^3 blocks has variable effective values including the permeability anisotropy. This has consequences for the concept of type models that has to be abandoned at this scale level. With this small volume, no typical building block can be selected at m^3 scale. Possibly at larger scale a block can be retrieved that shows consistent behaviour and can be used as a type model for that scale level.

References

DEA 1993: Oil and gas production in Denmark. Danish Energy Agency Annual Report 1992(70).

DEA 1997: Oil and gas production in Denmark. Danish Energy Agency Annual Report 1996(69).

Deutsch, C.V. & Journel, A.G. 1997: GSLIB - Geostatistical Software Library and User's guide, 2nd edition, 340 pp.: Oxford University Press, New York City.

Fine, S., Yusas, M.R. & Jørgensen, L.N. 1993: Geological aspects of horizontal drilling in chalks from the Danish sector of the North Sea. In: Parker, J.R. (ed.): Petroleum geology of Northwest Europe: Proceedings of the 4th Conference, 1483-1490. London: The Geological Society.

Frykman, P. 1994: Correlation structure of porosity and permeability in on- and offshore chalks. EAPG/AAPG Special Conference on Chalk, Copenhagen, Denmark, 7-9 September 1994, 36-39.

Frykman, P. & Deutsch, C.V. 1996: Reservoir modelling of the Dan Field accounting for areal trends and scaling of petrophysical properties. Fifth North Sea Chalk Symposium, Reims, France, 7-9. October 1996, 21 pp.

Frykman, P. & Deutsch, C.V. 1999: Geostatistical scaling laws applied to core and log data. SPE Paper 56822 presented at SPE Annual Technical Conference and Exhibition. 3-6 October 1999, Houston, Texas. 12 pp.

Frykman, P., Lindgaard, H.F. & Bech, N. 1997: Fine-scale geomodels as a tool for upscaling in North Sea chalk reservoirs. Danmarks og Grønlands Geologiske Undersøgelse Rapport 1997/86, 31 pp.

Jakobsen, F. 1996: Chalk outcrops - Analogues for offshore chalk reservoirs? Fifth North Sea Chalk Symposium, Reims, France, October 7-9, 19 pp.

Jørgensen, L.N. 1993: Dan Field – Denmark. Central Graben, Danish North Sea. In: Beaumont, E.A. & Foster, N.H. (eds): Atlas of Oil and Gas Fields, 199-215. Tulsa: American Association of Petroleum Geologists

Kristensen, L., Dons, T., Maver, K. & Schiøler, P. 1995: A multidisciplinary approach to reservoir subdivision of the Maastrichtian chalk in the Dan Field, Danish North Sea. American Association of Petroleum Geologists Bulletin 79(11), 1650-1660.

Lind, I. & Grøn, P. 1996: Porosity variation in chalk. Zbl. Geol. Paläont. H. 11/12, 763-772.

Nederveen, N. & Damm, M. 1993: Basal Waterflooding of a Tight Chalk Field with Long Horizontal Fractured Injectors. Offshore Technology Conference, Aberdeen, UK, 1993, (SPE Paper 26802).

Ovens, J.E.V., Larsen, F.P. & Cowie, D.R. 1998: Making sense of water injection fractures in the Dan Field. SPE Reservoir Evaluation & Engineering(December), 556-566 (SPE 52669).

Scholle, P.A. 1977: Chalk diagenesis and its relation to petroleum exploration: Oil from chalks, a modern miracle. American Association of Petroleum Geologists Bulletin 61(7), 982-1009.

Scholle, P.A., Albrechtsen, T. & Tirsgaard, H. 1998: Formation and diagenesis of bedding cycles in uppermost Cretaceous chalks of the Dan Field, Danish North Sea. Sedimentology 45(2), 223-243.

Stage, M. 1999: Signal analysis of cyclicity in Maastrichtian pelagic chalks from the Danish North Sea. Earth and Planetary Science Letters, 173, 75-90.

Toft, J., Albrechtsen, T. & Tirsgaard, H. 1996: Use of cyclostratigraphy in Danish chalks for field development and appraisal. Fifth North Sea Chalk Symposium, Reims, France, 7-9 October 1996, 17 pp.

FracSynt 3D

Flemming If (COWI)

CHARACTERISATION AND MULTISTEP UPSCALING OF FRACTURED CHALK RESERVOIRS.

JCR Phase V, Project no. 3

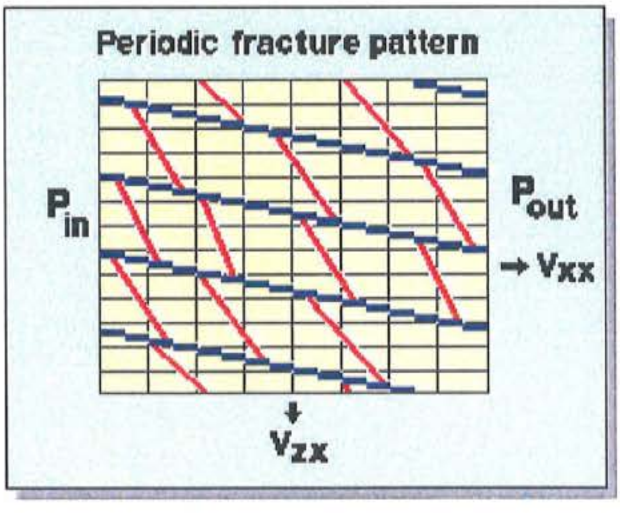

Description of methodology for upscaling

Introduction

FracSynt 3D is a software program for calculation of up-scaled values of absolute directional permeability of fractured rock. This document describes the methodology and principles used in the development of the FracSynt program. The program performs single-phase up-scaling from input of fracture network data, matrix permeability and matrix porosity grid block data. The program can perform up-scaling of directional permeability and porosity to reservoir grid cell size for both single porosity and dual porosity reservoir simulation. FracSynt 3D consist of 4 parts arranged as tools (see Figure 102)

1. A **FracMan file reader** for reading a FracMan file (***.fab**) [1]
2. A **Gridding** tool for calculation of fracture porosity, fracture permeability and fracture directional transmissibilities in user defined grid blocks. The result can be filed and used as input to reservoir simulation.
3. An **Up-scaling** tool for calculation of the absolute directional permeability of:
   a: the fracture pattern, (Fracture data in a dual porosity model)
   b: the matrix (Matrix data in a dual porosity model)
   c: the combined fracture pattern and matrix. (Matrix data in a single porosity model)
4. A **Viewing** tool which can be used for generating 3D-maps of grid block data, plot of up-scaled permeability, data distributions and logs.

In later sections the calculations in the gridding tool are described. The gridding tool computes the grid cell fracture porosity, the fracture permeability and the grid cell transmissibilities from the fracture network geometry and the fracture apertures. The matrix- and the fracture permeability and the combined matrix and fracture permeability at grid cell interfaces are calculated, and the single-phase up-scaling procedure for both periodic and non-periodic fracture networks performed by the up-scaling tool is described. The porosity to permeability relation and the air- to fluid-permeability conversion as implemented in FracSynt are described.

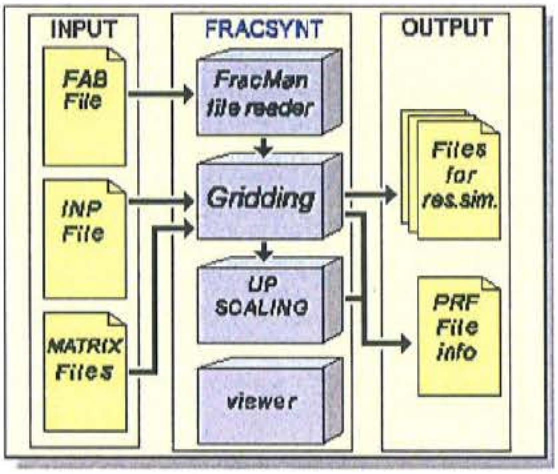

Figure 102. Program structure

[1] Fracman is a commercial software program from Golder Associates (UK) Ltd., which can generate 3D fracture patterns.

Gridding of fracture porosity

Generally, the porosity is the ratio between the volume available for hydrocarbons/water and the bulk volume.
The fracture porosity in a grid cell is calculated as the fracture volume within the grid cell divided by the grid cell volume.

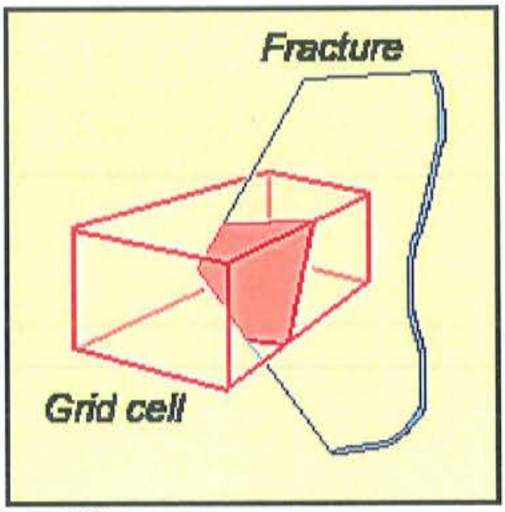

Figure 103
Fracture volume in grid cell

The fracture volume is the area of the fracture inside the grid cell times the fracture aperture.

For each grid cell FracSynt examines which fractures intersect the grid cell.

The total fracture volume in a grid cell is calculated as the sum of the volumes of all the fractures intersecting the grid cell.

The resulting grid cell porosity, φ, is calculated as:

$$\varphi = \frac{\sum_{\text{Fractures in grid cell}} \textbf{Fracture area} \cdot \textbf{Fracture aperture}}{\textbf{Grid cell volume}} \qquad (2.1)$$

Example
Porosity of fracture with mechanical aperture of 50 microns passing vertically through a grid cell of size 0.05m x 0.05m x 0.05m is: 0.1%

File
The calculated fracture porosity can be saved in a file. Name: **Porf**nxnynz**.dat**

The file contains the calculated fracture porosity in each of the grid cells written as one column of numbers in ASCII format.
The x-index cycles faster than the y-index, which cycles faster then the z-index in a co-ordinate system with the z-axis pointing downwards.
The file may be included in an input file for reservoir simulation.

Gridding of fracture permeability

The grid cell intrinsic fracture permeability, K_f, is calculated from the hydraulic aperture (***Ah***) and the mechanical aperture (***Am***), both apertures are given in microns.

$$K_f = 1013.25 \cdot \left(\frac{Ah^3}{12 \cdot Am} \right) [mD] \ . \qquad (3.1)$$

In case the mechanical aperture equals the hydraulic aperture (no roughness) the intrinsic fracture permeability formula reduces to the parallel plate formula.

In case a grid cell contains more than one fracture type a hydraulic aperture weighted average permeability is assigned to the grid cell,

$$K_f = 1013.25 \cdot \frac{\sum_n \left(Ah_n \cdot \left(\frac{Ah_n^3}{12 \cdot Am_n} \right) \right)}{\sum_n Ah_n} [mD] \ , \qquad (3.2)$$

where the sums are over all fracture types inside the grid cell.

The hydraulic aperture in microns is given by the mechanical aperture in microns and the Joint Roughness Coefficient (JRC):

$$Ah = \frac{Am^2}{JRC^{2.5}} \qquad (3.3)$$ [2]

Examples

Mechanical aperture =	500	micron, JRC = 20,	intrinsic perm: 4000 D
Mechanical aperture=	1000	micron, JRC = 15	intrinsic perm: 15000 D
Hydraulic aperture =	100	micron,	intrinsic perm: 844 D

File
The calculated fracture absolute permeability can be saved in a file.
Name: **Prmf**nxnynz**.dat**

The file contains the calculated fracture permeability in each of the grid cells written as one column of numbers in ASCII format.
The x-index cycles faster than the y-index, which cycles faster then the z-index in a co-ordinate system with the z-axis pointing downwards.
The file may be included in an input file for reservoir simulation.

[2] BARTON, N., 1973. REVIEW OF A NEW SHEAR-STRENGTH CRITERION FOR ROCK JOINTS: ENGINEERING GEOLOGY 7, PP. 287-332.

Gridding of fracture transmissibility factors

The effective fracture permeability between two neighbour grid cells (m and n) with the interface permeability K_{mn} is given by

$$K_{eff} = \frac{\textbf{fracture area at interface}}{\textbf{grid cell interface area}} \cdot K_{mn} \qquad (4.1)$$

K_{mn} is calculated from intrinsic permeabilities, as discussed in section 5.

The fracture area at interface of a single intersecting fracture is calculated as the length of the intersection times the hydraulic aperture of the fracture.

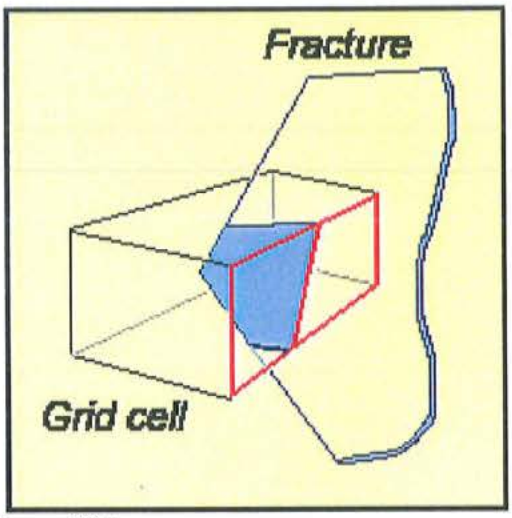

Figure 104
Fracture area at grid cell interface

For each grid cell in the model FracSynt will examine which fractures intersect the grid cell interface. The fracture interface area is calculated as the sum of the areas of all the fractures intersecting the grid interface.

The fracture transmissibility factor, ***FD***, is the multiplication factor on the grid cell interface permeability,

$$FD = \frac{\textbf{fracture area at interface}}{\textbf{grid cell interface area}} \qquad (4.2)$$

File
The horizontal and vertical fracture transmissibility factors can be saved in a file.
Name: **Xtr**fnxnynz**.dat, Ytr**fnxnynz**.dat** and: **Ztrf**nxnynz**.dat**.

The file contains the calculated horizontal and vertical fracture transmissibility factors in each of the grid cells written as one column of numbers in ASCII format.
The x-index cycles faster than the y-index, which cycles faster then the z-index in a co-ordinate system with the z-axis pointing downwards.
The file may be included in an input file for reservoir simulation

Permeability at cell interfaces

The matrix permeability is calculated at the interface between two cells (index m and n)

$$K_{m-n}^{matr} = \frac{Dh_m + Dh_n}{Dh_m / K_m^{matr} + Dh_n / K_n^{matr}} \tag{5.1}$$

Where Dh_m and Dh_n are the grid cell size of grid cell m and n, respectively, in the direction perpendicular to the interface plane. The matrix grid cell interface permeability is used when up-scaling the matrix and the combined matrix and fracture permeability.

The fracture permeability is calculated at the interface

$$K_{m-n}^{frac} = \frac{Dh_m + Dh_n}{Dh_m / K_m^{frac} + Dh_n / K_n^{frac}} \tag{5.2}$$

The fracture grid cell interface permeability is used when up-scaling the fracture permeability and the combined matrix and fracture permeability.

The effective matrix and fracture permeability is combined through the interface transmissibility factor, FD (see section 4)

$$K_{eff,m-n}^{comb} = FD_{m-n} \cdot K_{m-n}^{frac} + (1 - FD_{m-n}) \cdot K_{m-n}^{matr} \tag{5.3}$$

The effective matrix and fracture grid cell interface permeability is used when up-scaling the combined matrix and fracture permeability.

Up-scaling

The up-scaling procedure is based on Darcy's law and mass balance equations. The equations is solved by a 1-phase steady state flow equation for an incompressible fluid on the user-specified grid with either

the matrix grid cell interface permeabilities only,

the calculated fracture grid cell interface permeabilities only, or

a calculated effective combined matrix and fracture grid cell interface permeability.

The up-scaled matrix and fracture permeabilities are intended for use in dual porosity reservoir simulation models while the combined matrix and fracture permeability is for use in single porosity models.

Periodic boundary conditions are imposed thereby enabling the calculation of cross-flow, i.e. a full tensor description of the permeability is implemented. The off diagonal terms in the permeability tensor are a measure of the flow perpendicular to the pressure gradient.
The flow equation is solved three times with pressure gradients applied in the x- the y- and the z-direction, allowing for calculation of all nine elements in the permeability tensor.
The solution to the flow equation is the flow velocity, V, between each grid cell. Average x, y and z flow velocities are calculated for the entire block and up-scaled permeabilities are calculated from Darcy's equation.

Periodic fracture patterns

The boundary conditions imposed are periodic, apart from an applied pressure gradient, (P_{in}-P_{out})/Length.

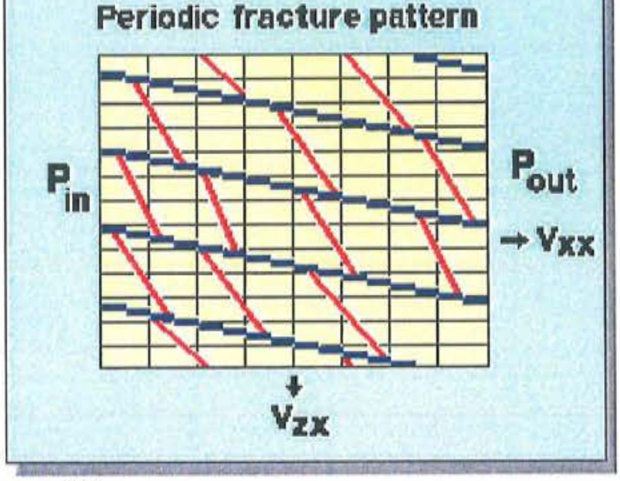

Figure 105
Periodic fracture pattern

The x-permeability corresponding to a pressure gradient applied in the x-direction, Kxx , is obtained from the calculated average flow velocity, Vxx , in the x-direction

$$V_{XX} = \frac{K_{XX}}{\mu} \cdot \frac{P_{in} - P_{out}}{\Delta x} \quad , \tag{6.1}$$

where μ is the viscosity and Δx is the length in the x-direction of the entire block.

The y-permeability corresponding to a pressure gradient applied in the x-direction, Kyx , is obtained from the calculated average flow velocity, Vyx , in the y-direction

$$V_{YX} = \frac{K_{YX}}{\mu} \cdot \frac{P_{in} - P_{out}}{\Delta x} \ , \ (\mu = 1) \tag{6.2}$$

The z-permeability corresponding to a pressure gradient applied in the x-direction, Kzx , is obtained from the calculated average flow velocity, Vzx , in the z-direction

$$V_{ZX} = \frac{K_{ZX}}{\mu} \cdot \frac{P_{in} - P_{out}}{\Delta x} \ , \ (\mu = 1) \tag{6.3}$$

The x- , y- and z-permeability corresponding to pressure gradients applied in the y- and z-direction, K_{xy} , K_{yy} , K_{zy} and K_{xz} , K_{yz} , K_{zz} is calculated likewise.

All nine directional permeabilities are determined from the three flow calculations and the permeability can be presented as the tensor:

$$K = \begin{bmatrix} Kxx & Kxy & Kxz \\ Kyx & Kyy & Kyz \\ Kzx & Kzy & Kzz \end{bmatrix} \quad (6.4)$$

In case where the off-diagonal permeabilities are non-zero, the main flow direction will be estimated by determination of the angles (dip and azimuth) in a rotation of the co-ordinate system that minimises these off-diagonal permeabilities.

Non-periodic fracture patterns

For non-periodic fracture patterns three buffer zones are attached to the target volume, two vertical slices and a horizontal layer that connects fractures at opposite edges. These additional grid cells are connected to the fractures in the target area through a high permeability fracture as shown in figure 106

The steady state flow equation is solved with periodic boundary conditions in this enlarged area.

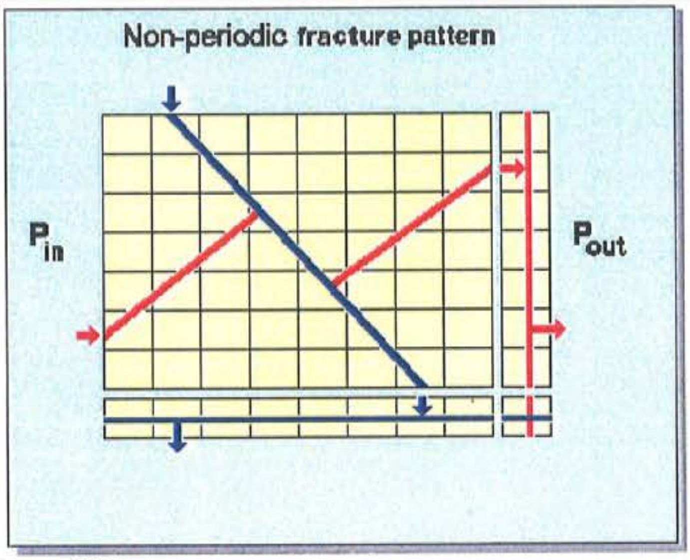

Figure 106
Non-periodic fracture pattern

The permeability tensor is then calculated for the non-periodic fracture pattern using the calculated flow velocities in the target volume, as for the periodic pattern case.

Generally, in the non-periodical case the off-diagonal elements in the up-scaled permeability are not equal. In these cases an average value for the off-diagonal elements is used when calculating the main flow direction.

The up-scaled permeability is presented numerically as a tensor and graphically as a directional permeability plot in which the permeability in a certain direction is the length from origo (centre of box) to the surface of the imaged permeability function.

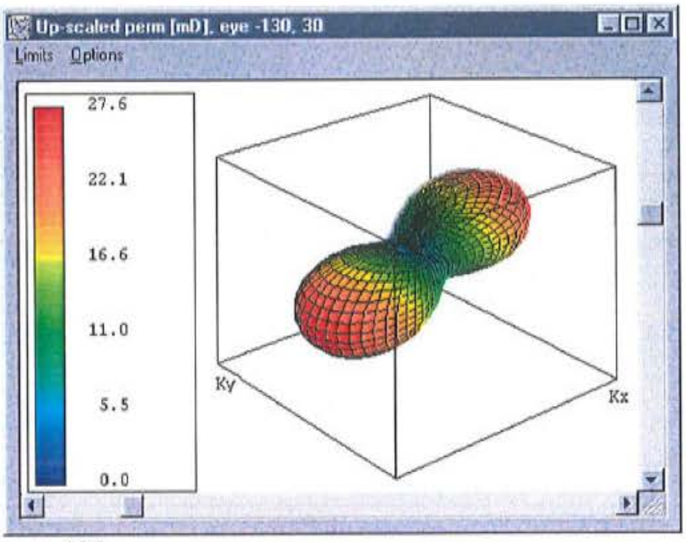

Figure 107
Imaging up-scaled permeability

The colours in Figure 107 show the magnitude of the absolute permeability

---

Matrix porosity-permeability relations

Two models for calculation of matrix permeability from matrix porosity (fraction) are implemented.

$$\text{(1) Exponential model}: K = A \cdot 10^{B \cdot \varphi} \tag{7.1}$$

$$\text{(2) Polynomial model}: K = A \cdot \varphi^{B} \tag{7.2}$$

The two models are generally used for curve fitting of porosity-permeability relations.

The two parameters, *A* and *B*, and the preferred model can be set by the user in the **FracSynt.inf** file.

The program defaults are:

Model 1: *A*=0.037, *B*=6.0
Model 2: *A*=500.0, *B*=5.0

For cases in which only the matrix porosity distribution is defined the matrix horizontal permeability is calculated from one of these models. The model and the parameters can be changed interactively by the user.

In cases where both the matrix porosity and permeability distributions are defined a best-fit A and B parameter set is calculated, and a best fit **Rel.Err**. is calculated as the relative distance between the best-fit curve and the data values:

$$\textbf{Exponential model: } d_1 = \frac{\sum_n \left| K_n - A \cdot 10^{B \cdot \varphi_n} \right|}{\sum_n K_n} \tag{7.3}$$

$$\textbf{Polynomial model: } d_2 = \frac{\sum_n \left| K_n - A \cdot \varphi_n^B \right|}{\sum_n K_n} \tag{7.4}$$

for possible quality assurance of the input data.

Air permeability to fluid permeability

A model for correction of matrix air permeability to fluid permeability is implemented.

$$K_{fluid} = C \cdot K_{air}{}^{D} \tag{8.1}$$

The two parameters, *C* and *D*, can be set by the user in the FracSynt.inf file.

The programme defaults are:

C=0.52, *D*=1.083

For cases in which the matrix air permeability distribution is defined the matrix fluid permeability is calculated automatically from equation (8.1).
The parameters can be changed interactively by the user.

FracSynt 3D Software documentation

Introduction

FracSynt 3D is a software program for calculation of up-scaled values of absolute directional permeability of fractured rock.
The program performs single-phase up-scaling from input of fracture network data, matrix permeability and matrix porosity grid block data.
The program can perform up-scaling of directional permeability and porosity to reservoir grid cell size for both single porosity of dual porosity reservoir simulation.

FracSynt 3D consist of 4 parts ,tools (see Figure 108)

1. A **FracMan file reader** for reading a FracMan file (***.fab**) [3]
2. A **Gridding** tool for calculation of fracture porosity, fracture permeability and fracture directional transmissibilities in user defined grid blocks. The result can be filed and used as input to reservoir simulation.
3. An **Up-scaling** tool for calculation of the absolute directional permeability of:
   a: the fracture pattern, (Fracture data in a dual porosity model)
   b: the matrix (Matrix data in a dual porosity model)
   c: the combined fracture pattern and matrix. (Matrix data in a single porosity model)
4. A **Viewing** tool which can be used for generating 3D-maps of grid block data, plot of up-scaled permeability, data distributions and logs.

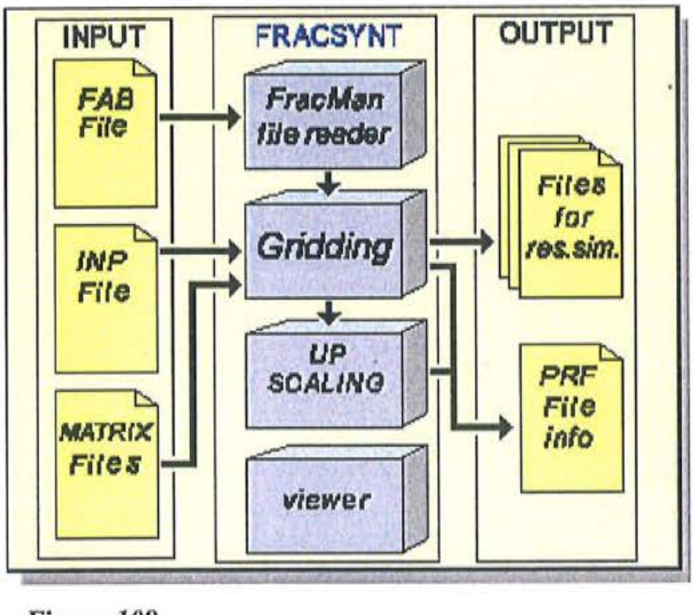

Figure 108
The program structure with input and output files.

[3] FracMan is a commercial software program from Golder Associates (UK) Ltd., which can generate 3D fracture patterns.

Input files

CaseName.fab fracture pattern file.

CaseName.inp File with grid data and matrix x-, y- and z-permeability, matrix kv/kh data and matrix porosity data. The input file may also contain paths to files with matrix data.

Output files

CaseName.prf print file. Contains information about the grid and all calculated items during the execution of FracSynt.

Fracture and matrix permeabilities, porosities and transmissibilities on the grid can be saved for input to reservoir simulation.

The present document corresponds largely to the material included in an online help system attached to FracSynt.

In the document items in square brackets [.] are optional.

FracMan file

The **FracMan file reader** reads a FracMan output fab file with a 3D fracture pattern defined as the co-ordinates to the corners of a number of 3D fracture polygons. In the fab file also the hydraulic aperture (given in microns) of each fracture polygon is given.

--- Top of File ---

```
BEGIN FORMAT
  Format = Ascii
  Scale =    100.
  No_Fractures =          2
  No_Nodes =             13
  No_Properties =         3
END format

BEGIN Properties
  Prop1  = (Real*4)         "Transmissivity"
  Prop2  = (Real*4)         "Storativity    "
  Prop3  = (Real*4)         "Frac Thickness"
END Properties

BEGIN Fracture
     1    6   1    1.000E+00    1.000E+00    50.000E+00
     1    1.649691E+01    5.403756E+01   -2.687633E+00
     2    5.794394E+01    4.584776E+01    3.249860E+01
     3    5.144702E+01    1.181019E+01    7.518623E+01
     4    3.503073E+00   -1.403756E+01    8.268763E+01
     5   -3.794394E+01   -5.847755E+00    4.750139E+01
     6   -3.144702E+01    2.818980E+01    4.813772E+00
     0    3.239312E-01   -7.631328E-01   -5.591930E-01

     2    7   2    1.000E+00    1.000E+00    75.000E+00
     1   -1.893376E+01    1.489420E+01    1.000000E+02
     2   -6.382171E+01    1.290986E+00    7.326132E+01
     3   -6.485494E+01    3.376302E+00    7.324213E+00
     4   -1.103325E+01    2.208531E+01   -2.593712E+01
     5    4.382170E+01    3.870901E+01    6.738660E+00
     6    4.485495E+01    3.662370E+01    7.267577E+01
     7    6.403685E-01    2.125423E+01    1.000000E+02
     0    3.088289E-01   -9.504771E-01   -3.489899E-02
END  Fracture
```

--- End of File ---

Figure 109

FracMan file example defining two fractures of 50 and 75 microns, respectively

Note

The hydraulic aperture for the individual fracture must be specified in microns in the FracMan fab file (red numbers in example, Figure 109).
The reservoir volume considered is given as the scale parameter (blue number in example).
The volume covered in the example is

X: from -100m to 100m,
Y: from -100m to 100m,
Z: from -100m to 100m

INPUT FILE

Input data for **FracSynt** contain grid information, for the **Gridding** tool. The input file format is based on a keyword concept.
Keywords are preceded by a * (asterisks) and only one keyword is allowed per record.
Lower and upper case characters are allowed.
Records without keywords and data after column 255 are ignored.

```
--- Top of File ---
   *GRID-X.start         -0.5
   *GRID-Y.start         -0.5
   *GRID-Z.start         -1850.0

   *GRID-X.dim           20*0.05
   *GRID-Y.dim           50*0.02
   *GRID-Z.dim           50*0.02

   *MATRIX.X-PERM.FILE   c:\FracSynt\Core\Matr.dat 3
--- End of File ---
```

Figure 110
Input file example with 20x50x50 grid cells. Matrix x-perm data in column 3 of file Matr.dat.

Input grid size and position in relation to the input fracture pattern
The file name of the input file must equal the file name of the corresponding FracMan fab file. The grid volume size and position defined in the input file do not have to match the volume and position defined in the FracMan fab file. In cases where the grid volume does not match the fracture file volume only the relevant section of the fracture pattern are taken into account.

Format of keyword with attached data
***Keyword** [Multiplier*]data

Format of keyword with attached data file
***Keyword** Path to data file [Column number]

The path to the data file can be either the full path or a relative path from the location of the input file.

Pure matrix up-scaling
Opening the ***.inp** file pure matrix analysis are performed. No ***.fab** file are needed.

Porosity specification
Porosity may be specified as percentage or fraction data. Percentage data are identified and automatically converted into fraction data.
(Porosity is supposed to be given as percentage data if any data value is above 0.6)

Data files
The data must be ordered in one column in which the x-index cycles faster than the y-index, which cycles faster then the z-index. The z-index counts from the top layer to the bottom layer, except for data files in GSLIB format which are automatically identified and data are read in from bottom to top.
Empty records are not allowed, but records with comments can be inserted if preceded by two minus signs "--".

```
--- Top of File ---
   -- permeability (mD)
   1.50
   1.35
   1.42
   .
   .
   .
   1.67
   -- layer 2
   0.94
   1.11
   1.05
   .
   .
   .
   0.87
--- End of File ---
```

Figure 111
Data file example

For data files with more than one data column a specific data column can be read by adding the column number after the data file path.

List of keywords

<u>1 Size of grid cells in x-direction</u>
***grid-X.dim**
Array of positive real numbers (metre) defining the grid cell x dimension size.
Max 1000.
Must not appear with keyword 4 and 7
Example: *grid-X.dim 20*0.5 10*1.0 20*0.2

<u>2 Size of grid cells in y-direction</u>
***grid-Y.dim**
Array of positive real numbers (metre) defining the grid cell x dimension size.
Max 1000.
Must not appear with keyword 5 and 8
Example: *grid-Y.dim 50*0.75

3 Size of grid cells in z-direction

***grid-Z.dim**

Array of positive real numbers (metre) defining the grid cell z dimension size.
Max 1000.
Must not appear with keyword 6 and 9
Example: *grid-Z.dim 0.75 0.75 20*0.5 0.75 1.5

4 Grid lines in x-direction

***grid-X.coo**

Array of increasing positive real numbers (metre) defining the x grid lines.
Max 1001.
Must not appear with keyword 1, 7, 10 and 13
Example: *grid-X.coo 0 1 2 3.6 6 8 10 11 15 20

5 Grid lines in y-direction

***grid-Y.coo**

Array of increasing positive real numbers (metre) defining the y grid lines.
Max 1001.
Must not appear with keyword 2, 8, 11 and 14
Example: *grid-Y.coo -5 -4 -3 -2 -1 0 1 2 3 4 5

6 Grid lines in z-direction

***grid-Z.coo**

Array of increasing positive real numbers (metre) defining the z grid lines.
Max 1001.
Must not appear with keyword 3, 9, 12 and 15
Example: *grid-Z.coo -1800 -1790 -1780 -1770

7 File with size of grid cells in x-direction

***grid-X.dim.file**

File containing column of positive real numbers (metre) defining the grid cell x dimension size.
Max 1000.
Must not appear with keyword 1, 4 and 10
Example: *grid-X.dim.file c:\FracSynt\data\x-grd.dat

8 File with size of grid cells in y-direction

***grid-Y.dim.file**

File containing column of positive real numbers (metre) defining the grid cell y dimension size.
Max 1000.
Must not appear with keyword 2, 5 and 11
Example: *grid-Y.dim.file c:\FracSynt\data\y-grd.dat

9 File with size of grid cells in z-direction

***grid-Z.dim.file**

File containing column of positive real numbers (metre) defining the grid cell z dimension size.
Max 1000.
Must not appear with keyword 3, 6 and 12
Example: *grid-Z.dim.file c:\FracSynt\data\z-grd.dat

10 File with grid lines in x-direction

***grid-X.coo.file**

File containing column of increasing positive real numbers (metre) defining the x grid lines. Max 1001.

Must not appear with keyword 1, 4, 7 and 13

Example: *grid-X.coo.file c:\FracSynt\data\x-grd.dat

11 File with grid lines in y-direction

***grid-Y.coo.file**

File containing column of increasing positive real numbers (metre) defining the y grid lines. Max 1001.

Must not appear with keyword 2, 5, 8 and 14

Example: *grid-Y.coo.file c:\FracSynt\data\y-grd.dat

12 File with grid lines in z-direction

***grid-Z.coo.file**

File containing column of increasing positive real numbers (metre) defining the z grid lines. Max 1001.

Must not appear with keyword 3, 6, 9 and 15

Example: *grid-Z.coo.file c:\FracSynt\data\z-grd.dat

13 First x-grid line position

***grid-X.start**

Real number (metre) defining the 1st x-grid line position.

Must not appear with keyword 4 and 10

Default: *grid-X.start 0

Example: *grid-X.start -10.0

14 First y-grid line position

***grid-Y.start**

Real number (metre) defining the 1st y-grid line position.

Must not appear with keyword 5 and 11

Default: *grid-Y.start 0

Example: *grid-Y.start -10.0

15 First z-grid line position

***grid-Z.start**

Real number (metre) defining the 1st z-grid line position.

Must not appear with keyword 6 and 12

Default: *grid-Z.start 0

Example: *grid-Z.start -1800.0

16 Depths to top layer

***Top.formation.depth**

Real number (metre) defining the depths to the top of each grid cell in the first(top) layer.

Must not appear with keyword 6, 12, 15 and 17

Default: *Top.formation.depth 0

Example: *Top.formation.depth 100*10 100*20 100*40

17 File with depths to top layer

***Top.formation.depth.file**

File with column of real number (metre) defining the depths to the top of each grid cell in the first (top) layer.

Must not appear with keyword 6, 12, 15 and 16

Example: *top.formation.depth.file c:\data\depths.dat

18 Active cells

***Active.cells**

Integer numbers, 0 or 1(active), defining active cells.

Max 150000.

Must not appear with keyword 19

Default: *Active.cells 1

Example: *Active.cells 100*0 300*1

19 File with active cells

***Active.cells.file**

File with a column of integer numbers (0 or 1) defining active cells.

Max 150000.

Must not appear with keyword 18

Example: *active.cells.file c:\data\deadcells.dat

20 Matrix x-permeability grid data

***Matrix.X-Perm** or ***Matrix.Fluid.X-Perm**

Array of positive real numbers (mD) defining the matrix x-permeability in each grid cell.

Max 150000

Must not appear with keyword 23, 26 and 29

Default: *Matrix.X-perm =function of porosity

Example: *Matrix.X-perm 100*2.4 300*3.5

21 Matrix y-permeability grid data

***Matrix.Y-Perm** or ***Matrix.Fluid.Y-Perm**

Array of positive real numbers (mD) defining the matrix y permeability in each grid cell.

Max 150000

Must not appear with keyword 24, 27 and 30

Default: *Matrix.Y-perm =x-perm

Example: *Matrix.Y-perm 100*2.4 300*3.5

22 Matrix z-permeability grid data

***Matrix.Z-Perm** or ***Matrix.Fluid.Z-Perm**

Array of positive real numbers (mD) defining the matrix z permeability in each grid cell.

Max 150000

Must not appear with keyword 25, 28 and 31

Default: *Matrix.Z-perm = x-perm

Example: *Matrix.Z-perm 100*0.4 300*1.5

23 File with matrix x-permeability grid data

***Matrix.X-Perm.file** or ***Matrix.Fluid.X-Perm.file**

File with a column of positive real numbers (mD) defining the matrix x permeability in each grid cell.

Must not appear with keyword 20, 26 and 29

Example: *Matrix.X-perm.file c:\data\Xprm.dat

24 File with matrix y-permeability grid data

***Matrix.Y-Perm.file** or ***Matrix.Fluid.Y-Perm.file**

File with a column of positive real numbers (mD) defining the matrix y permeability in each grid cell.

Must not appear with keyword 21, 27 and 30

Example: *Matrix.Y-perm.file c:\data\Yprm.dat

25 File with matrix z-permeability grid data

***Matrix.Z-Perm.file** or ***Matrix.Fluid.Z-Perm.file**

File with a column of positive real numbers (mD) defining the matrix z permeability in each cell.

Must not appear with keyword 22, 28 and 31

Example: *Matrix.Z-perm.file c:\data\Zprm.dat

26 Matrix air x-permeability grid data

***Matrix.Air.X-Perm**

Array of positive real numbers (mD) defining the matrix air x-permeability in each grid cell.

Max 150000

The air permeability will automatically be transformed to fluid permeability.

Must not appear with keyword 20, 23 and 29

Example: *Matrix.Air.X-perm 100*2.9 300*4.8

27 Matrix air y-permeability grid data

***Matrix.Air.Y-Perm**

Array of positive real numbers (mD) defining the matrix air y-permeability in each grid cell.

Max 150000

The air permeability will automatically be transformed to fluid permeability.

Must not appear with keyword 21, 24 and 30

Default: *Matrix.Air.Y-perm = x-air-perm

Example: *Matrix.Air.Y-perm 100*2.9 300*4.8

28 Matrix air z-permeability grid data

***Matrix.Air.Z-Perm**

Array of positive real numbers (mD) defining the matrix air y-permeability in each grid cell.

Max 150000

The air permeability will automatically be transformed to fluid permeability.

Must not appear with keyword 22, 25 and 31

Default: *Matrix.Air.Z-perm = x-air-perm

Example: *Matrix.Air.Z-perm 100*2.9 300*4.8

29 File with matrix air x-permeability grid data

***Matrix.Air.X-Perm.file**

File with column of real numbers (mD) defining the matrix air x permeability in each grid cell.

The air permeability will automatically be transformed to fluid permeability.

Must not appear with keyword 20, 23 and 26

Example: *Matrix.Air.X-perm.file c:\data\xairperm.dat

30 File with matrix air y-permeability grid data

***Matrix.Air.Y-Perm.file**

File with column of real numbers (mD) defining the matrix air y permeability in each grid cell.
The air permeability will automatically be transformed to fluid permeability.
Must not appear with keyword 21, 24 and 27
Example: *Matrix.Air.Y-perm.file c:\data\yairperm.dat

31 File with matrix air z-permeability grid data

***Matrix.Air.Z-Perm.file**

File with column of real numbers (mD) defining the matrix air z permeability in each grid cell.
The gas permeability will automatically be transformed into fluid permeability.
Must not appear with keyword 22, 25 and 28
Example: *Matrix.Air.Z-perm.file c:\data\zairperm.dat

32 Matrix porosity grid data

***Matrix.Poro**

Array of positive real numbers (% or fraction) defining the matrix porosity in each grid cell.
Max 150000
Must not appear with keyword 33
Default: *Matrix.Poro 30%
Example: *Matrix.Poro 100*20 200*30 100*33

33 File with matrix porosity grid data

***Matrix.Poro.file**

File with column of real numbers (% or fraction) defining the matrix porosity in each grid cell.
Must not appear with keyword 32
Example: *Matrix.Poro.file c:\data\poro.dat

Info file

The info file contains values for customising FracSynt.
The **FracSynt.inf** file must be located in the directory holding the executable (FracSynt.exe).
Below is shown an example of an FracSynt.inf file.

```
--- Top of File ---
 [Opening Directory]
 C:\FracSynt\Cases\Geus\
 [Opening File Type]
 inp
 [Color Scale]
 Rainbow
 [Main Window Position]
 25 2
 [Matrix Poro-Perm Model]
 2
 [Matrix Poro-Perm Parms AB]
 500.0  5.0
 [Air to Fluid Parms CD]
 0.52 1.083
 [Graphs 3D Effect]
 On
 [Graphs Pixel size]
 350
 [Company Logo]
 COWI
--- End of File ---
```

FracSynt.inf file example.

In case the FracSynt.inf file does not exist a default file will be created automatically at the first time FracSynt is executed.

List of customising values

[Opening Directory]

Directory — The last opened input case directory (updated automatically)

[Opening File Type]

FileType — The last opened input file type: fab or inp (updated automatically)

[Color Scale]

Type — Preferred colour scale (Rainbow or Standard. Default: **Standard**)

[Main Window Position]

Hpixel — Screen horizontal position of main window (updated automatically)

Vpixel — Screen vertical position of main window (updated automatically)

[Matrix Poro-Perm Model]

Model — The model used for porosity permeability relation. (Exponential model: 1, Polynomial model: 2. Default: **1**)

[Matrix Poro-Perm Parms AB]

A	Parameter in porosity permeability relation (Default: **0.037**)
B	Parameter in porosity permeability relation (Default: **6.0**)

[Air to Fluid parms CD]

C	Parameter in air to fluid permeability conversion (Default: **0.52**)
D	Parameter in air to fluid permeability conversion (Default: **1.083**)

[Graphics Annotations]

Annotate	Flag for 3-D effects in graphs (On or Off. Default: **On**)

[Graphs Pixel Size]

Width	The size of graph windows in pixels (min: 275, max: screen vertical pixels-200. Default: **300**)

[Company Logo]

Company	String that will appear in all output windows (Max: 12 characters. Default: **COWI**)

Win95/NT implementation

A shortcut to the **FracSynt.exe** file may be placed on the desktop.

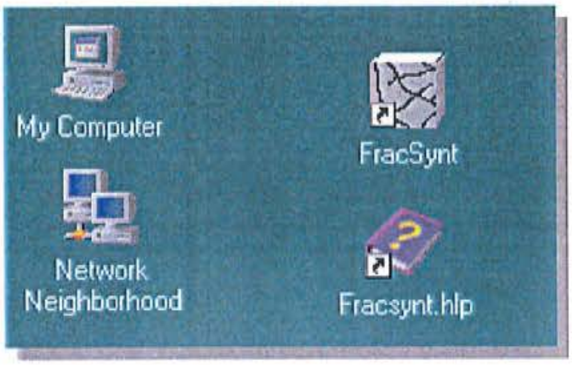

Figure 112
Desktop example with shortcuts to FracSynt programme and FracSynt online help.

Direct access to the help system can be obtained by placing an additional shortcut on the desktop to the file **FracSynt.hlp**.
The program is started by double clicking the FracSynt icon.

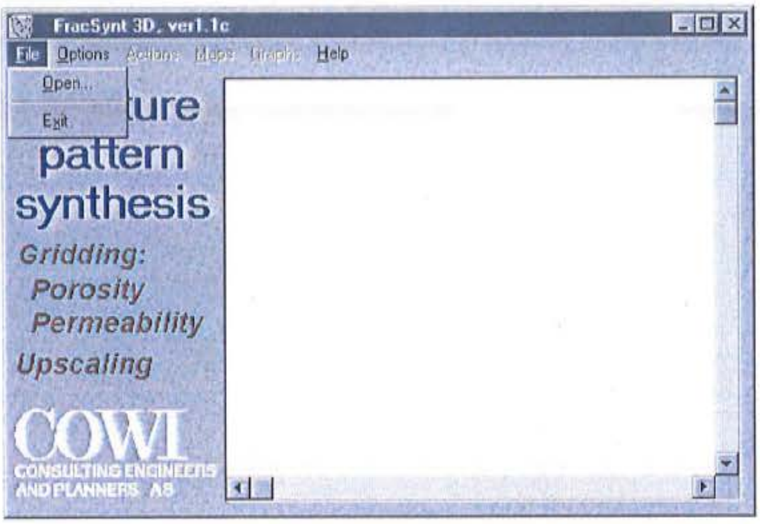

Figure 113
Main window with menu and message field.

The white message field in Figure 5.2 is used for displaying user instructions, computational information and error messages during execution.

Some of the menu items at the top of the main window will be inactive (greyed). The menu items become active during the up-scaling procedure dependant on the actual stage in the procedure.

System requirements

The hardware and operating system requirements for running FracSynt are listed below.

Processor:	Pentium (or similar)
OS:	Windows95 or NT 4.0
RAM:	Minimum 64 Mbytes
Screen resolution:	Minimum 1024 x 768 with 16 bits/pixel
Hard disk:	8 Mbytes free space

Open case

Choosing a 3D FracMan (*.fab) file containing fracture geometry and aperture through mouse selection of menu item: **[File] [Open...]** starts the fracture synthesis.

After selection of [**Open...**] a file selection box pups up.

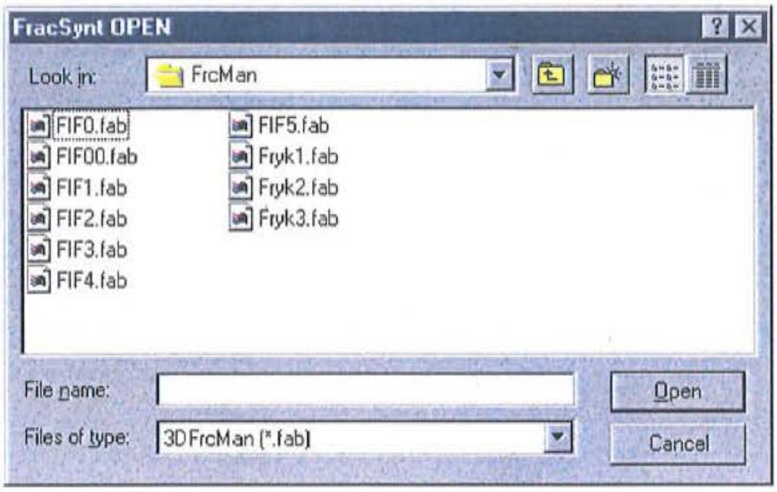

Figure 114
File selection box.

In Figure 5.3 the FracMan 3D fracture pattern file **Fryk3.fab** may be selected with the mouse or typed in **File name:**
Press the [**Open**] button and FracSynt is ready for Gridding under menu item [**Actions**].

NOTE:
A pure matrix analysis is started by choosing "Input" in the field [**Files of type:**] and opening an *.inp file.
Alternatively, files may be opened by simply dragging and dropping them into the application.

How to Exit

FracSynt is closed by selecting [**File**] [**Exit**] or pressing the cross in the upper right corner of the main window with the mouse.

Graphics

Menu item [Maps]

Plots of 3D-fracture and matrix grid cell data are presented in separate windows that can be resized.

After gridding is finished the fracture pattern can be inspected by selecting **[Maps][Fracture][Porosity]** or **[Maps][Fracture][Permeability]**

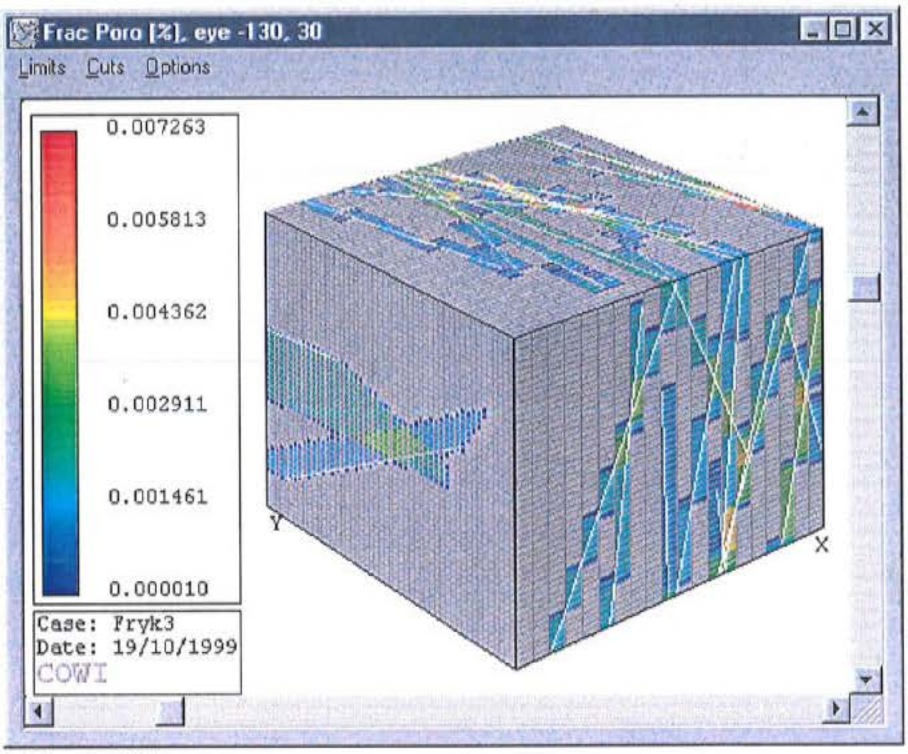

Figure 115
3D plot of fracture porosity. Grey cells are cells, which are not intersected by fractures.

The menu at the top of the window are for setting co-ordinate and data Limits, Cutting into the data volume and Options for switching the grid on/off and displaying the fracture pattern.

The spatial distribution of the matrix porosity and permeability can be inspected by selecting **[Maps][Matrix][Porosity]** or **[Maps][Matrix][Permeability]**

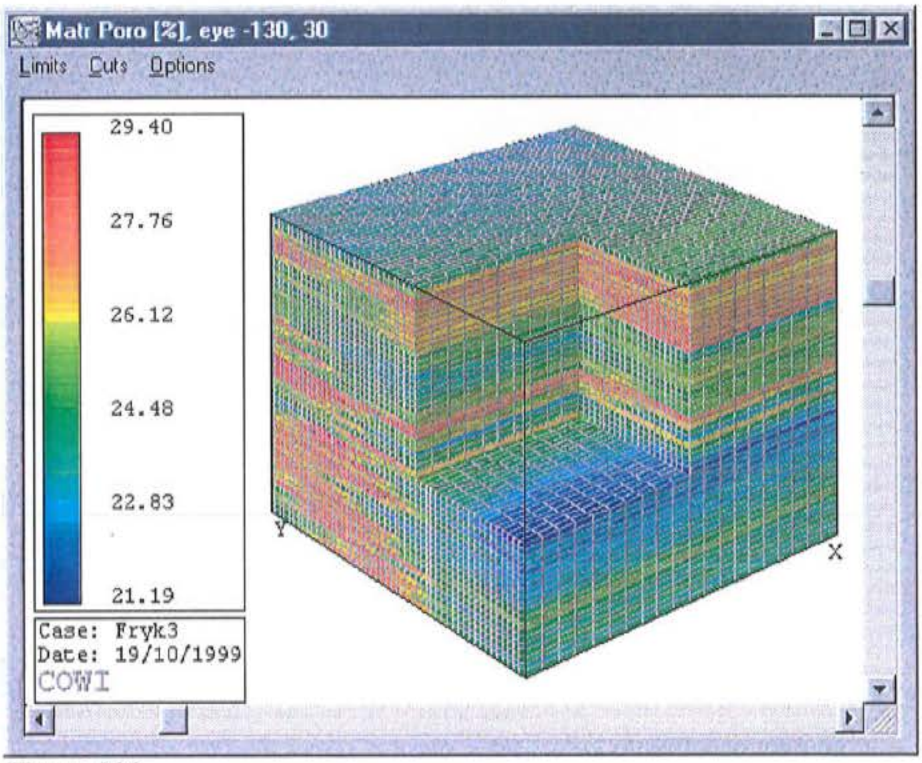

Figure 116
3D plot of matrix porosity.

Menu item [Graph]
The frequency distribution of the fracture porosity or the fracture permeability can be displayed by selecting:**[Graph][Fracture] [Porosity]** or **[Graph][Fracture][Permeability]**

The frequency distribution of the matrix porosity or the matrix permeability can be displayed by selecting: **[Graph][Matrix] [Porosity]** or **[Graph][Matrix][Permeability]**

Image logs or logs of matrix porosity and permeability can be inspected by selecting **[Graph] [Fracture][Image Log] , [Graph][Matrix] [Poro Log] , or [Graph][Matrix] [Perm Log**

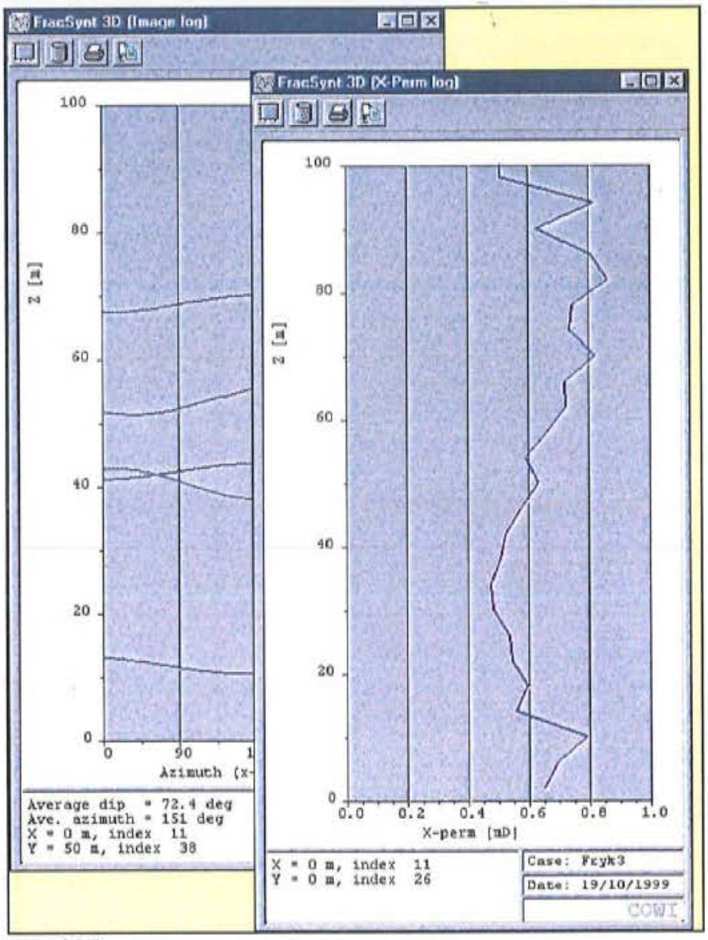

Figure 117
Synthetic image log and porosity log.

The buttons at the top of the windows are for setting the axes, defining well parameters, printing and copying to the clipboard.

Results from up-scaling

The up-scaled permeability is presented graphically as a directional permeability plot in which the permeability in a certain direction is the length from origo (centre of box) to the surface of the imaged permeability function.

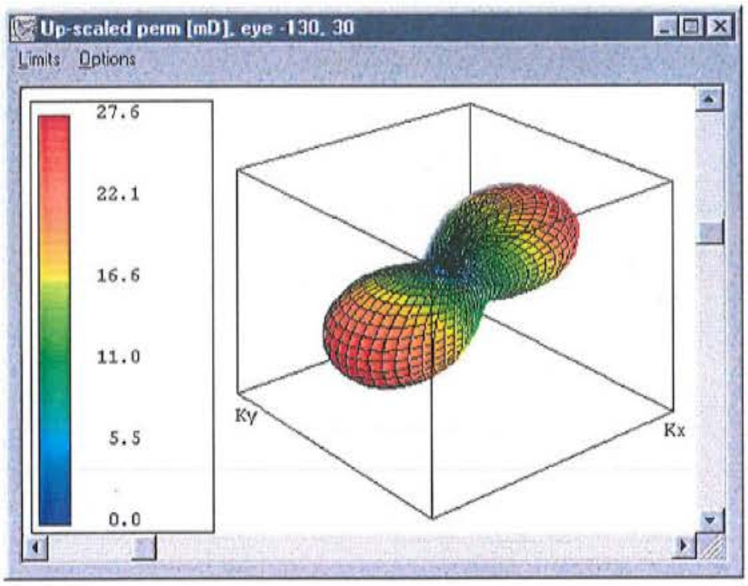

Figure 118
Directional permeability. The colours show the magnitude of the absolute permeability (Red: High, Blue: Low).

All nine directional permeabilities are determined from flow calculations in the x-, y- and z-directions and the permeabilities are also presented as a tensor (eq. 6.1):

$$\mathbf{K} = \begin{bmatrix} Kxx & Kxy & Kxz \\ Kyx & Kyy & Kyz \\ Kzx & Kzy & Kzz \end{bmatrix} \tag{6.1}$$

In cases where the off-diagonal permeabilities are zero, the flow directions will be parallel to the grid axes. In cases in which the off-diagonal permeabilities are non-zero the dominant flow direction will differ from the direction of the grid axes. In the latter case the angles between the grid axes and the dominant flow direction will be calculated and can be used for evaluation of reservoir simulation grid orientation effects.

Upscaling demonstration on large reservoir model block

Peter Frykman, Kim Zinck-Jørgensen, Finn Jakobsen (GEUS)
Flemming If (COWI)

CHARACTERISATION AND MULTISTEP UPSCALING OF FRACTURED CHALK RESERVOIRS.

JCR Phase V, Project no. 3

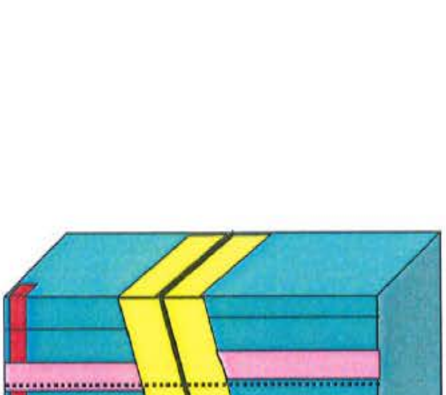

Objective of the demonstration

The objective is to demonstrate the full procedure of:

1. generation of matrix model,
2. generation of fracture models,
3. upscaling in the first step,
4. combination of building blocks of matrix for the second step model,
5. merging with large-scale fracture model, and
6. upscaling of second step.

The demonstration is carried out by using real data from the Kraka Field imported into a conceptual model with dimensions as a typical reservoir simulation cell.

Data

The available data are derived from two wells in the Kraka Field, a vertical well (deviated) and a horizontal well. They both penetrate the Danian units D1 and D2 in the oil zone, and sections from these units are selected in the same stratigraphic interval according to the biostratigraphic analyses from the wells. These two sections from the two wells are more than 1 km apart, but are artificially merged into the same volume reflecting the size of a grid block of 50 m length and width and with a total thickness of 20 m.
Data from conventional logging is available from the wells, as well as FMI logs and interpretations giving information on the fracture distribution and orientation in these selected sections.

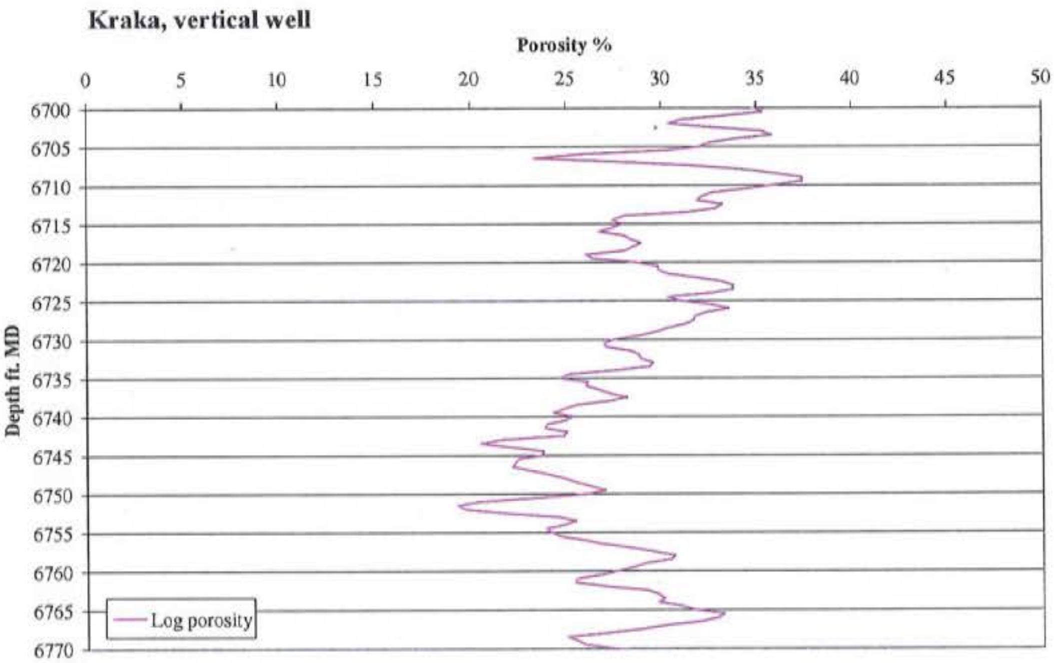

Figure 119
Porosity interpreted from log data in the vertical well in the Kraka Field

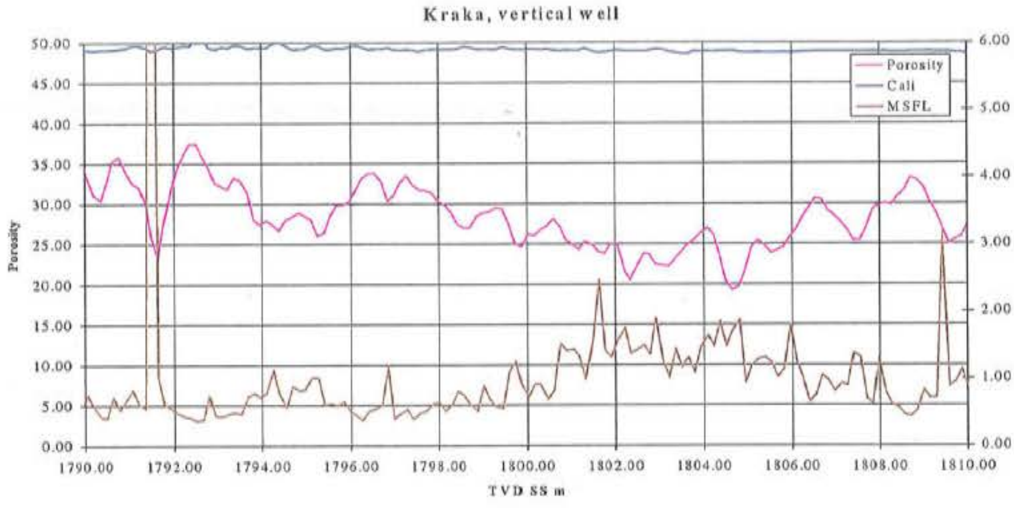

Figure 120
Same section as fig.119 with the porosity log and a resistivity log (MFSL) that is used to show indications of flint occurrences.

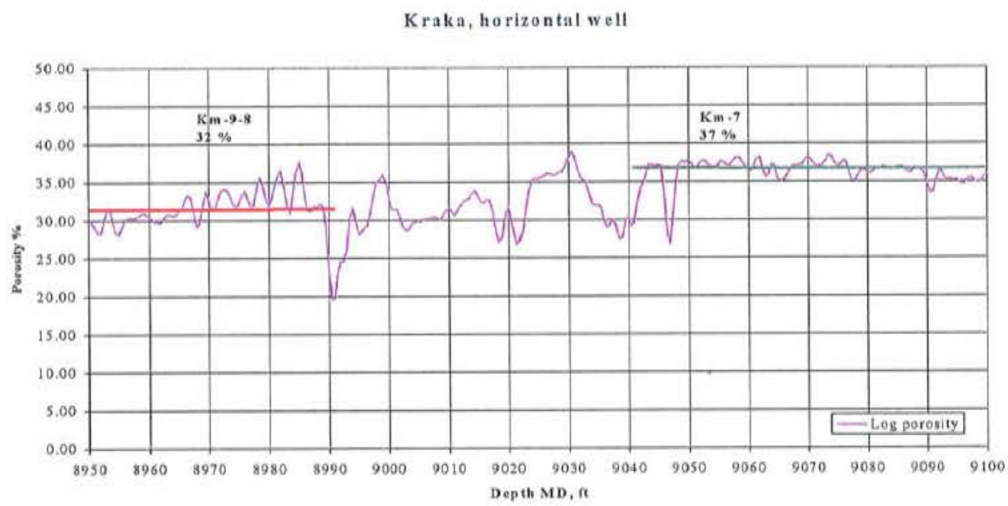

Figure 121
Porosity log from the horizontal well in the Kraka Field. The porosity level is seen to be different for the two different biostratigraphic zones present in the well, separated by a minor fault that is identified from the change in the biozonation.

In order to have the fine-scale porosity and permeability variations available for the upscaling procedure, a geostatistical simulation of those two parameters is carried out. The basic input is the log porosity data forming a soft data set that is guiding the simulation of the synthetic core porosity. From the histogram and the variogram of the log porosity, a rescaled target histogram with higher variance is produced to be used in the simulation. The variogram is also rescaled to a shorter correlation length according to the scaling laws for volume-variance relations.

The porosity simulation produces a "core" porosity model (Fig. 122), where the values deviate from the log porosity, although it is questionable how much deviation is realistic in this sequence.

The simulation of the "core" permeability model is carried out in a similar fashion, using the previous core porosity model as soft data, and an estimated permeability target histogram derived from the bivariate relation between porosity and permeability as found in other core plug data from the D1 and D2 units. The permeability model is showing layering according to the porosity level, and a fair contrast in permeability in the different layers.

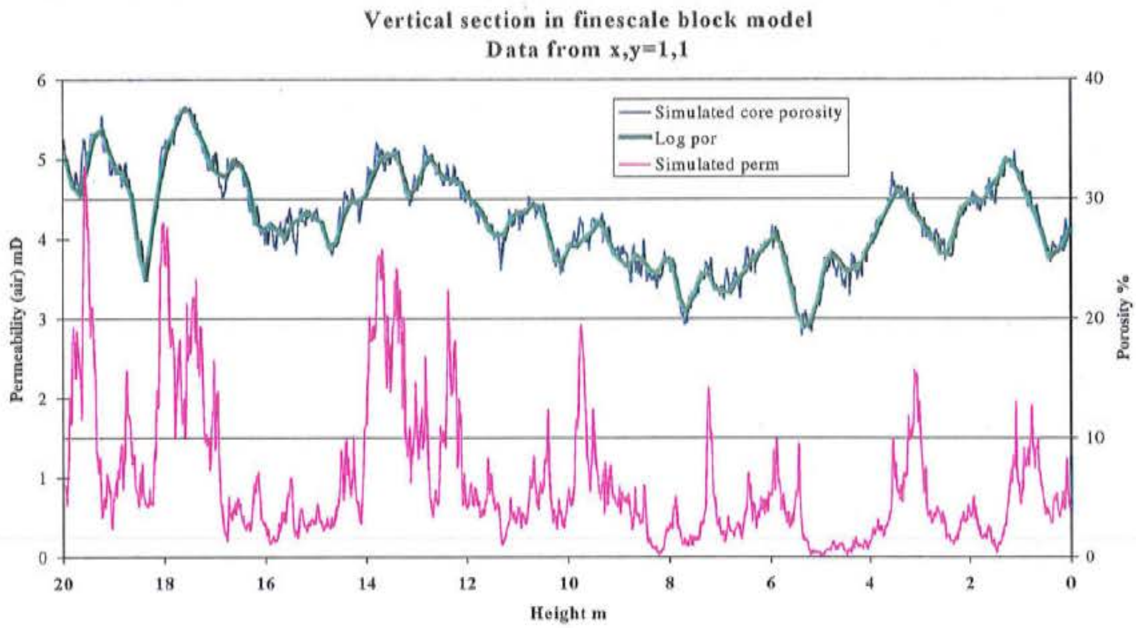

Figure 122
Simulated porosity and permeability at 2 cm scale for the Kraka V well model. The graph shows the data in one single line through the 20 m high 3D model at x,y=1,1. The simulated core porosity from this specific realisation is seen to follow the log porosity curve with only minor deviations, that might be too small for reflecting the actually present higher variability in the core scale porosity. Other simulations with changed parameters can provide additional variability.

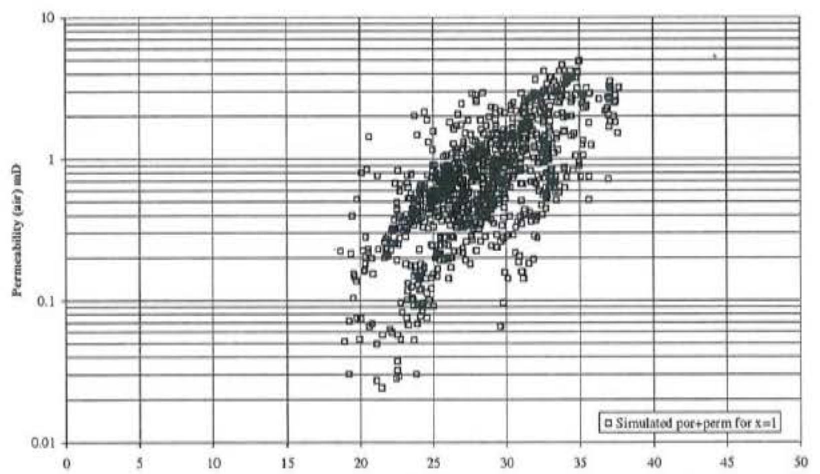

Figure 123
Porosity/permeability relation for the model after simulation of the permeability.

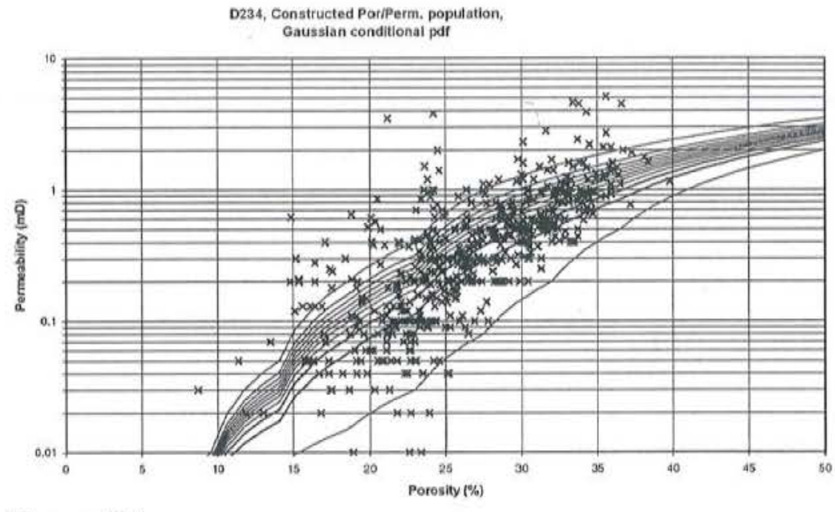

Figure 124
Porosity/permeability relation for the D2 unit in the Dan Field used as an analogue for the Kraka unit.

Flint layer occurrence

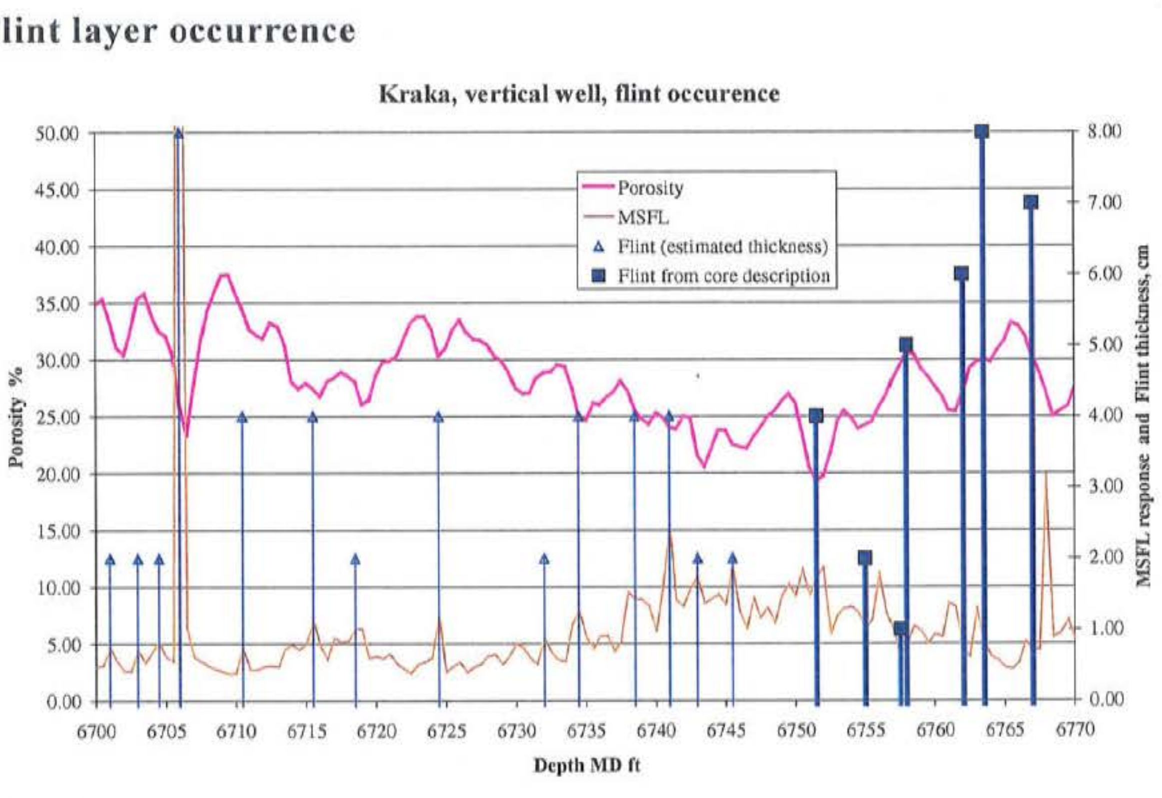

Figure125
The MSFL log response is used to interpret the occurrence of flint layers in the section investigated. The limited amount of information from the core description shown in heavy lines is used as a guideline to extrapolate the occurrence and the thickness of the individual flint layers in the non-cored sequence. This information could probably be further refined with additional analysis of the wireline log data.

Conceptual model of the grid block size scale

In order to evaluate the effect of small scale heterogeneities in a larger volume, a conceptual model is constructed, in which the main features are imported.

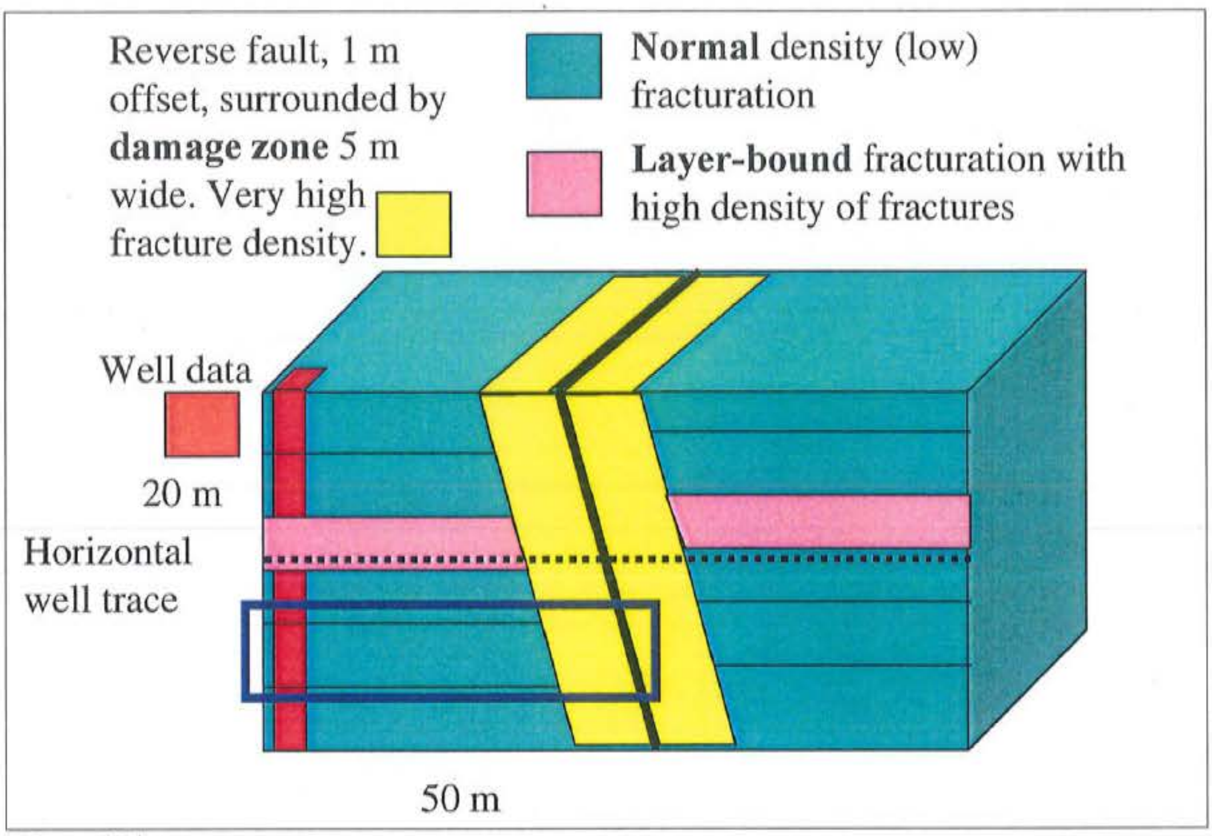

Figure 126
The blue frame shows the 50x50 m and ca. 5 m thick volume that is undergoing upscaling.

Fracture characterisation

Introduction.

The present fracture study on selected intervals from the subvertical pilot well Kraka V and the horizontal well Kraka H, is mainly based on the fracture mapping and analysis of FMI well image logs presented in a service report prepared by Z&S Geologi a.s. (now Baker Atlas Geoscience) for Mærsk Olie & Gas A.S. Additional information is gained from the Final Well Report and a Kraka Field Development Review by Mærsk Olie og Gas A.S. The wells have been chosen in collaboration with Mærsk Olie & Gas A.S., who also provided the Z&S fracture study. Available core material from Kraka V has been inspected with respect to a calibration of the log derived fracture data. Only the lower part of the selected Danian interval from 6710' to 6770' has been cored. Moreover, the core recovery is down to 36.6%, and the core data do therefore not allow for a proper quantitative calibration of the log derived fracture data. This study is concerned with fractures and faults that are open for fluid flow, i.e. the conductive fracture anomalies on the FMI image logs. Hereafter, if nothing else is stated, the term "fracture" only applies to open fractures and faults.

Selection of studied intervals.

Two intervals in Kraka V and H have been selected for fracture characterisation and forward fracture modelling, namely the intervals 6710-6770 feet MD of Kraka V and 8950-9100 feet MD of Kraka H. Both intervals are located in the Danian reservoir section in the micropalaeontological zones KM6B to KM14 and KM7 to KM9-8, respectively (figs 127 and 128). A further selection criteria has been applied for the Kraka H well, so that the selected horizontal section exhibits a marked shift in the overall fracture density (fig. 128). According to Z&S Geologi both intervals exhibit good to very good image log quality, and the image log interpretations of the intervals are not believed to be biased by the cherty intervals, as commonly seen elsewhere in the Kraka field. Thus, the fracture data presented in the Z&S report have not been corrected for a possible influence of cherty intervals, nor have the data been corrected for possible drilling induced fractures.

Density distribution of open fractures

Kraka V, 6710-6770 feet MD (fig. 127).

The density distribution of open fractures, as given from the Z&S image log interpretation of conductive fracture and fault events, is shown on fig. 127. The fracture densities are generally low, varying from 0.8 m^2/m^3 to 1.4 m^2/m^3, with the highest densities recorded in the bio-zones KM6B-7 and the lowest densities in KM8-9. The low fracture densities are in fairly good agreement with the core observations, although the cores contained a number of subvertical open fractures that were oriented parallel to the core, and therefore believed to be poorly represented on the image log, due to the "blind angle" phenomena (fig. 129). The Schmidt net plot of poles to fracture planes (Z&S report, and fig. 129 in this report) confirms that no fractures in the blind angle area (108°/18°) have been interpreted. Fractures with this orientation are very frequent in the horizontal section of Kraka H, and it is therefore very likely that the image-log derived fracture densities of Kraka V are relatively too low.
Although both the core- and log-derived fracture densities are low, there is no obvious mach between the two density distributions. The uppermost 8 feet of the core, down to 6757 feet MD, is almost void of fractures. Hereafter, the fracture frequency increases somewhat in the interval down to 6769 feet MD. The remaining three feet of the recovered core is rubble, but many slickensided fracture surfaces on core pieces indicate fairly high fracture frequencies for this interval. This apparent increase in fracture density in the lower part of the vertical section, though, is not reflected on the log-derived density distribution, where a minor increase in fracture density from 6750 to 6760 feet MD is succeeded by a minor decrease going from 6760 to 6770 feet MD.

Kraka H, 8950-9100 feet MD (fig. 128).

The density distribution of open fractures, as given from the Z&S image log interpretation of conductive fracture and fault events, is shown on fig. 128. In contrast to the Kraka V section, the horizontal section of Kraka H exhibit highly variable fracture densities – from below 1 m^2/m^3 in the interval 8950-9010 feet MD (biozones KM9-8) to up to 4 m^2/m^3 in the interval 9010-9100 feet MD (biozone KM7). The most pronounced shift in fracture density appears to be related to a fault controlled boundary at 9000 feet MD between the bio-zones KM9-8 and KM7, with the higher densities in KM7. In Kraka V the biozone KM7 also showed higher fracture densities than the biozones KM8-9. It is therefore possible that the observed fracture density variations in Kraka H are, at least partly, controlled by different mechanical properties of the chalks in biozone KM7 and in KM8-9. The cause of these possible different mechanical properties, though, is not quite obvious. The relationship of decreasing porosity with increasing fracture density, that is generally accepted for North Sea chalk reservoirs, does not seem to apply for selected intervals at this scale of investigation. On the contrary, for both well sections the biozone KM7 displays the highest porosities as well as the highest fracture densities, when compared to the biozones KM8-9.
The two faults marked on fig. 128 (at 9000 and 9100 feet MD) are both based on the Z&S image log interpretation. It is striking that both faults appear to be located in sections with very low fracture densities compared to the neighbouring sections. Faults are usually

accompanied by zones of more intense fracturing adjacent to the faults, also called "damage zones". The fracture densities should therefore increase, and not decrease in the vicinity of the two faults. A likely explanation of this apparent decrease in fracture densities in the vicinity of the faults, is that the fracture densities of the damage zones are too high for individual fractures to be resolved by the FMI image log. Consequently, with respect to the forward fracture modelling, it is proposed to disregard the apparent low fracture densities, and assign high fracture densities (ca. 5 m2/m3) to the damage zones of faults with visible offset, like the one at 9000 feet MD. In a recent EU research project(Bech 1999), the scaling relationships of normal fault damage zones in analogue outcrops of fractured limestone rocks in Italy were investigated (Bech 1999). Although poorly defined, there seemed to be a positive correlation between both fault trace length / fault throw and the damage zone width. The damage zone width were suggested to be related to the fault length by L/52, and to the fault throw by a log-normal relationship. In the present study we have suggested a damage zone width of 10 m, which corresponds to a fault trace length of 520 m and a fault throw in the range 3 to 70 m. Given the total thickness of the bio-zones KM7-9 in the vertical well of approximately 30 feet, the fault throw for the fault at 9000 feet MD in the horizontal well is less than 10 m. A damage zone width of 10 m might therefore be too much for this fault.

Orientation distribution of open fractures

Based on the fracture orientation distributions presented in the Z&S report, a number of fracture sets have been defined for each of the two selected well intervals (Table 1 and fig. 129). Each fracture set is defined by a mean orientation, an orientational spread and the percentage of the total number of fractures contained in the fracture set. The fracture sets of Kraka V are less well constrained than the sets of Kraka H, because of the lower fracture densities and smaller counting window of Kraka V.

The stereonet plots of fig. 129 are based on fracture data from longer well sections than the ones chosen in this study, but on basis of a qualitative assessment of the Z&S data, it is believed that the orientation distributions of these longer sections are representative for the shorter sections of this study.

Comparisons of the fracture set orientation of the two well sections show approximately the same orientation of the most prominent fracture set of each well, namely the N striking, W dipping fractures of the sets V-1 and H-1. The less prominent ENE striking, N dipping fracture sets V-3 and H-4 also seem to belong to the same fracture population. The conjugate set to H-1 in Kraka H, the E dipping H-2 set, and the conjugate sets H-5 and H-6 are apparently absent in Kraka V. This fact, though, is believed mainly to be a "blind angle" effects, because the H-2 and H-5 fractures, if present in Kraka V, would parallel the borehole (fig. 129). Also, the core inspection confirmed the presence of fractures oriented parallel to the borehole axis. The same kind of "blind angle" effect probably accounts for the absence of NW striking fractures in Kraka H (fracture set V-2 in Kraka V). The relative small counting window of Kraka V is believed to be the cause for the apparent absence of the fracture set H-6 in Kraka V. Fractures with the same orientation are present in Kraka V, where most of them would be included in the fracture set V-1 of Kraka V. The fracture set V-4 is very poorly constrained (based on only three events), and it is proposed to disregard this set with respect to the forward fracture modelling.

Based on the evaluation above of the fracture populations and possible blind angle effects of the two well sections, it is proposed that following fracture sets should be included in the forward fracture modelling - namely H-1, H-2, V-2, H-3, H-4, H-5 and H-6.

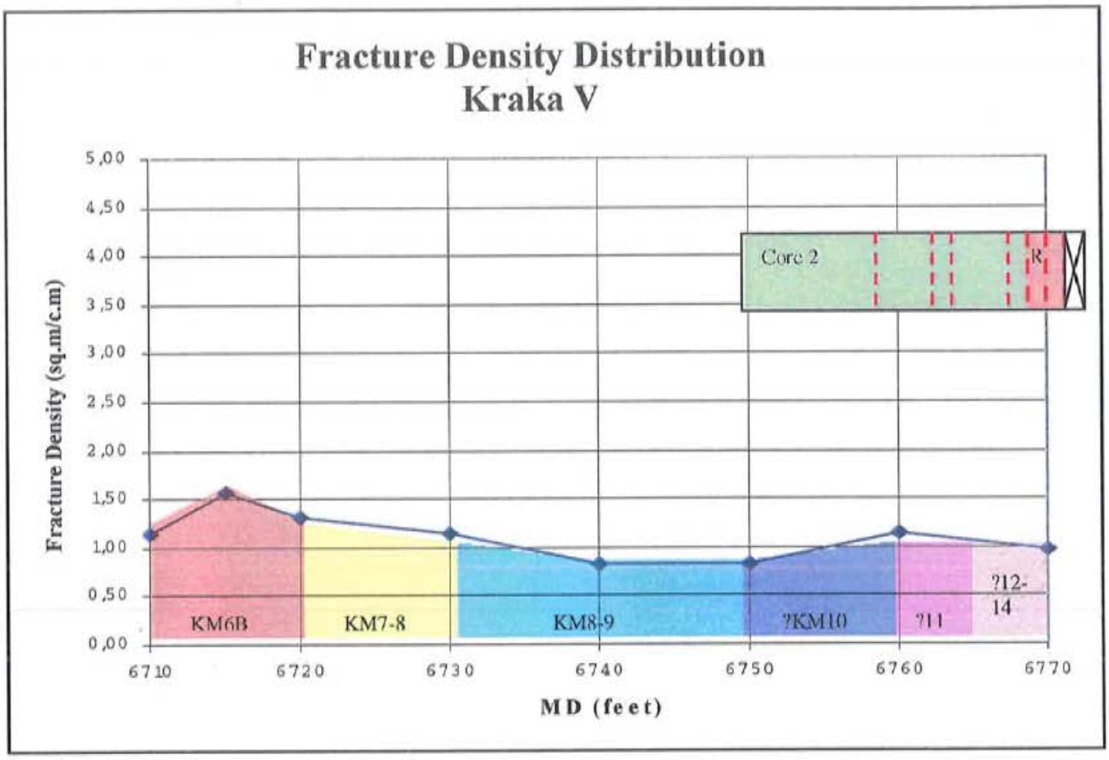

Fig. 127. *The density distribution of open fractures in Kraka V, 6710'-6770'MD, with indication of the micropalaeontological zonation. Fracture observations (dotted red lines) from available core material are shown above. Red colour/'R' indicates rubble.*

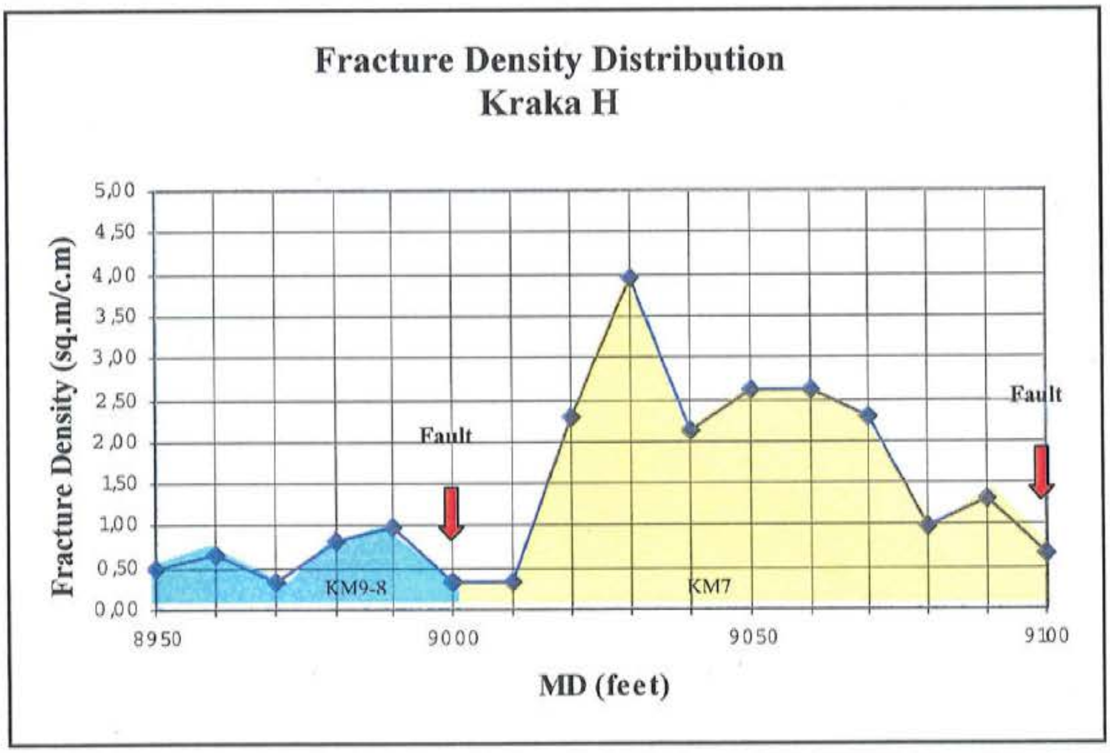

Fig. 128. *The density distribution of open fractures in Kraka H, 8950'-9100'MD, with indication of the micropalaeontological zonation.*

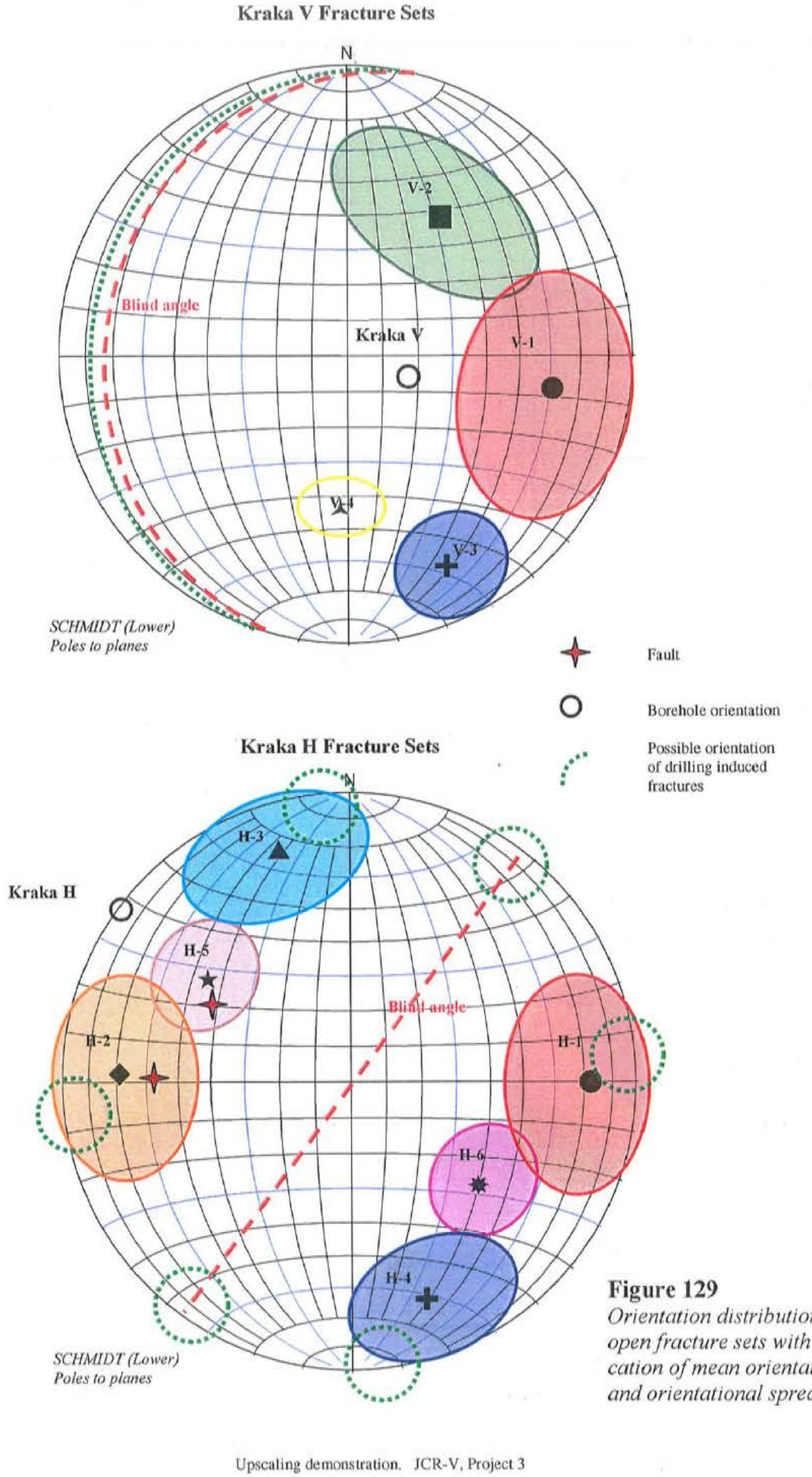

Figure 129
Orientation distribution of open fracture sets with indication of mean orientations and orientational spread.

Fracture length distribution

In addition to the fracture frequency and orientation distribution, the fracture length distribution is a critical parameter with respect to the connectivity of a given fracture network. Unfortunately, it is not possible on the well scale to obtain the fracture lengths. Core and well image log data basically only provide 1D information on faults and fractures. Previous fracture studies on North Sea chalk reservoirs have, based on analogue outcrop studies, assumed a log-normal length distribution of fractures with an average length of 3 to 5 m (Koestler & Reksten 1992). The same principle and average numbers have been applied by the present study.

Possible problems with drilling induced fractures

As this fracture study is only concerned with the natural fracture network, possible drilling induced fractures are a concern. In some chalk fields, drilling induced fractures are believed to constitute a significant proportion of the image log interpreted fracture events (Jørgensen & Petersen 1999). In vertical wells fractures parallel to the wellbore and the minimum in situ stress direction are commonly interpreted as drilling induced (Ma *et al.* 1993). In horizontal wells, vertical fractures running along the top of the borehole are considered drilling induced (Lehne & Aadnoy 1992). In addition to these commonly accepted orientations for drilling induced fractures, it has been argued that abundant drilling induced fractures in horizontal wells preferentially form as vertical shear fractures striking 45° to the wellbore (Jørgensen & Petersen 1999).

In the present fracture study, these different orientations of possible drilling induced fractures have been related to the well azimuth of Kraka V and H (fig. 129). Concerning the vertical well, drilling induced fractures would preferentially form in the blind angle to the logging tool, and consequently, there are no image-log derived fractures with this orientation. As mentioned above, sub-vertical fractures parallel to the wellbore have been observed in the core. However, none of these fractures can positively be identified as drilling induced. Regarding the horizontal well section, possible drilling induced vertical fractures, aligned parallel to the wellbore, would probably not be detected by the logging tool because of the blind angle effect. However, several of the fracture sets defined in Kraka H are oriented close to the critical 45° angle to the wellbore. Thus the fracture sets H-1 to H-4 are all striking close to the critical angle for the formation of drilling induced fractures. A proportion of the fractures from these four sets might therefore be drilling induced. Given that the fracture sets H-1 and H-4 both are well defined in Kraka V, and that the absence of the sets H-2 and H-3 in Kraka V probably is due to the blind angle effect, we feel confident that the majority of the H-1 to H-4 fractures of Kraka H are natural fractures. Consequently, we do not believe that the image-log derived fracture data applied in this study are severely biased by drilling induced fractures, that should be corrected for.

Table 1: Fracture Orientation Distribution			
Well: **Kraka-V** *Total no. of faults/fractures:* 27		*Depth int*: 6710-6770 feet MD *No. of fracture sets:* 4	
Fracture set	**Mean orientation**	*Orientational spread*	*% of all fractures*
V-1	279° / 61°	±29° / ±30°	38 %
V-2	214° / 48°	±29° / ±21°	17 %
V-3	335° / 69°	±14° / ±15°	9 %
V-4	3° / 43°	±18° / ±10°	6 %
"Rest"	None	Random / 35° - 90°	30 %
Well: **Kraka-H** *Total no. of faults/fractures:* ca. 74		*Depth int:* 8950-9100 feet MD *No. of fracture sets:* 6	
Fracture set	**Mean orientation**	*Orientational spread*	*% of all fractures*
H-1	270° / 72°	±26° / ±26°	23 %
H-2	92° / 69°	±25° / ±25°	22 %
H-3	163° / 73°	±25° / ±25°	17 %
H-4	341° / 68°	±21° / ±21°	12 %
H-5	126° / 51°	±16° / ±16°	5 %
H-6	309° / 47°	±16° / ±16°	6 %
"Rest"	None	Random / 35° - 90°	15 %

H-1 & H-2, H-3 & H-4 and H-5 & H-6 are conjugate shear sets

Fracture modelling

Fracture modelling is carried out by the use of the FracMan software on the basis of the input from the fracture characterisation. A random fracture generation has been carried out using the FracWorks package. The intention with this study is to supply models of the geometry of fracture networks. Determination of apertures or roughness coefficient has not been treated here.

Input data.

As input for the FracMan the following parameters have to be determined:

Density of fractures for each fracture set
Orientation of fracture sets (Azimuth/Dip)
Fracture length distribution

For the present models data from the vertical and the horizontal Kraka well have been used, and the 6 fracture sets of Kraka H have been applied (in this model the fracture set V-2 not seen in the horizontal well section due to the blind angle effect is not included). 3 types of models comprising different frequencies (low (0.6 m^2/m^3), high (2.0 m^2/m^3) and damage zone (5.0 m^2/m^3)) have been modelled assuming a similar representation of the fracture sets in the various intervals concerning orientation and relative density.

Dip/Azimuth plot	**Fracture set**		**H1**	**H2**	**H3**	**H4**	**H5**	**H6**
Azimuth		deg	270	92	163	341	126	309
Dip		deg	72	69	73	68	51	47
Frequency	**Low density**	m^2/m^3	**0,16**	**0,15**	**0,12**	**0,08**	**0,04**	**0,04**
	High density	m^2/m^3	**0,54**	**0,52**	**0,4**	**0,28**	**0,12**	**0,14**
	Damage zone	m^2/m^3	**1,35**	**1,24**	**1,06**	**0,71**	**0,29**	**0,35**

Table 2

The fracture radius is estimated to be 3 m with a lognormal distribution and a range of 1 m for the low and high density fracture sets, but with a radius of 1 m +/- 0.5 for the damage zone.

For the FracMan modelling the following additional options have been applied:

- Geostatistical model used for the geometric modelling
- Center of fracture used for generation of 6-sided polygons
- Degree of termination of fractures (25% in high and low density; 50 % in damage zone)

For representation of the variation in dip/azimuth as recognised from the well data has been used a Fisher dispersion of 25 for fracture set H1-H3; dispersion 30 for fracture set H4 and dispersion 50 for fracture sets H5-H6.

Output

For the illustration of the fracture distribution a box generation region is chosen (figure 130) The box sizes for visualisation are 2 x 2 x 2 m. For the modelling purposes in FracSynt a slab generation region representing a pre-defined block size is used. For illustration of the low density fractured gridblock a 50 x 50 x 5 m slab region has been generated (figure 131)

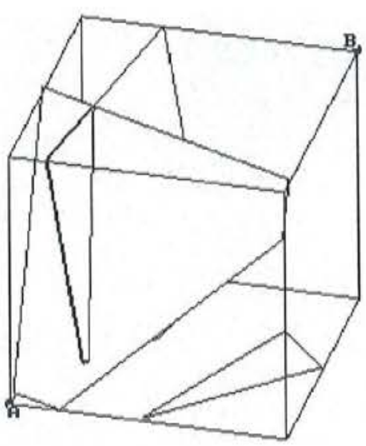

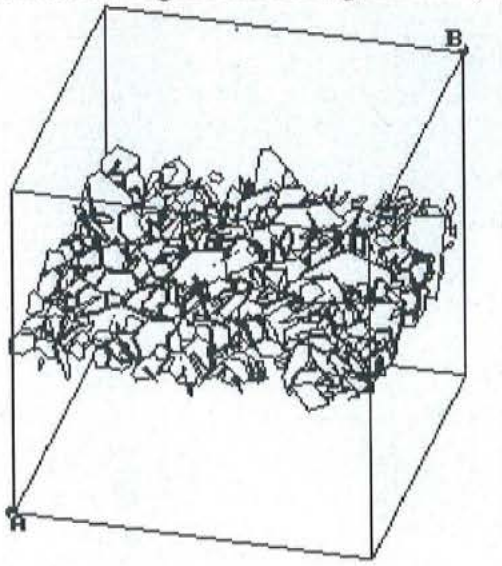

Figures 130 and 131

Fracture model in 2x2x2 m box for low frequency model and fracture model for low frequency in slab-defined box of 50x50x5 m.

The three fracture models have been replicated and merged to fill the full block model of 50x50x5 m, with the damage zone as a 5 m wide zone at the end face of the model block as shown in Fig. 132. The model of the large-scale fracture pattern with the long fractures have been produced so that some fractures traverse the full model block (Fig. 133).

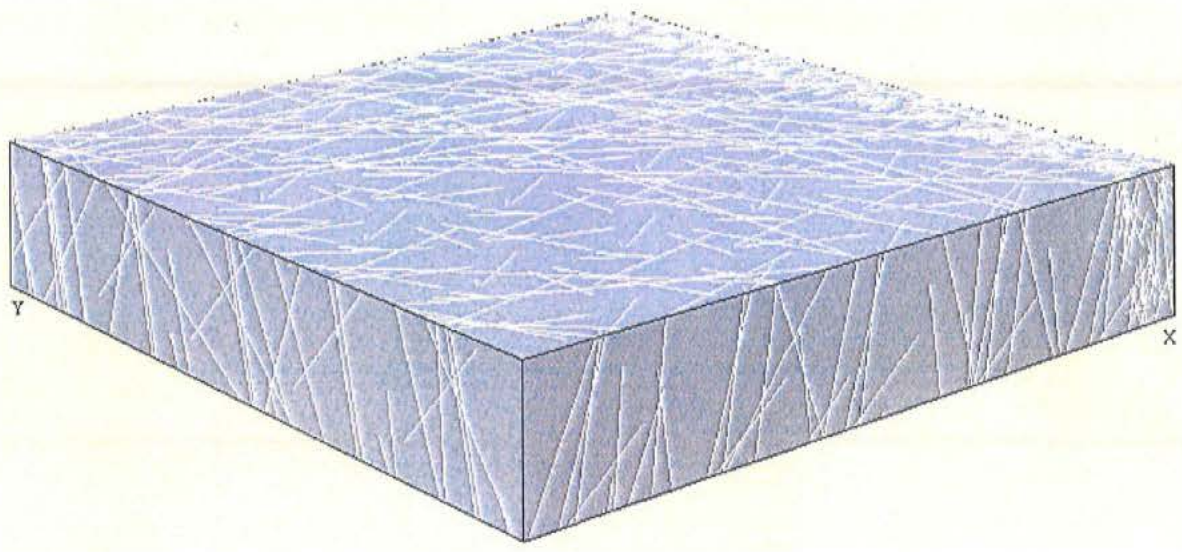

Figure 132
Block model with all three fracture models incorporated

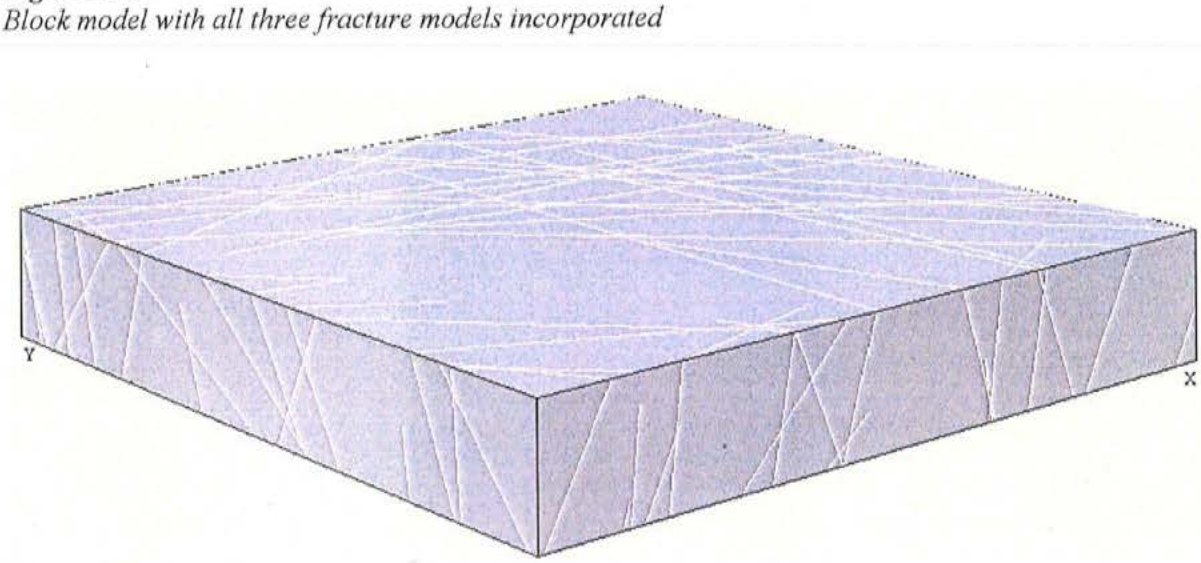

Figure 133
Extract showing the population of long fractures

UP-SCALING PROCEDURE

The aim of the up-scaling demonstration is to calculate the porosity and the effective up-scaled directional permeabilities for a grid block of size 50m x 50m x 4.62m. The grid block is located at the uppermost part of the Danian-2 formation.

The up-scaling to a reservoir grid block is based on the geostatistical data from the simulated $1 \times 1 \times 20 m^3$ column at depth 1790m to 1810m. The $20 m^3$ column is shown in Figure 134 and consists of 1.000.000 grid cells of core plug size. The original data consist of the cell position and size, and the porosity and air permeability for each grid cell. The layering presented in this model is considered to be constant for the 50x50 m grid cell, and no lateral changes in matrix properties is incorporated.

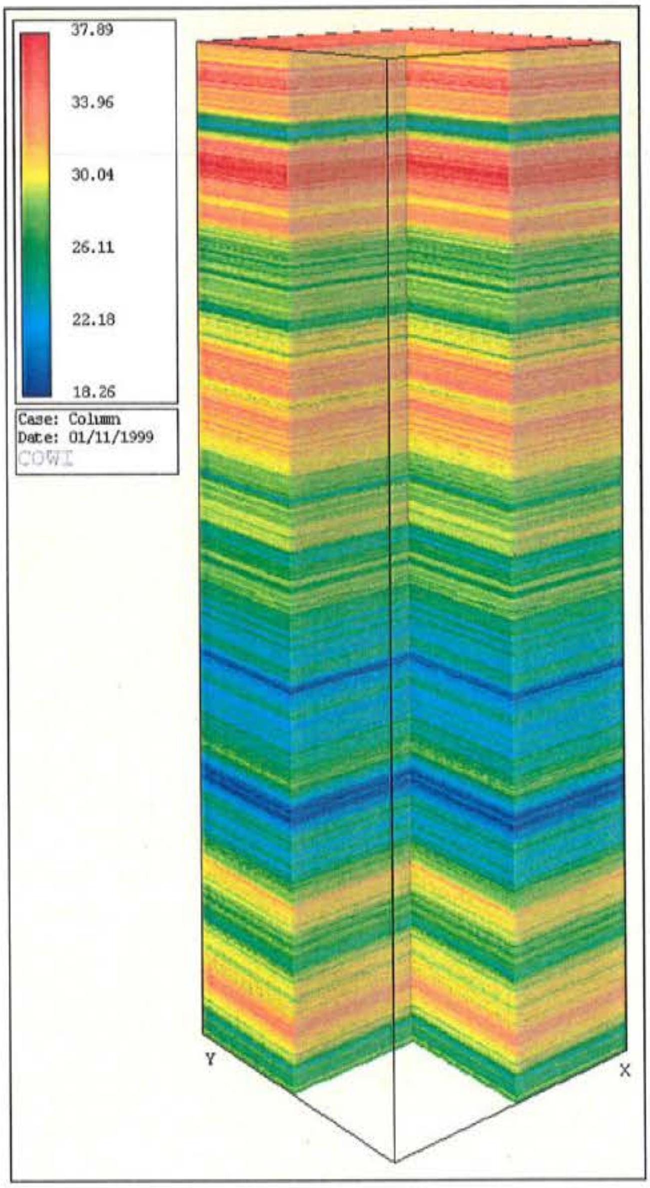

Figure 134
Porosity distribution in the 20m column. A cut is made into the centre of the column to emphasize the layering. The porosity varies from 18.26% to 37.89%.

Initially a small scale zonation of the 1.000.000 cell column into blocks of size $1m^3 \sim 2m^3$ each with $50.000 \sim 100.000$ grid cells is done in order to form input to the first up-scaling steps. Figure 135 show the small scale zonation with the calculated horizontal and vertical permeabilities in each zone. Also in Figure 135 is shown the fluid permeability and the porosity log along the centre of the 20 m column.

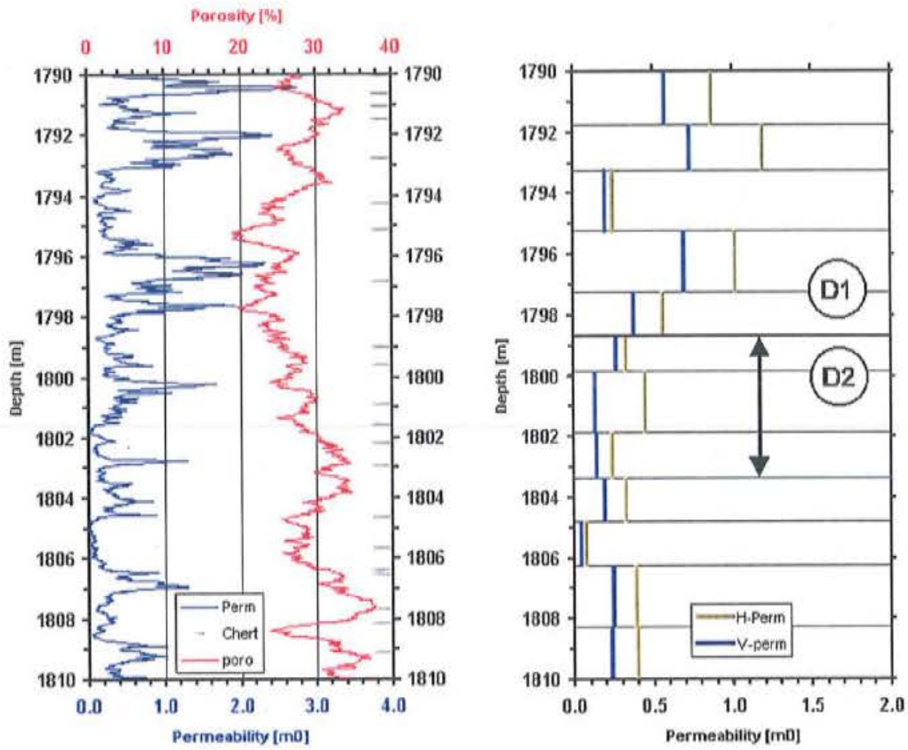

Figure 135

Porosity and permeability log at centre of column (left). Small scale zonation and up-scaled horizontal and vertical permeability in each zone (right).

The fluid permeability are calculated from the air permeability data using the transformation:

$$k_{fluid} = 0.52 \cdot k_{air}^{1.083} \qquad (1)$$

In Figure 135 the target up-scaling zone is indicated with an arrow at depth from 1798.7m to 1803.38m at the top of the Danian 2 formation. The up-scaling target zone consists of three small-scale zones, named Block06, Block07 and Block08. These blocks are up-scaled individually.

The thickness of the chert layers shown in Figure 135 varies from 2cm to 4cm. The chert layers are modelled by randomly distributing zero porosity/permeability cells in one or two layers in the matrix model at the given depths. The 2cm chert layers are supposed to cover 40% of the layer while the thick 4cm chert layers are supposed to cover 70% of the layer. As no fine scale fracturing exists only the matrix core plug data and chert layer positions are used in the first up-scaling steps.

Upscaling upper block (Block06)

Block size 1m x 1m x 1.16m from depth 1798.7m to 1799.86m. Two chert layers are present in the block at depths 1799.0m and 1799.58m with thickness 2cm and 4cm, respectively.

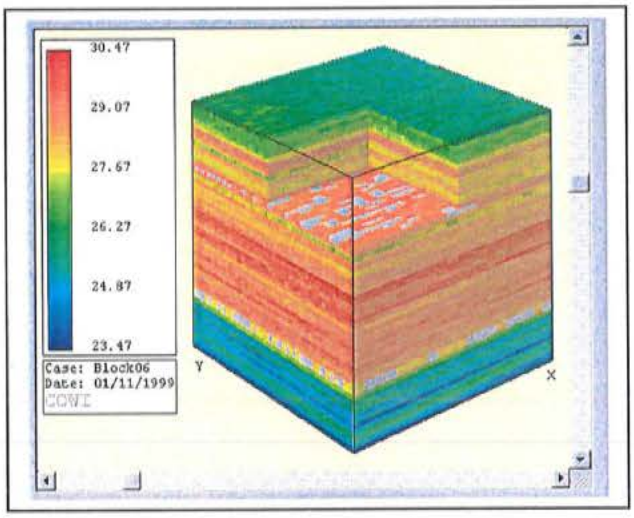

Figure 136
Porosity distribution in the upper block. A cut is made into the block to show one of the chert layers.

The up-scaled permeability tensor is purely diagonal with equal x- and y-permeability:

$$\mathbf{k} = \begin{bmatrix} \mathbf{0.32} & \mathbf{0.00} & \mathbf{0.00} \\ \mathbf{0.00} & \mathbf{0.32} & \mathbf{0.00} \\ \mathbf{0.00} & \mathbf{0.00} & \mathbf{0.26} \end{bmatrix} \mathbf{mD} \tag{2}$$

which for this block results in an effective anisotropy $k_V/k_H = 0.81$

The up-scaled porosity is **27.9%**

Upscaling middle block (Block07)

Block size 1m x 1m x 1.98m from depth 1799.86m to 1801.84m. Two 4cm thick chert layers are present in the block at depths 1800.88m and 1801.60m.

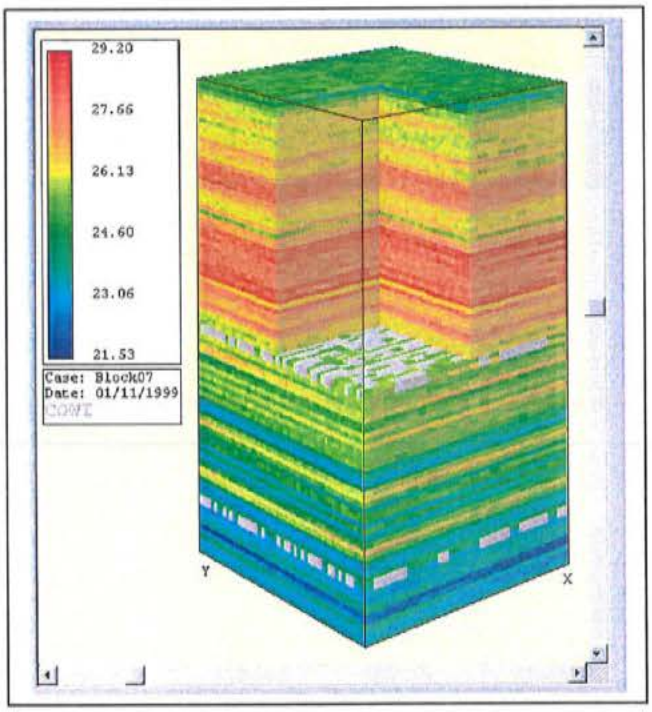

Figure 137
Porosity distribution in the middle block. A cut is made into the block to show one of the chert layers.

The up-scaled permeability tensor is purely diagonal:

$$\mathbf{k} = \begin{bmatrix} \mathbf{0.43} & \mathbf{0.00} & \mathbf{0.00} \\ \mathbf{0.00} & \mathbf{0.44} & \mathbf{0.00} \\ \mathbf{0.00} & \mathbf{0.00} & \mathbf{0.11} \end{bmatrix} \ \mathbf{mD} \qquad (3)$$

which for this block results in an effective anisotropy $k_V/k_H = 0.25$.

The up-scaled porosity is **25.8%**

Upscaling lower block (Block08)

Block size 1m x 1m x 1.54m from depth 1801.84m to 1803.38m. Two 2cm thick chert layers are present in the block at depths 1800.88m and 1801.60m.

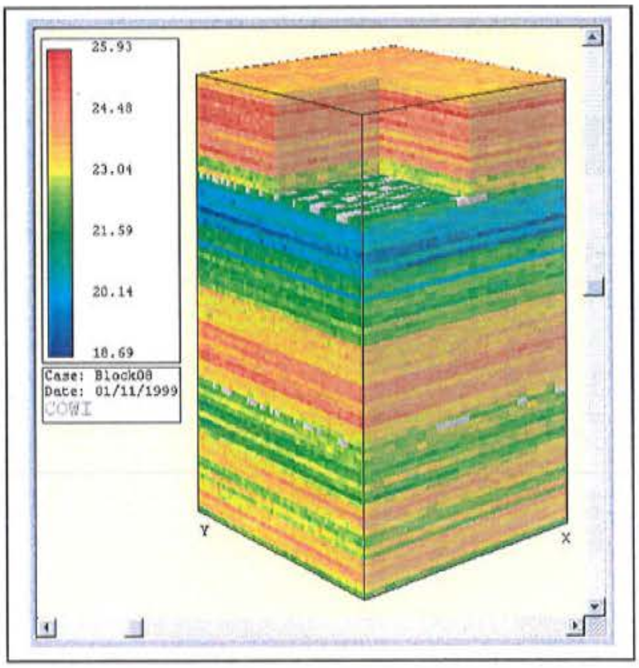

Figure 138
Porosity distribution in the lower block. A cut is made into the block to show one of the chert layers.

The up-scaled permeability tensor is purely diagonal:

$$\mathbf{k} = \begin{bmatrix} \mathbf{0.} & \mathbf{0.00} & \mathbf{0.00} \\ \mathbf{0.00} & \mathbf{0.3} & \mathbf{0.00} \\ \mathbf{0.00} & \mathbf{0.00} & \mathbf{0.14} \end{bmatrix} \mathbf{mD} \tag{4}$$

which for this block results in an effective anisotropy $k_V/k_H = 0.61$

The up-scaled porosity is **23.0%**

The three small-scale blocks was also up-scaled without the chert layers in order to investigate the effect of these layers. The anisotropy, k_V/k_H, increased by 5% for Block 6 and Block 8 and 20% for Block 7. So no significant effect of the chert layers was observed. However, the effect of the chert layers would increase in case the coverage is increased (more tight layers) or the distribution of the chert is changed so that it is distributed with only a few larger holes (more tortuous flow).

Up-scaling to grid block size

The three up-scaled blocks, Block06, Block07 and Block08 are used as building blocks in forming a 50m x 50m x 4.62m grid block. As no lateral data exist outside the 20m column a simple layered pattern consisting of 2500 of each of the building blocks are formed. Figure 139 shows the distribution of the 7500 building blocks.

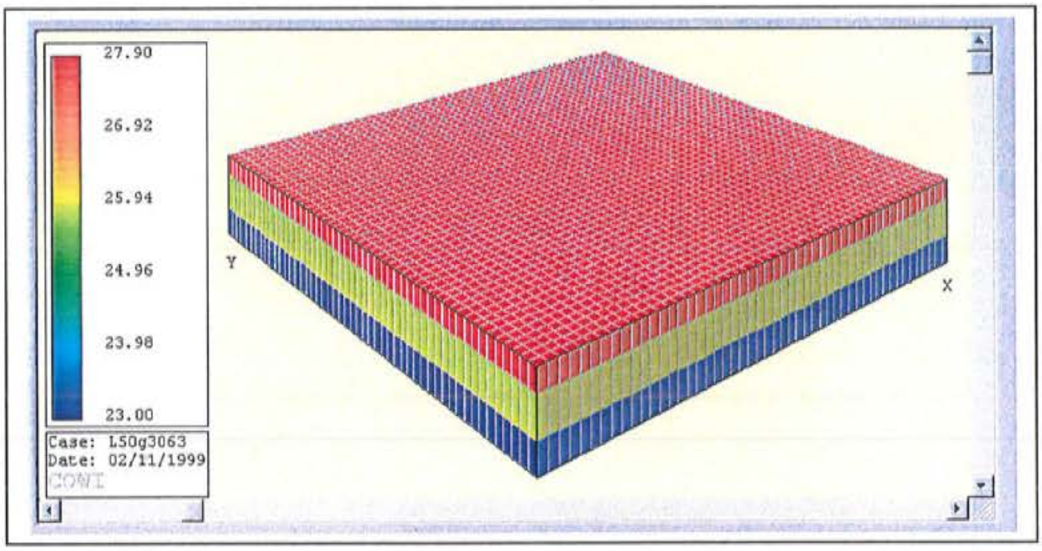

Figure 139
The matrix porosity distribution in the reservoir grid block.

In this last up-scaling step the matrix data are combined with an overall fracture pattern consisting of three fracture populations with different apertures:
Long fractures: 45 μ hydraulic aperture (138 fractures)
Short fractures: 25 μ hydraulic aperture (525 fractures)
Damage zone: 30 μ hydraulic aperture (2400 fractures)
The assignment of apertures is a step with large uncertainty. Very few data exist on measured fracture apertures and their variability. Data from shallow subsurface hydrogeology investigations in chalk have indicated a range from 50 to 500 μm with a mean around 250 μm (Younger & Elliot 1995). The effect from reservoir conditions on apertures is unknown. Figure 140 show the overall fracture pattern. The long fractures coloured red, the short fractures coloured blue and the damaged zone fractures coloured green.

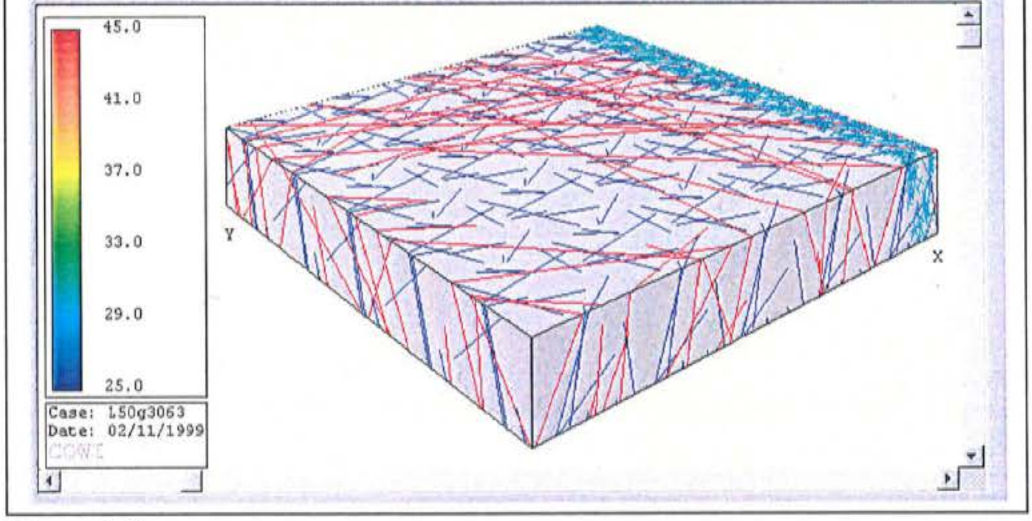

Figure 140
Overall fracture pattern. The fracture colours indicate the size of the apertures in microns.

The procedure used for this last up-scaling step to a reservoir grid block of the matrix and the fracture pattern shown in Figures 139 and 140 depends on the subsequent reservoir simulation type, single porosity or dual porosity.

For dual porosity formulation the matrix distribution and the fracture pattern are up-scaled individually as shown below.

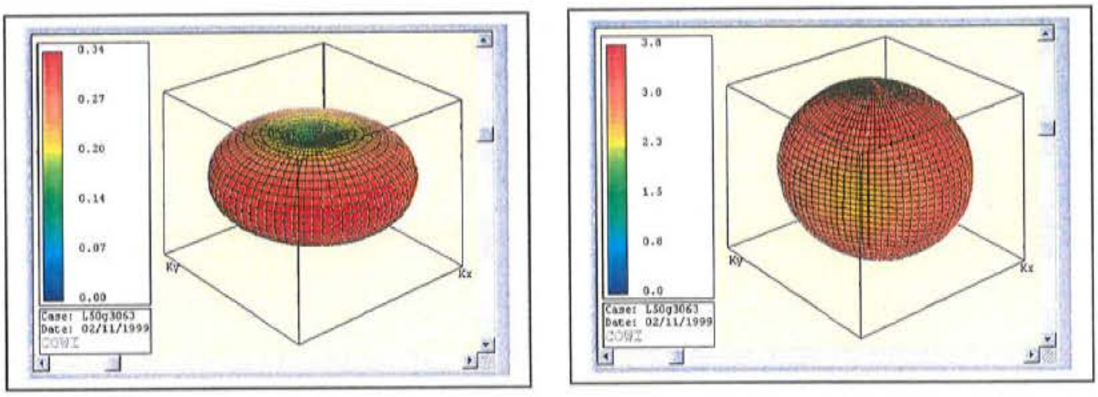

Figure 141
Up-scaled directional permeability for the matrix part (left) and the fracture pattern part (right).

In figure 141 the up-scaled permeability is presented graphically as a directional permeability plot in which the permeability in a certain direction is the length from origo (centre of box) to the imaged permeability surface.

The computed matrix directional permeability is given as the tensor

$$\mathbf{k}_{matr} = \begin{bmatrix} \mathbf{0.33} & \mathbf{0.00} & \mathbf{0.00} \\ \mathbf{0.00} & \mathbf{0.34} & \mathbf{0.00} \\ \mathbf{0.00} & \mathbf{0.00} & \mathbf{0.13} \end{bmatrix} \mathbf{mD} \tag{5}$$

which for this 3-layer block results in an effective matrix anisotropy k_V/k_H = **0.38**.
The up-scaled matrix porosity is **25.4%.**
As the off-diagonal permeability terms are zero the main flow directions are parallel to the axes of the co-ordinate system.

The computed fracture directional permeability is

$$\mathbf{k}_{frac} = \begin{bmatrix} \mathbf{2.87} & \mathbf{-0.48} & \mathbf{-0.04} \\ \mathbf{-0.48} & \mathbf{3.20} & \mathbf{-0.05} \\ \mathbf{-0.04} & \mathbf{-0.05} & \mathbf{3.78} \end{bmatrix} \mathbf{mD} \tag{6}$$

which for this full fracture model results in an effective fracture network anisotropy k_V/k_H = **1.32** and **1.18** for the k_{Hx} and k_{Hy} directions respectively.
The up-scaled fracture porosity is **0.005%**.
The off-diagonal terms are seen to be non-zero indicating cross-flow. These off-diagonal terms can be minimised by a rotation of the co-ordinate system. The angle of rotation indicates the main flow direction.
The rotated permeability tensor becomes

$$k_{frac}^{rot} = \begin{bmatrix} 3.78 & 0.00 & 0.00 \\ 0.00 & 3.55 & 0.00 \\ 0.00 & 0.00 & 2.52 \end{bmatrix} \text{ mD} \tag{7}$$

Main flow direction is: **-54°** (positive x-axis direction 0°)

For single porosity formulation the matrix distribution and the fracture pattern are combined and up-scaled as shown below

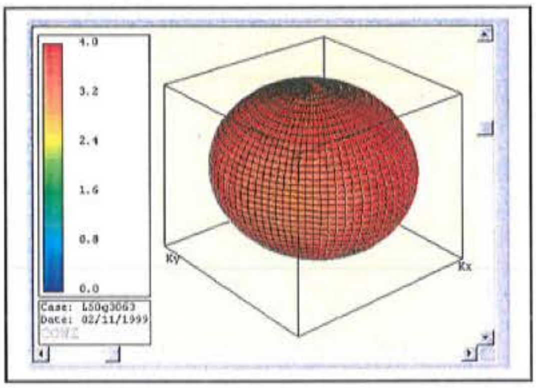

Figure 142
Up-scaled directional permeability for the combined matrix and fracture pattern (right).

The computed combined matrix and fracture directional permeability is

$$k_{m+f} = \begin{bmatrix} 3.36 & -0.43 & -0.05 \\ -0.43 & 3.64 & -0.05 \\ -0.05 & -0.05 & 3.96 \end{bmatrix} \text{ mD} \tag{8}$$

which for this full matrix and fracture model results in an effective combined anisotropy k_V/k_H = **1.18** and **1.09** for the k_{Hx} and k_{Hy} directions respectively.
The up-scaled porosity is **25.4%**

By rotating the co-ordinate system by an angle that minimises the off-diagonal terms the permeability tensor becomes

$$k_{f+m}^{rot} = \begin{bmatrix} 3.97 & 0.00 & 0.00 \\ 0.00 & 3.94 & 0.00 \\ 0.00 & 0.00 & 3.04 \end{bmatrix} \text{ mD} \tag{9}$$

with a main flow direction of **-54°** (positive x-axis direction 0°)

The main flow direction is consistent with the overall direction of the long fractures shown in red in Figure 140.

Conclusions

The study shows how a fine-scale matrix model can be constructed when only wireline log and limited core information is available from a sequence. The matrix model has been constructed to reflect both porosity variations in the chalk matrix as well as incorporation of flint layers. Likewise, the data on fractures from a sequence have been used to form input to the fracture modelling that supplies the fracture network to incorporate in the larger-scale model. The upscaling of the matrix properties for a selected part of the reservoir zonation, as well as the combined system of matrix and fractures for that part is shown.
With the present assumptions about apertures and fracture models, the permeability enhancement factors from pure matrix to matrix+fracture system is 10.2, 10.7, and 30.5 for the x,y and z directions for the present block model.
The effective properties of the grid block and the fracture network can be used for estimating any possible re-orientation of the simulation grid at larger scale.

The demonstration has been concerned with the steps required for upscaling a single reservoir simulation grid block size model. The further distribution of grid blocks and their properties in a larger scale, or even full field model, has not been developed here. The demonstration shows the application of the different procedures and methods.

References

Bech, N. 1999: Fracture interpretation and flow modelling in fractured reservoirs. Danmarks og Grønlands Geologiske Undersøgelse Rapport 1999/13, and in press as EU Special Publication **EUR 18946**. Bruxelles: EU Commission.

Jørgensen, O. & Petersen, N.W. 1999: Interpreting Natural Fracture Directions in Horizontal Wells from Wellbore Image Logs. AAPG Hedberg Symposium, October 10-13, .

Koestler, A.G. & Reksten, K. 1992: Insight into the 3D Fracture Network of an Exposed Analogue of Fractured Chalk Reservoirs. The Lägerdorf Case. 1992 Fourth North Sea Chalk Symposium,, .

Lehne, K.A. & Aadnoy, B.S. 1992: Quantitative Analysis of Stress Regimes and Fractures from Logs and Drilling Records of a North Sea Chalk Field. The Log analyst, 351.

Ma, T.A., Lincerum, V., Reinmiller, R. & Mattner, J. 1993: Natural and induced fracture classification using image analysis. SPWLA 34th Annual Logging Symposium, June 13-16, .

Younger, P.L. & Elliot, T. 1995: Chalk fracture system characteristics; implications for flow and solute transport. The Quarterly Journal of Engineering Geology **28**, 39-50.

Conclusions and recommendations for future work

Peter Frykman (GEUS)
Flemming If (COWI)
John Jansson (COWI)

CHARACTERISATION AND MULTISTEP UPSCALING OF FRACTURED CHALK RESERVOIRS

JCR PHASE V, PROJECT NO. 3

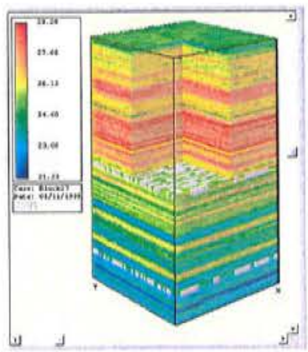

Conclusions

From the project work the following main achievements and conclusions are summarised:

- The matrix study and developed up-scaling method have demonstrated that it is possible to incorporate fine scale matrix heterogeneities and small and large scale fracture networks in the upscaling procedure.

- A range of different heterogeneities have been investigated for their heterogeneity effect on the permeability anisotropy. For some small-scale features like clay-flasers and lamination, a clear effect on the k_V/k_H is seen. Larger-scale features like cyclic bedding and flint layers are also shown to have an effect. If both small- and large scale features occur embedded in the same sequence it is called "nested anisotropy", and the k_V/k_H is a cumulative effect that has been studied with upscaling using flow simulation technique.

- Although the concept of type models has been advocated, the practical implementation of the upscaling scheme has shown that even in limited sequences, the effective properties for m^3 size blocks can vary significantly. It is therefore at the moment not possible to supply a limited catalogue of type models that can have wide application. The concept might find use in case studies, and maybe type models can be established for slightly larger volume elements than m^3 to be used as building blocks.

- The petrophysical expression of fractures has been successfully implemented in the fine-scale simulations for an upscaling of both matrix and fracture system in a given block.

- The merging of matrix models of different sizes and resolution with the fracture models is straight forward with the new developed software tool for upscaling. For this tool, valid and robust formulations of the aperture-to-permeability, and a 3D-tensor description of the effective permeabilities have been developed.

- The efforts put into a case study is related to the application of the modelling and upscaling scheme in relation to matrix and fracture data from two related wells in a chalk reservoir. The layering of the matrix gives rise to k_V/k_H ratios down to 0.25 for some of the building blocks, and the fracture system has been categorised into 3 main suites with significantly different fracture densities: background, layer-bound, and fault-related damage zone.

Recommendations for future work

Based on the findings and conclusions from the project we recommend the following work to be initiated.

Extension of the developed up-scaling method

The present version of the developed up-scaling method is designed for treating single phase flow. As a step towards the handling of two phase flow, the method could be extended to account for relative permeability effects caused by varying saturations of the flowing phase. The water saturation can be estimated as a function of the porosity profile and the position of the free water level (FWL), and hence an effective oil permeability (oil relative permeability to water) can be calculated using the relative permeability functions for the sequence. The effect of this would then be, that intervals with increased water saturation would significantly lower the effective vertical oil permeability.

The developed up-scaling method can be further extended to handle two or three phase flow. This will involve the full 3D treatment of matrix/fracture exchange, shape factors, relative permeabilities, capillary pressure functions etc. It is a major task, which however would make the developed up-scaling method more useful for generation of input to reservoir simulation models.

Extend the program to include the possibility for handling variable layer thickness.

Provide outer loop around the calculation procedure, such that upscaling is performed on a whole range of reservoir simulation grid cells. If for instance the fine grid definition is 100*100*40, the tool should produce upscaled parameters for e.g. a 10*10*8 model representing the same reservoir volume.

Geological and petrophysical characterisation

For improved modelling of the fine-scale matrix models, it is necessary to develop further a scheme for modelling the extremes in porosity and permeability variations associated with bedding features, hardgrounds and flint occurrences. The wireline log data only supplies a filtered version of the fine-scale variability, and core data is sparse and scattered. Therefore, better knowledge of the fine-scale patterns in reservoir chalk needs to be developed, closely connected with work on the cyclic aspects of chalk sequences.

The original objective of establishing the concept of "type models" for reservoir chalk and their associated patterns of heterogeneities has been investigated. The aim was to define a building block of m^3 size that was representative for a reservoir unit. From the work in this report on upscaling of the different sequences based on real field data, it has become apparent that the concept is non-operational for m^3 size models. This size is too small to be representative, and even within a limited sequence, the variation in upscaled properties is large. The concept might be operational at larger scales, i.e. for larger rock volumes, but this must be investigated for specific examples.

From the work with fracture systems, it is obvious that a further and more definitive characterisation of apertures is necessary. The quantification of apertures, and more importantly the spatial variation in aperture, is so far including a very large uncertainty. Their spatial variations might give rise to channeling of flow in only segments of the fracture network. Extreme values in this variation might cause highly productive pathways to exist in the fracture system, and possibly being independent of the general network geometry. Until now, no rules have been developed for these relations, and therefore it is an area with large potential for improved characterisation.

Also the length distribution of fractures in the fracture systems in reservoir chalk is a field of uncertainty. Only limited experience can be drawn from analogue outcrops, and a quantification of the limits for variation needs to be developed further.

****